Mon. Not. R. Astron. Soc. **270**, 523–569 (1994)

Dynamics and stellar populations in early-type galaxies

C. Marcella Carollo* and I. John Danziger
European Southern Observatory, Karl-Schwarzschildstrasse 2, D-85748 Garching bei München, Germany

Accepted 1994 April 28. Received 1994 April 20; in original form 1993 November 29

ABSTRACT

Optical multiband CCD photometry and multiposition CCD long-slit spectroscopy are presented for the five early-type galaxies NGC 439, NGC 2434, NGC 3706, NGC 6407 and NGC 7192. Light and morphological profiles, rotation velocity and velocity dispersion profiles, as well as Mg_2 and ⟨Fe⟩ line-strength radial profiles are reported. In some cases the measurements extend beyond two effective radii.

Peculiar core kinematics are detected in NGC 2434 and NGC 7192, in which the innermost nuclear regions counter-rotate with respect to the main galactic bulk. Corresponding with the kinematically decoupled core, an enhancement in the Mg_2 index is observed. A much weaker signature of enhancement with respect to the galactic bulk is found in the corresponding ⟨Fe⟩ profiles. Should this phenomenon turn out to be common, it might be at least partly responsible for the relatively shallow slope in the ⟨Fe⟩–Mg_2 plane shown by galactic nuclei compared to that traced *within* galaxies.

Under the assumption of axisymmetry, the Jeans equations of stellar equilibrium have been solved to model the dynamical state of each galaxy. In some objects there is evidence for the presence of a significantly massive and extended dark halo (in some cases, even more flattened than the luminous galaxy).

The dependence of the *local* metallicity (as traced by the Mg_2 index) on physical parameters that possibly influence the local chemical enrichment has been investigated. In particular, a *local* dependence of the metallicity on the escape velocity from the potential well has been found (supporting previous results); however, the spread in the *local* relationship hints at other physical parameters, in addition to the local potential, affecting the metallicity distribution within galaxies. The Mg_2 index is found to correlate with the *local* stellar density ρ (as described by the R surface brightness) rescaled by the *total* galactic mass M, i.e. with ρM^2. The slope of such a correlation *within* individual galaxies seems consistent with the *average* relationship derived by Bender, Burstein & Faber for galactic nuclei. A significant spread, reduced when the dark component is added to the scaling mass, is, however, present in the relationship. Part of such a scatter might arise from a residual dependence on the galactic size, possibly incompletely accounted for with the M^2 dependence.

Key words: galaxies: abundances – galaxies: elliptical and lenticular, cD – galaxies: fundamental parameters – galaxies: kinematics and dynamics – galaxies: structure.

1 INTRODUCTION

A good deal of evidence seems to suggest that massive, boxy, pressure-supported ellipticals and smaller, discy, rotation-supported elliptical and lenticular galaxies are the end-products of different star formation histories leaving their signature in the galactic orbital structure and stellar populations as revealed by kinematics, colours, line strengths and line-strength ratios. However, the exact interplay between structural, dynamical and population properties in early-type galaxies still remains undefined. For example, it is still unclear whether the observed metallicity content and distribution within individual galaxies, e.g. the increasing trend with mass shown by line-strength gradients (Carollo, Danziger & Buson 1993, hereafter CDB), are properties

*Present address: Sterrewacht Leiden, Postbus 9513, 2300 RA Leiden, The Netherlands.

related to the details of the orbital structure, such as the presence of a stellar disc, or rather properties dependent only on fundamental parameters or global quantities, such as the total mass involved in the galactic formation process or the total angular momentum of the system. A major difficulty in identifying the crucial parameters is the fact that the observable quantities do not often allow one to discriminate between various phenomena. For example, although the ratio V/σ provides information on the total angular momentum of the system, such a ratio is, on the other hand, also affected by the amount of dissipation that occurred in the process of galaxy formation. A high V/σ does not necessarily testify to the presence of a stellar disc, but in some cases can indeed be due to such a disc; pressure-supported galaxies with low V/σ do possibly arise from almost dissipationless processes (see Worthey, Faber & Gonzalez 1992, hereafter WFG; Bender, Burstein & Faber 1992, 1993, hereafter, respectively, BBF1 and BBF2; CDB).

Another unresolved question is why, on the one hand, the global galactic properties indicate a high degree of homogeneity from galaxy to galaxy (as shown, e.g., by the correlation of the nuclear Mg_2 line strength with the velocity dispersion σ, or equivalently with the density-dependent parameter $M^2\rho$; BBF1 and BBF2), and why, on the other hand, for example, the Mg_2–$\langle Fe\rangle$ and the σ–Mg_2 relationships within galaxies do not follow the corresponding patterns generated by galactic nuclei (WFG; Davies, Sadler & Peletier 1993, hereafter DSP; CDB). This latter result strongly questions, for example, the local onset (regulated by the local escape velocity) of a supernovae-driven galactic wind as the unique origin of the observed global correlations (Franx & Illingworth 1990, hereafter FI; DSP). A valuable test to investigate whether, and to what extent, the global correlations found for cores are also valid throughout whole galaxies is to look for features in the line strength, colour or kinematic profiles at large galactocentric distances, where, for example, anisotropy in the velocity dispersion, dark matter and signs of interaction with the environment should be more easily detectable. Any anomalous feature (such as non-homogeneities or age variations in the galactic structure and population, respectively) might strongly constrain plausible scenarios of galaxy formation.

The investigation of these issues was one of the original incentives for starting a detailed study of a few selected galaxies (Carollo & Danziger 1994, hereafter Paper I). Here, we present a follow-up to that previous study, i.e. we present new multicolour optical photometric and multislit spectroscopic observations for five early-type galaxies, namely NGC 439, NGC 2434, NGC 3706, NGC 6407 and NGC 7192. In Section 2, details of the observations, an outline of the basic steps of data reduction and some general information on the sample are reported. In Section 3 the derived photometric, kinematic and line-strength radial profiles for all the galaxies of the sample are shown. All the galaxies are modelled in Section 4, with the same kind of axisymmetric dynamical models presented in Paper I. *Local* relationships between, for example, colours and line-strengths, and *local* dependences of colours and line-strengths on the depth of the galactic potential well (described by the local escape velocity) and on the stellar density (as described by the surface brightness in the R band) are presented and discussed in Section 5. Section 6 concludes this paper.

2 OBSERVATIONS

Broad-band optical imaging and multiposition long-slit spectra of NGC 439, NGC 6407 and NGC 7192 were taken in 1992 July 22–27, at the ESO New Technology Telescope, located at La Silla. The other two galaxies of the sample, NGC 2434 and NGC 3706, were observed at the 2.2-m ESO/MPI telescope (La Silla) during 1993 January 21–25. Long-slit spectra were also taken for these two galaxies at three position angles, including the two major photometric axes. Multicolour optical photometry was taken only for NGC 2434, because it was already available for NGC 3706 from a previous photometric survey conducted at the 1.54-m Danish–ESO telescope (Carollo 1993, hereafter C93). Information for each run, the instruments, the instrumental configurations, the detector characteristics and the corresponding spatial and wavelength resolutions are given in Tables 1(a) and (b).

The logs of the observations are reported in Tables 2(a) and (b).

2.1 Photometry

In both runs, broad-band imaging was performed with B, V, R and I ESO–Cousin standard filters. The run at the 2.2-m telescope was photometric, with an average seeing FWHM of 1.1 arcsec in the I band, 1.5 arcsec in the R band, 1.7 arcsec in the V band and 1.3 arcsec in the B band. During those nights, exposures of Landolt CCD standard fields were taken at various times during the night. The whole run at the NTT was non-photometric, and on some occasions even very cloudy. The average seeing FWHM there was 1.3 arcsec in the I filter, 1.4 arcsec in the R and V filters and 1.6 arcsec in the B filter. The observations of NGC 3706 were also performed under imperfect photometric conditions (although weather conditions were rather good); standard stars (Landolt CCD fields) were observed. The average seeing was 1.1 arcsec in the R band and 1.3 arcsec in the B band.

For each set of photometric observations, the basic steps of data reduction were performed as described in Paper I, by using the ESO MIDAS package (bias and dark current were subtracted from the science frames, and high-count twilight sky exposures were used to flat-field the frames). For the 2.2-m data, the absolute photometric calibration was obtained by using all available standard stars. The derived colour equations, using R as the main filter, are (see Paper I)

$$B_{\rm Bessel} = 21.819 + B_{\rm tel} + 0.203(B-R)_{\rm tel}, \tag{1}$$

$$R_{\rm Bessel} = 23.653 + R_{\rm tel}, \tag{2}$$

and, for the V filter,

$$V_{\rm Bessel} = 23.45 + V_{\rm tel} + 0.135(V-R)_{\rm tel}. \tag{3}$$

Published aperture photometry from the Longo & de Vaucouleurs (1983) and de Vaucouleurs & Longo (1988) compilations was used to calibrate the NTT data and NGC 3706. For the R filter of NGC 7192, aperture photometry was not available, and we calibrated the frame assuming the same conversion factor derived from the R filters of the other two galaxies.

For the galaxy observed at the 2.2-m telescope (NGC 2434), the zero-point error in the calibration (derived by

Table 1. The characteristics of the detectors and the instrumental setup for the spectroscopic (a) and photometric (b) runs.

(a)

Run	Telescope	Instrument	CCD(1)	ron	λ range	Slit(2)	Pixel Size(3)	Resolution
22–27 July 1992	NTT	EMMI	ESO # 18	5	4700–5700	1.8	2×0.88	4.5
21–25 Jan 1993	2.2m	EFOSC2	ESO # 19	5	4600–6000	1.5	2×0.66	5.

Units are: read-out noise (ron) in e^-/pixel; wavelength range in Å; slit width in arcsec; pixel size in Å× arcsec; resolution (i.e. FWHM of Thorium/HeAr emission lines and sky lines) in Å.
(1)Thomson Coated, 1024 × 1024 pixels of 19 × 19 μm^2.
(2)In table, the slit width. Both chips are about 7 arcmin long.
(3)The CCD was always rebinned 2 × 2; the listed pixel size already includes such a rebinning.

(b)

Run	Telescope	Instrument	CCD	ron	ESO filters	Pixel Size
22–27 July 1992	NTT	EMMI	ESO # 18	5	B,V,R,I standard	0.44
20–25 Jan 1993	2.2m	EFOSC2	ESO # 19	5	B,V,R standard	0.332

Units are: read-out noise in e^-/pixel; pixel size in arcsec.

Table 2. Observations logs for the spectroscopic (a) and photometric (b) runs.

(a)

name	P.A. (deg)	Telescope*	exposure time (sec)
NGC 439	158	NTT	3×3600$_{REMD}$
NGC 439	48	NTT	2×3600$_{REMD}$
NGC 2434	318	2.2m	5×3600
NGC 2434	48	2.2m	2×3600
NGC 2434	90	2.2m	3600
NGC 3706	73	2.2m	8×3600
NGC 3706	163	2.2m	2×3600
NGC 6407	63	NTT	5×3600$_{DIMD}$+2×3600$_{REMD}$
NGC 6407	153	NTT	4×3600$_{REMD}$
NGC 6407	108	NTT	3600$_{REMD}$
NGC 7192	20	NTT	6×3600$_{DIMD}$
NGC 7192	110	NTT	3600$_{REMD}$
NGC 7192	65	NTT	3600$_{REMD}$

*During NTT observations, the Dichroic Mode of EMMI (DIMD) was used sometimes to collect simultaneously spectra in a bluer wavelength range (4000–4600 Å). The analysis of these spectra will be reported elsewhere. The observations taken without dichroic are labelled as REMD (normal EMMI red-arm mode).

(b)

name	run	exposure time (sec)	filter	Δ*mag**
NGC 439	July 1992	600	B	$\lesssim$0.1
NGC 439	July 1992	180	R	$\lesssim$0.1
NGC 439	July 1992	180	I	$\lesssim$0.1
NGC 2434	Jan 1993	360	B	$\lesssim$0.03
NGC 2434	Jan 1993	120+150	V	$\lesssim$0.03
NGC 2434	Jan 1993	60+120	R	$\lesssim$0.03
NGC 6407	July 1992	600+600+600	B	$\lesssim$0.1
NGC 6407	July 1992	180+180+180	V	$\lesssim$0.1
NGC 6407	July 1992	180+120+60	R	$\lesssim$0.1
NGC 7192	July 1992	600	B	$\lesssim$0.1
NGC 7192	July 1992	180	V	$\lesssim$0.1
NGC 7192	July 1992	180+60	R	$\lesssim$0.3
-	-	-	-	-
NGC 3706**	Jan 1993	420+600+600	B	$\lesssim$0.05
NGC 3706**	Jan 1993	60+60+60+50+50+50+90	R	$\lesssim$0.05

*Zero-point error in the photometric calibration.
**Observations performed during the nights of 1993 January 16–20 at the 1.5-m Danish–ESO telescope. Standard ESO–Cousin filters were used. The chip was a CCD Tektronix 1024 × 1024, 24-μm (0.377-arcsec) size pixels. Details on this run of observations will be published in a separate paper (see text).

comparing the results obtained by using different templates taken in various occasions during the nights) was estimated to be smaller than 0.03 mag. For NGC 3706, the calibration derived from aperture photometry and that derived from Landolt fields stars were consistent to within ≈ 0.05 mag. The zero-point error of the NTT observations was that of the aperture photometry used (≤ 0.1 mag, from the scatter in the data published by different authors). Only for the R band of NGC 7192 might the calibration error be as large as 0.3 mag. The latter value gives the average scatter in the calibration of the other two galaxies of that run for which the R aperture photometry was available. It gives an estimate of the degree to which the weather conditions were non-photometric when the R exposures of NGC 7192 were taken.

The derived light profiles were K-corrected (as in Whitford 1971), and corrected also for Galactic reddening by using the extinction values published by Burstein & Heiles (1984; NGC 439, $A_B = 0$; NGC 2434, $A_B = 0.71$; NGC 3706, $A_B = 0.36$; NGC 6407, $A_B = 0$).

2.2 Spectroscopy

All spectroscopic exposures were limited to a maximum of one hour, in order to avoid excessive cosmic-ray events on the galaxy spectra. The slit was always centred on the galaxy nucleus. At the NTT, thorium (and, at the 2.2-m telescope, HeAr) calibration spectra were taken after each exposure, to determine the wavelength scale. Spectrophotometric standard stars were taken in both runs, as well as G and K giants, to be used as kinematical templates and to correct the galactic line strengths for velocity dispersion broadening.

Also, for each set of spectroscopic data we used the ESO MIDAS package for the basic data reduction. Bias and dark current were initially subtracted from all science frames. Small-scale sensitivity variations (determined from high-count quartz lamp exposures) were subsequently removed; twilight sky exposures were used to produce the correction for the variable vignetting along the slit. After removing cosmic rays and faulty pixels, the star and galaxy spectra were wavelength-calibrated by fitting, row by row, a third-order polynomial to the positions of the emission lines of the corresponding thorium or HeAr arc frames. The accuracy of the wavelength calibration was checked on the sky emission lines present in the galaxy spectra; an average accuracy of $\simeq 15$ km s^{-1} was reached for both the NTT and the 2.2-m data. A spectrum of the sky present in the science frame was generated by averaging, frame by frame, the outermost 25 rows on each side of the CCD; this sky was then subtracted from the corresponding star or galaxy spectrum. Just as for the data presented in Paper I, some tests were made to check the influence of the sky subtraction on the reported measurements (e.g. under- and over-sky subtraction, by 10 per cent, were applied to the galaxy spectra; these tests have shown that the line-strength and kinematic profiles reported in the following sections are reliable to the outermost measured radii within their error bars). The spectra were corrected for Galactic extinction and finally corrected for instrumental response by using the conversion derived from the spectrophotometric standards. The photometric conditions of the 2.2-m run allow one to consider the latter correction as an absolute flux calibration for the spectra taken during that run.

2.3 The sample

In Table 3, some physical parameters for the galaxies of the sample are given. In the following, we also give a brief summary of the morphological classification, the environmental conditions and any known peculiarity or non-stellar emission for each of the five galaxies. Excluding NGC 3706, which is a well-studied object, the other four galaxies were chosen because they had not yet been studied in detail.

NGC 439. It is classified as a lenticular by de Vaucouleurs et al. (1991, hereafter RC3) and as E-S0 by Lauberts & Valentijn (1989, hereafter ESOLV). It is the brightest member of a group containing six other members, one of which is a lenticular, the other five being spirals (Maia, Da Costa & Latham 1989). The group mass-to-light ratio is about 40 (Gourgoulhon, Chamaraux & Fouqué 1992). The galaxy is not a known X-ray or *IRAS* source, and has no H I emission and no emission lines. A compact faint nuclear

Table 3. Physical parameters for the galaxies of the sample.

Name	Type	Vel_{hel}	m_B	P.A.	ϵ	R_e	$(B-V)_o$	Mg_{2centr}	σ_o
NGC 439	E	5679	12.38	158	.33	45	-	-	-
NGC 2434	E	1388	12.50	138	.08	24	.91	.268	205
NGC 3706	E	3045	11.87	74	.32	27	.92	.310	281
NGC 6407	E	4625	12.88	63	.17	33	-	-	-
NGC 7192	E/cD	2763	12.21	20	.02	28	.95	.250	185

Column: 1 – name of the galaxy; 2 – morphological type; 3 – heliocentric velocity; 4 – apparent blue magnitude; 5 – position angle of the major axis (NE); 6 – ellipticity; 7 – effective radius, i.e. half-light radius; 8 – corrected $(B-V)$ colour within 67 arcsec; 9 – central value of Mg_2 index; 10 – central velocity dispersion.
Units: position angle of major axis in degrees; heliocentric velocity and velocity dispersion in km s^{-1}; effective radius in arcsec; Mg_2 and $(B-V)$ in mag.
All parameters are from ESOLV or RC3, with the exclusion of Mg_2 and σ_0 (from Davies et al. 1987) and $(B-V)_0$ from Burstein et al. 1987).

radio source has been observed (Bregman, Hogg & Roberts 1992).

NGC 2434. The galaxy is classified as elliptical by both RC3 and ESOLV. Together with two other galaxies, it is a member of Huchra & Geller (1982) group number 1. A possible dwarf elliptical (or blue compact dwarf) companion has been identified by Vader & Chaboyer (1992).

NGC 3706. The galaxy is classified as lenticular in RC3 and elliptical in ESOLV. It is a shell galaxy (Malin & Carter 1983), has a compact elliptical companion (Vader & Chaboyer 1992), and has been detected in the radio continuum and in the FIR (Wilkinson et al. 1987; Sadler, Jenkins & Kotanyi 1989; Roberts et al. 1991).

NGC 6407. Not much is known about this galaxy. It is classified as lenticular by RC3 and as elliptical by ESOLV.

NGC 7192. The galaxy is classified as elliptical by both RC3 and ESOLV. It belongs to a group of seven galaxies, including four spirals (Maia et al. 1989). It contains diffuse dust, as it has been detected at 100 μm (Roberts et al. 1991); Hα and N II emission have been detected (Phillips et al. 1986).

3 RESULTS

3.1 Photometric profiles

The GALPHOT package (written by M. Franx; in IRAF) was used to derive the photometric profiles through ellipse-fitting; deviations from perfect ellipses were measured by computing the C_i and S_i coefficients of the Fourier expansion of the intensity along the ellipses ($i=3$, 4, 6; see Paper I). Following the same definitions given in Paper I, the final errors reported for the photometric profiles are the sum of the formal errors derived from ellipse-fitting, plus the errors in sky subtraction; errors in the colour profiles are the sum of the errors in the two bands. Listed in Appendix A, for the five galaxies and for each filter, are the individual measurements, as functions of galactocentric distance, of surface brightness, ellipticity, major axis position angle and S_i and C_i coefficients ($i=3$, 4, 6). The $(B-R)$ colour profiles were derived; the corresponding logarithmic gradients, computed excluding the innermost seeing-affected 3 arcsec, are listed in Table 4. Also listed are the central $(B-R)$ values, computed by averaging the innermost 3 arcsec. Errors on these values are the formal rms deviations around the given averages. For a comparison of the colour gradients with those shown by a larger sample of galaxies, see, for example, FI and Peletier et al. (1990).

Table 4. The $(B-R)$ gradients and central $(B-R)$ values for the five galaxies.

name	$(B-R)_{centr}$	$err_{(B-R)_{centr}}$	$\frac{d(B-R)}{dLogr}$	$err_{\frac{d(B-R)}{dLogr}}$
NGC 439	1.52	.04	-.07	.01
NGC 2434	1.59	.10	-.12	.02
NGC 3706	1.53	.16	-.06	.01
NGC 6407	1.60	.07	-.10	.01
NGC 7192	1.41	.06	-.12	.01

3.2 Stellar kinematic profiles

In all the galaxy spectra, at least the Mg_b, the Fe_{5270} and the Fe_{5335} bands were present. A Fourier quotient package (Sargent et al. 1977) was run on all the galaxy spectra to derive the kinematical profiles, after spatial software rebinning of the CCD in order to maintain the signal-to-noise ratio (S/N) above the fixed threshold of 30. As the 2.2-m spectra had a relatively high S/N until ≈ 2 half-light galactic radii, they were also analysed with a version of the Fourier-fitting program (Franx & Illingworth 1988) developed by van der Marel & Franx (1993), and we were able to measure the two lowest moments of the line-of-sight velocity distribution (rotation velocity and velocity dispersion) and also the next two higher moments. The analysis of such higher moments is reported in a separate paper (Carollo et al. 1994, hereafter CMZD). The Fourier quotient and the Fourier-fitting programs gave comparable rotation velocity and velocity dispersion profiles for both NGC 2434 and NGC 3706; for consistency with CMZD, we report here the profiles derived with the Fourier fitting program for these two galaxies. For both the NTT and the 2.2-m data and for each galaxy, all the templates available were in turn used to derive the rotation velocity and velocity dispersion profiles. The latter showed systematic shifts of maximum ≈ 30 km s^{-1} with different templates. The templates used to derive the final kinematic profiles reported here are HR 6049 for the three galaxies observed at the NTT, and a synthetic best-fitting template, derived by superimposing with different weights all the observed K-giants, for the two galaxies observed at the 2.2-m telescope (see CMZD for details).

For the three galaxies in common with Davies et al. (1987, hereafter D87; NGC 2434, NGC 3706 and NGC 7192), our central velocity dispersions are systematically larger than those published by these authors. For NGC 2434 and NGC 3706, the discrepancy is explained by (possibly seeing) aperture and spectral resolution effects. The velocity dispersion profiles that we observe in these two galaxies are in fact very steep within ≈ 10 arcsec. Mimicking in our CCD frames an instrumental setting analogous to that used for the Lick measurements, i.e. averaging together a few central CCD's rows to simulate the Lick aperture, we obtain central σ-values in good agreement with those measured by Davies et al. (within 10 km s^{-1}). In NGC 7192, a steep velocity dispersion gradient is not observed, and the central value obtained by mimicking the Lick aperture is still ≈ 40 km s^{-1} higher than the value of Davies et al. In this case, the differences between the metallicities and abundance ratios of the template stars used by Davies et al. to derive the kinematical parameters and those used by us might play a significant role (as mentioned, we used a single template for the galaxies observed at the NTT, since we did not have enough templates to attempt any proper star–galaxy matching). The slightly higher resolution of the NTT data, as well as the already mentioned differences in the stellar templates used to derive the kinematical parameters, might also produce a systematic offset between the 2.2-m and NTT velocity dispersion profiles we present. This shift (if present) is difficult to quantify, since none of the galaxies and templates were observed at both the telescopes. However, the values obtained by mimicking the Lick instrumental setting suggest an upper limit of about 30 km s^{-1} for such an offset.

The single measurements of rotation velocity and velocity dispersion as functions of galactocentric distance are listed, for all five galaxies, in Appendix B.

3.3 Line-strength profiles

The galaxy spectra were de-redshifted, and the system of line strengths of Burstein et al. (1984) was used to compute the radial Mg_2, Mg_1, Mg_b, Fe_{5270} and Fe_{5335} line-strength profiles (as well as the Hβ profiles for the galaxies observed at the 2.2-m telescope). Errors due to photon statistics and sky subtraction were computed according to CDB.

All line strengths were standardized to zero velocity dispersion. The correction for velocity dispersion was negligible for the Mg_2 band, while it ranged from a few per cent up to some tens of per cent for the remaining bands (at $\sigma \simeq 300$ km s^{-1}, these corrections were about 19 per cent for Mg_b, 21 per cent for Fe_{5270} and 36 per cent for Fe_{5335} for the NTT data, and 13 per cent for Mg_b, 16 per cent for Hβ, 19 per cent for Fe_{5270} and 30 per cent for Fe_{5335}, for the 2.2-m data). The measured velocity dispersion profiles, appropriately smoothed, were used to correct the line strengths (following the same procedure outlined in Paper I).

As in Paper I, all the line strengths were also standardized to a spectral resolution of 9 Å, in order to minimize the discrepancy with the results of the Lick group (D87). A further comparison with the Mg_2 values reported by D87, performed as described in Paper I, showed an average shift of $-0.010(\pm 0.005)$ mag for the 2.2-m measurements relative to the Lick system. Of the galaxies observed at the NTT, only NGC 7192 is present in the list of D87; we find $\delta Mg_2(\equiv Mg_{2NTT} - Mg_{2D87}) = 0.022$. These offsets have not been added to the Mg_2 measurements reported in the tables, (i) because of the approximate nature of the derived corrections, due to the fact that only one or two comparison points were available; (ii) because the analogous corrections are not available for the other line strengths, and (iii) because individual measurements have not been published by the Lick group. For such line strengths, however, the residual systematic differences with the Lick values are expected to be rather small (see DSP and Paper I).

In Appendix C we report, for each position angle of all five galaxies, the Mg_2, Fe_{5270} and Fe_{5335} values as functions of galactocentric distance (the measurements for Mg_b and Hβ are available on request). Central Mg_2, Fe_{5270} and Fe_{5335} values and the radial logarithmic gradients of Mg_2 were computed, and are listed for all galaxies, for each position angle, in Table 5.

The central values were obtained by averaging the radial measurements inside the innermost 3 arcsec. Errors in these values are the root-mean-squares of the averaged points. To minimize seeing effects, radial logarithmic line-strength gradients excluding the points in the innermost 3 arcsec were obtained. Errors in the gradients are the formal ones obtained from the linear fit.

In the following, the results for each individual galaxy are summarized separately.

NGC 439. The photometric profiles for NGC 439 are shown in Figs 1(a)–(d) for the *B*, *V*, *R* and *I* filters, respectively. From top to bottom, each left panel shows the profiles of the surface brightness, the ellipticity and the position angle of the major axis. In the right panel, the C_i (left) and the S_i (right) coefficients are shown, with $i=3$, 4 and 6 from top to bottom. The ellipticity profile rises very steeply and continuously from the innermost regions out to the outermost measured points, reaching the value of ≈ 0.4 at ≈ 100 arcsec. No isophotal twisting is observed. Apart from a positive C_4 outside the innermost 10 arcsec, other significant deviations of the isophotes from pure ellipses are not detected. The $(B-R)$ colour profile is plotted in Fig. 2. Both the central colour and the colour gradient are typical for an elliptical of its luminosity class.

Table 5. Central Mg_2, Fe_{5270} and Fe_{5335} values and the radial logarithmic gradients of Mg_2 for all galaxies.

Name	P.A.	Mg_2	Fe_{5270}	Fe_{5335}	$-\frac{dMg_2}{d\log r}$
NGC 439	158	.300(.008)	2.67(.26)	2.70(.26)	.062(.004)
NGC 439	48	.304(.011)	2.94(.14)	2.64(.16)	.060(.002)
NGC 2434	318	.252(.018)	2.78(.12)	2.56(.13)	.055(.009)
NGC 2434	48	.256(.015)	2.68(.28)	2.45(.21)	.065(.010)
NGC 2434	90	.250(.014)	2.87(.08)	2.66(.21)	-
NGC 3706	73	.304(.010)	3.19(.13)	2.81(.19)	.074(.005)
NGC 3706	163	.307(.017)	3.18(.32)	2.77(.21)	.080(.009)
NGC 6407	153	.305(.007)	2.94(.20)	2.48(.26)	.036(.009)
NGC 6407	63	.312(.012)	2.81(.24)	2.10(.24)	.036(.010)
NGC 6407	108	.311(.008)	2.61(.19)	2.03(.26)	.041(.011)
NGC 7192	20	.278(.009)	2.81(.14)	2.62(.11)	.070(.009)
NGC 7192	110	.269(.009)	3.12(.16)	2.62(.14)	.060(.020)
NGC 7192	65	.270(.013)	2.91(.26)	2.46(.28)	.060(.009)

Units: position angle in degrees; Mg_2 in mag; two iron lines in Å; Mg_2 slope in mag dex.
1σ errors are given in parenthesis. They are defined as the rms of averaged points for central values. Formal errors of the fits are given for the gradients.

The stellar kinematic profiles of NGC 439 are shown in Figs 3(a) and (b), for the major and minor axes, respectively (velocity dispersion in the top panel and rotation velocity in the bottom panel). Along the major axis, the rotation curve rises very smoothly and reaches an amplitude of ≈ 50 km s^{-1} at about one half-light radius, while the velocity dispersion profile declines smoothly from ≈ 300 to ≈ 200 km s^{-1} in the same radial range. No rotation is observed along the minor axis.

The line-strength profiles of NGC 439 are shown in Figs 4(a) and (b), for the major and minor axes, respectively. No particular feature is observed along either of the two axes.

NGC 2434. The photometric profiles for NGC 2434 are shown in Figs 5(a)–(c), for the *B*, *V* and *R* filters, respectively (panels are as in Fig. 1). The galaxy is very round; the $(B-R)$ colour profile is normal (Fig. 6).

The stellar kinematic profiles of NGC 2434 are shown in Figs 7(a)–(c), for the major, minor and PA=90° axes, respectively (panels as in Fig. 3). No significant rotation is observed at large radii along the major axis of NGC 2434, while a very modest rotation might have been detected along the minor axis. The velocity dispersion profile is rather steep within the innermost 5 arcsec. Peculiar core kinematics are detected along all three axes, i.e. the core is counter-rotating rapidly with respect to the main galactic body.

The line-strength profiles of NGC 2434 are shown in Figs 8(a)–(c), for the major axis, minor axis and PA=90°, respectively). The Mg_2 index shows a strong enhancement in the innermost region, where the kinematically decoupled core is observed. The major axis Mg_2 and ⟨Fe⟩ indices and rotation velocity are plotted together in Fig. 9, on a linear radial scale; a sharp change in slope in the Mg_2 profile is observed at the radius of the core. Also, the ⟨Fe⟩ index shows an enhancement in the same radial range, but much less pronounced than that shown by the Mg_2 index.

NGC 3706. The *B* and *R* photometric profiles used in the following for NGC 3706 have been taken from C93; for easy reference, they are shown again in Figs 10(a) and (b), respectively (panels as in Fig. 1). The $(B-R)$ colour profile is plotted again in Fig. 11. As reported in C93, the ellipticity within ≈ 40 arcsec shows rapid variations in the range 0.25–0.4; a small (15° amplitude) but systematic isophotal twisting is observed; the C_4 coefficient shows scatter around 5 arcsec, and increases outside this radius (reaching the value of 0.04 at 40 arcsec).

The stellar kinematic profiles of NGC 3706 are shown in Figs 12(a) and (b), for the major and minor axes, respectively (panels as in Fig. 3). NGC 3706 is a fast rotator along its major axis (≈ 150 km s^{-1} at ≈ 2 effective radii); the rotation velocity profile rises very steeply, displaying the same kind of bump already observed in the innermost region of NGC

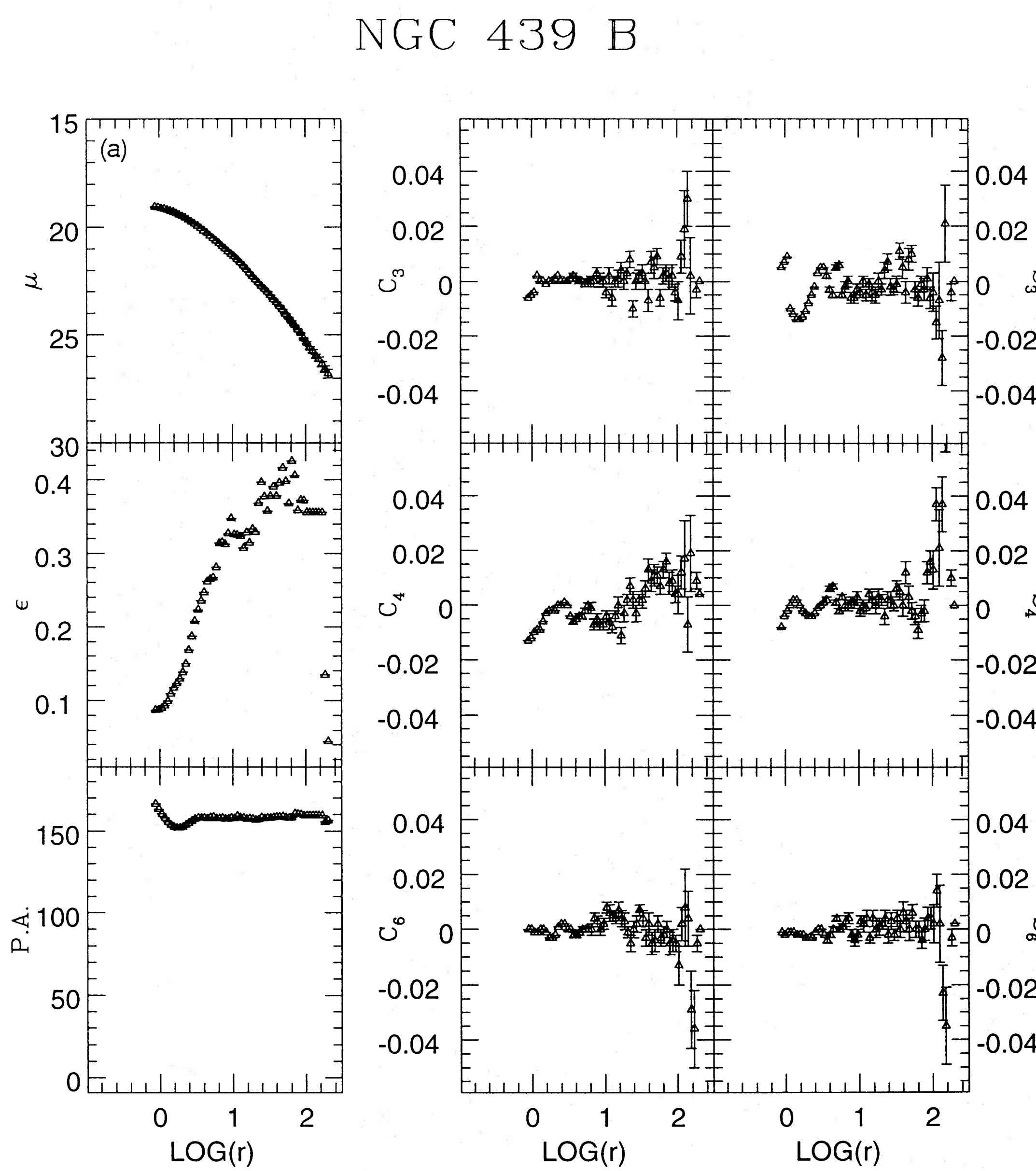

Figure 1. (a) *B* photometry for NGC 439. Left panel: surface brightness (upper), ellipticity (central), major axis position angle (lower). Right panel: C_i (left) and S_i (right) coefficients ($i = 3$, 4, 6 from top to bottom). Abscissa is $\log_{10}$(radius), in arcsec. (b) As (a), for the *R* band of NGC 439. (c) As (a), for the *I* band of NGC 439.

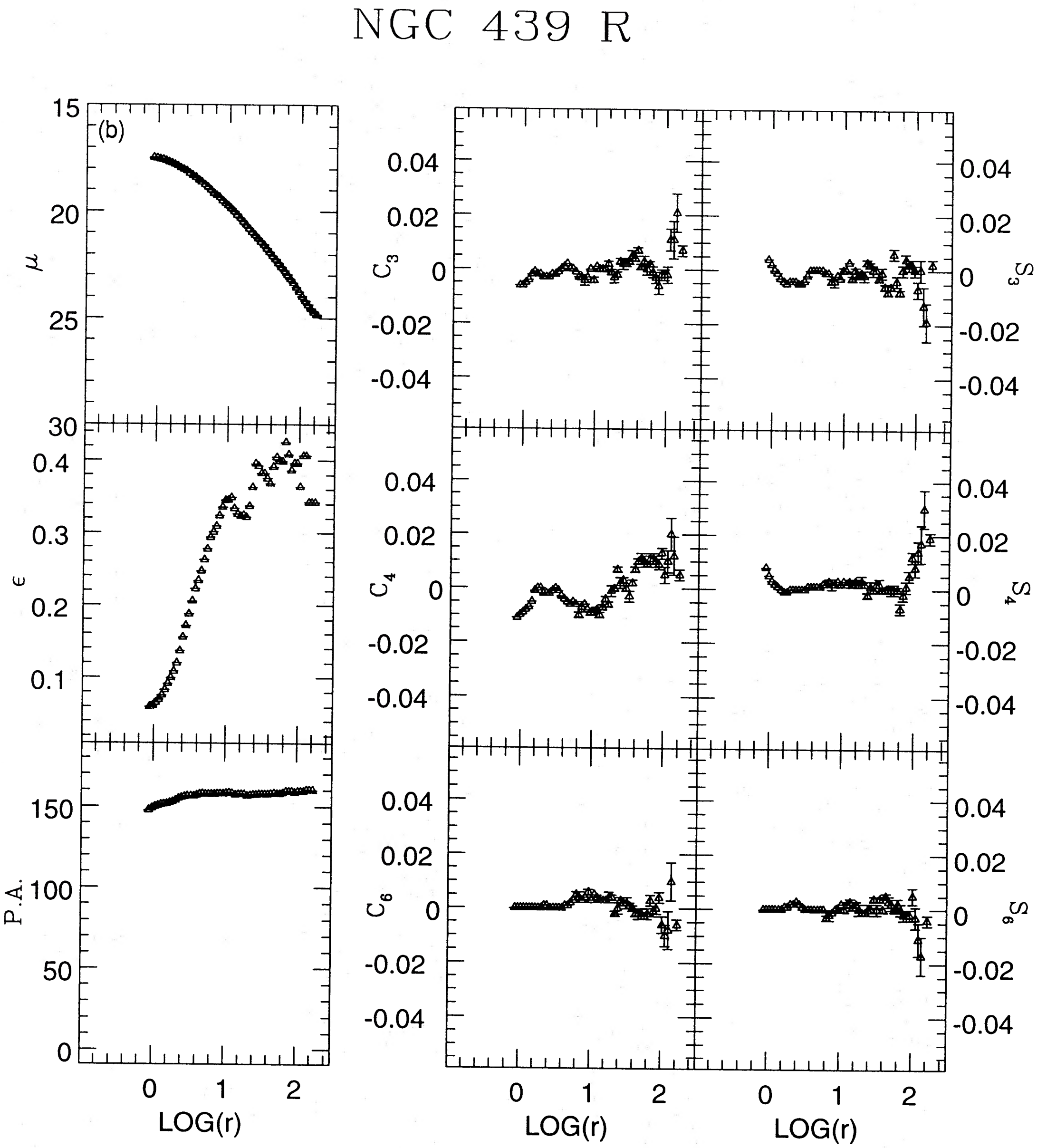

Figure 1 – *continued*

5018 (Paper I). The minor axis velocity curve is consistent with no rotation.

The velocity dispersion profiles along the two position angles appear rather peaked in the centre; no evident structure is observed at large radii.

The line-strength profiles of NGC 3706 are shown in Figs 13(a) and (b), for the major and minor axes, respectively. No evident feature is observed.

NGC 6407. The photometric profiles for NGC 6407 are shown in Figs 14(a)–(c), for the *B*, *V* and *R* filters, respectively (panels as in Fig. 1). A very bright star is close to the galaxy; even though subtraction was performed iteratively, it is likely that it might have affected the isophotal geometrical parameters. We therefore describe the observed profiles with a warning that there is the possibility that most of the features could actually arise from the imperfect subtraction of the bright star. In all three bands, the ellipticity shows a steep increase from an almost round shape to the value of ≈ 0.3 at ≈ 100 arcsec. A lot of scatter is present in the S_i and C_i coefficients, hinting at significant deviations of the isophotes from pure ellipses. In particular, C_3 and C_4 show a pronounced valley centred around ≈ 15 arcsec, where a strong bump upward is observed in S_3 and S_4, and where the maximum of isophotal twisting is reached. The $(B-R)$ colour profile, plotted in Fig. 15, shows a peculiar knee at the same radius, outside of which it decreases very rapidly.

The stellar kinematic profiles of NGC 6407 are shown in Figs 16(a)–(c) for the major, minor and PA=108° axes, respectively (panels as in Fig. 3). A good deal of scatter is also present here; the rotation velocity curves along the three

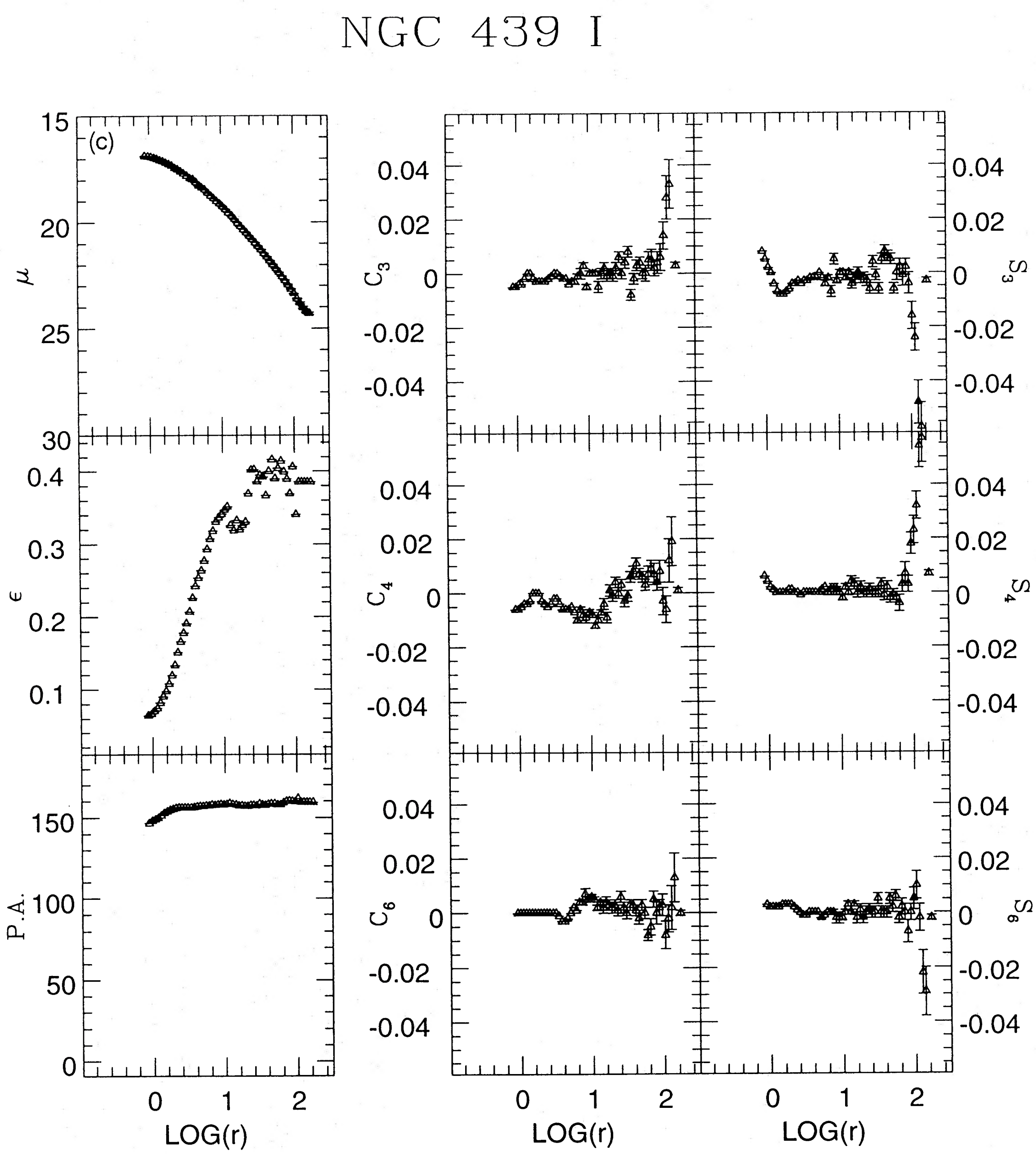

Figure 1 – *continued*

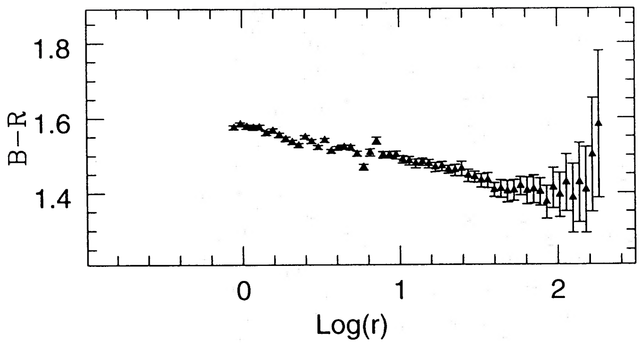

Figure 2. $(B-R)$ versus $\log_{10}$(radius) for NGC 439.

axes are, in any case, all consistent with no rotation. The data hint at core-decoupling, but the evidence is very marginal.

The line-strength profiles for NGC 6407 are shown in Figs 17(a)–(c), for the major, minor and PA=108° axes, respectively. No obvious features are evident.

NGC 7192. The photometric profiles for NGC 7192 are shown in Figs 18(a)–(c) for the *B*, *V* and *R* filters, respectively (panels as in Fig. 1). The galaxy is very regular and round. The $(B-R)$ colour profile, plotted in Fig. 19, is rather steep.

The stellar kinematic profiles of NGC 7192 are shown in Figs 20(a)–(c), for the major, minor and PA=65° axes, respectively (panels as in Fig. 3). Peculiar core kinematics are observed, i.e. the innermost ≈8 arcsec rotate faster and in

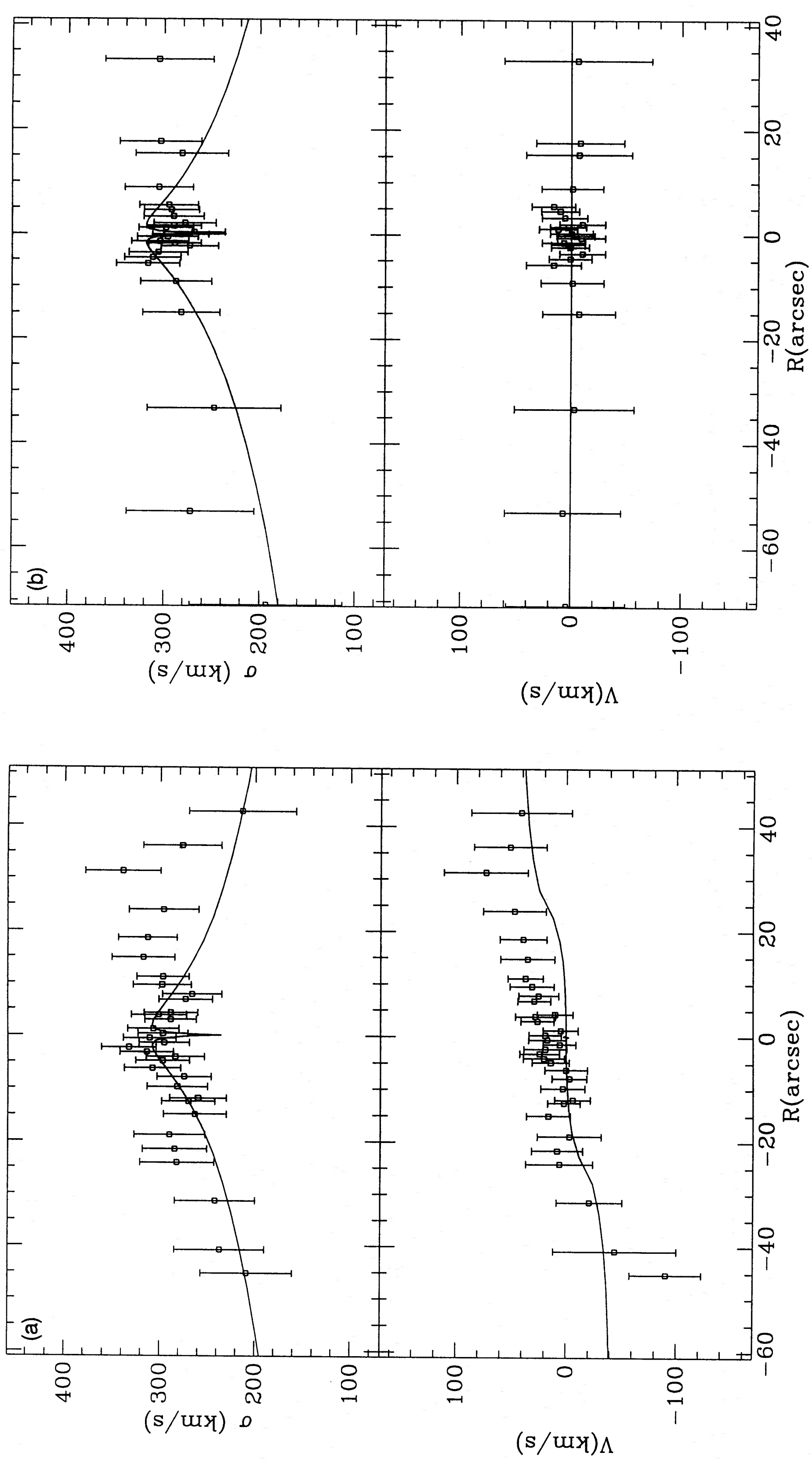

Figure 3. (a) Rotation velocity (lower) and velocity dispersion (upper), both in km s^{-1}, as functions of radius (in arcsec) for the major axis of NGC 439. (b) As (a), for the minor axis of NGC 439. Solid lines are the best-fitting dynamical model to the two axes (see text).

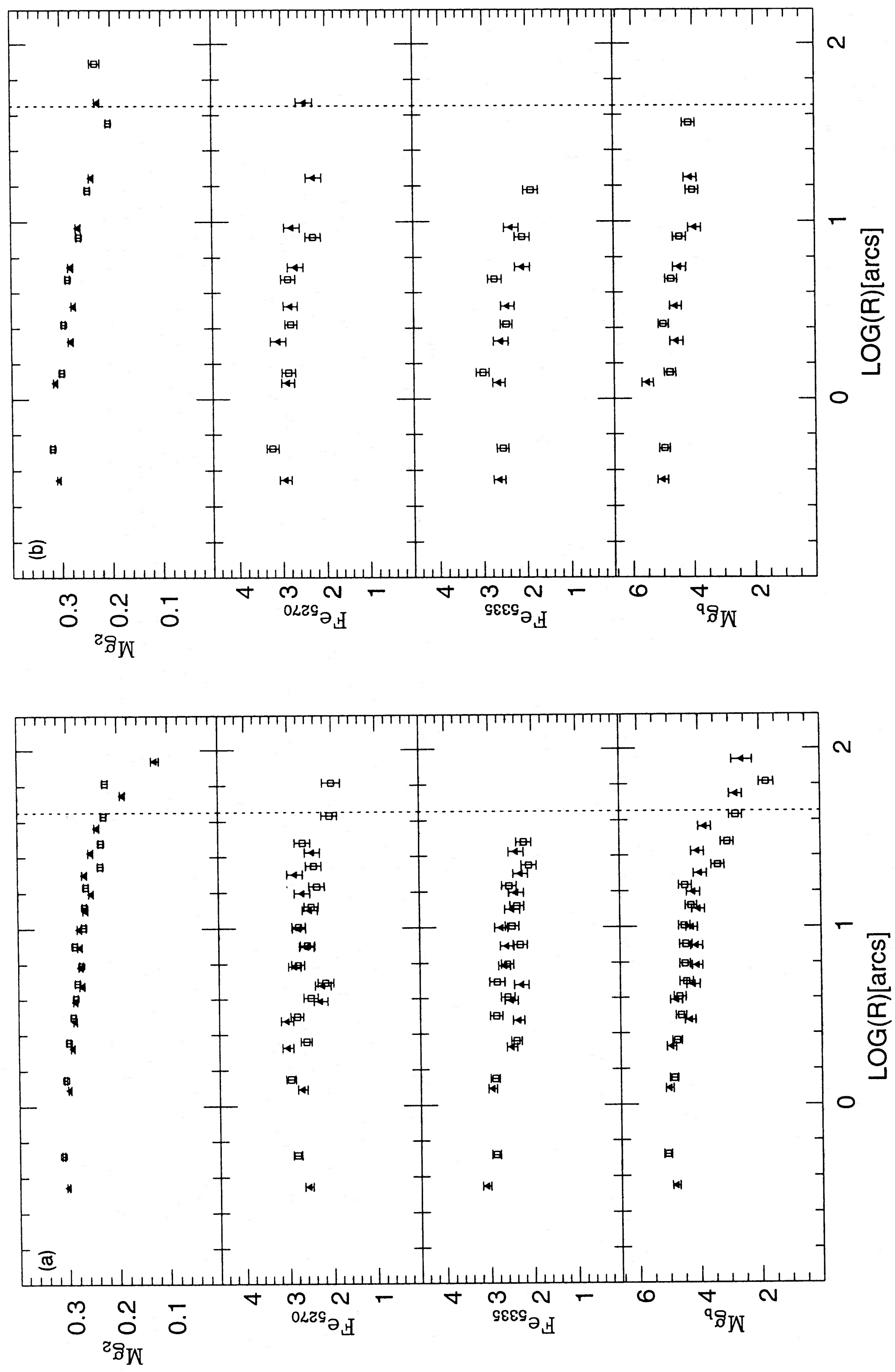

Figure 4. (a) Mg_b (lower), Fe_{5335} (second from bottom), Fe_{5270} (second from top; all the last three indices in Å) and Mg_2 (upper; in mag), as functions of $\log_{10}$(radius) (in arcsec) for the major axis of NGC 439. (b) As (a), for the minor axis of NGC 439.

the direction counter to the bulk of the galaxy (whose kinematics along any of the three axes observed is consistent with no rotation).

The line-strength profiles of NGC 7192 are shown in Figs 21(a)–(c) for the major, minor and PA=65° axes, respectively. As in NGC 2434, a strong enhancement of Mg_2 and a moderate enhancement of ⟨Fe⟩ is observed in the core region (see Fig. 22, where the Mg_2 and ⟨Fe⟩ indices and the rotation velocity are plotted together on a linear radial scale).

4 AXISYMMETRIC DYNAMICAL MODELLING

Following the approach introduced by Binney, Davies & Illingworth (1990), already used in Paper I (see also references therein), we have used a family of axisymmetric dynamical models to derive information on the dynamical state and structure of the galaxies of the sample, from their measured photometric and kinematic profiles. The galaxies are described with a modified Jaffe (1983) mass density

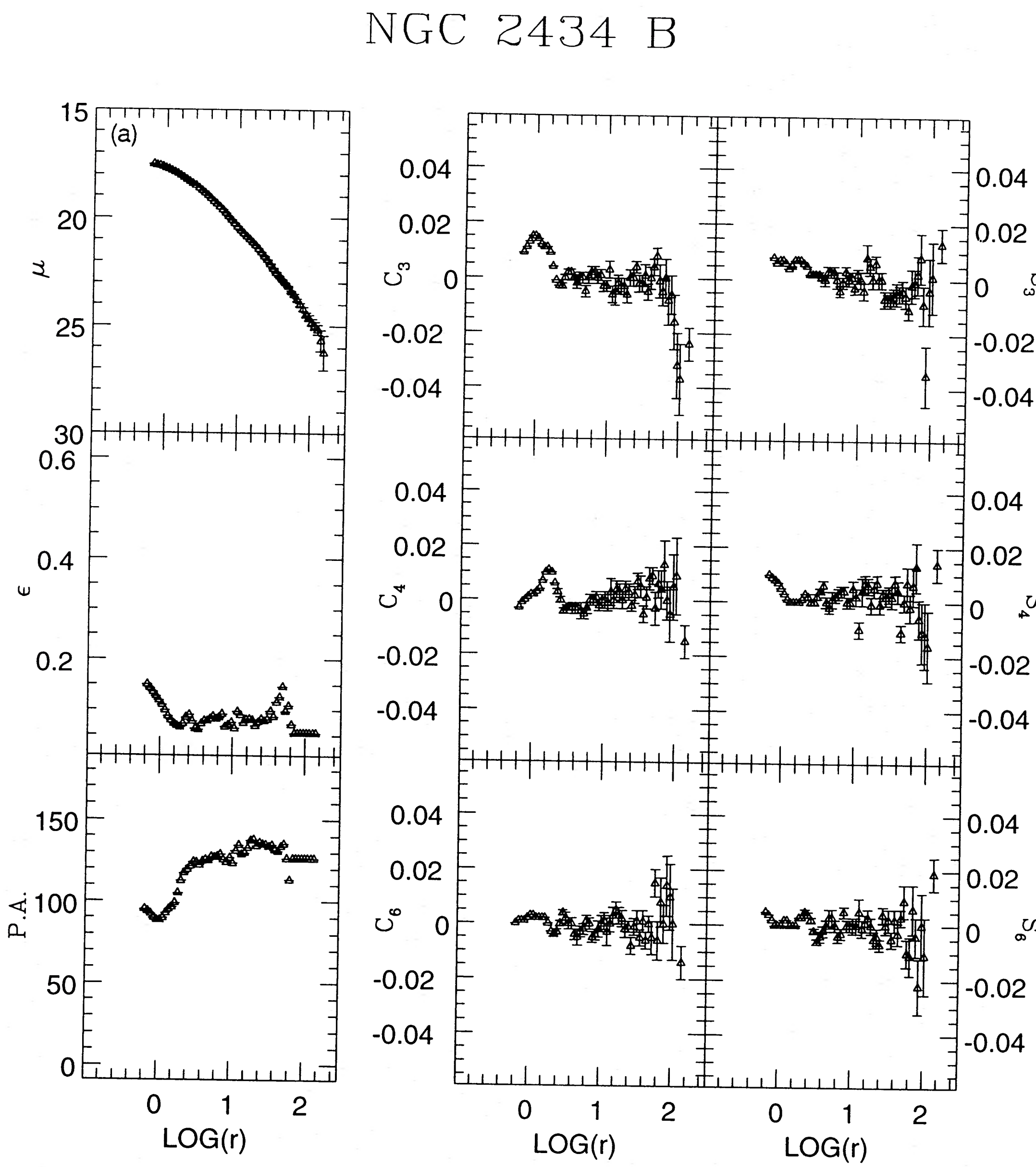

Figure 5. (a) *B* photometry for NGC 2434. Left panel: surface brightness (upper), ellipticity (central), major axis position angle (lower). Right panel: C_i (left) and S_i (right) coefficients ($i=3$, 4, 6 from top to bottom). Abscissa is $\log_{10}$(radius), in arcsec. (b) As (a), for the *V* band of NGC 2434. (c) As (a), for the *R* band of NGC 2434.

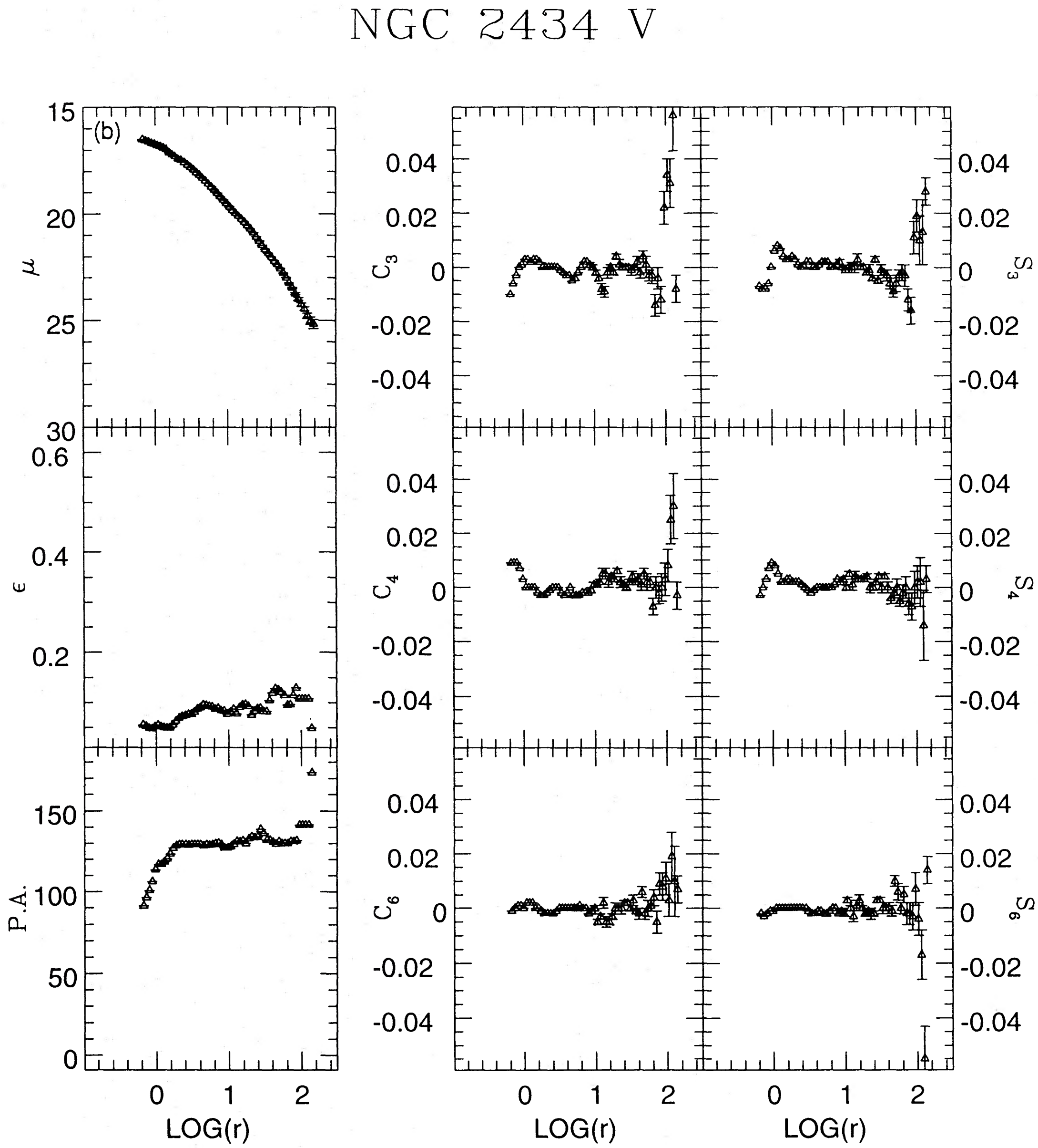

Figure 5 – *continued*

profile, which is fitted to the observed light curve to derive the scalelength for the dynamical model. With the assumption of a distribution function dependent only on the energy E and on the z-component of the angular momentum L_z, the Jeans equations of stellar equilibrium are solved to derive, for oblate models, the theoretical rotation velocity and velocity dispersion profiles. Prolate rotators are also modelled, by assuming the longest axis to be the symmetry axis; in that case the separation between ordered and random motion is unnatural, and the total azimuthal velocity $\langle v_\phi^2 \rangle$ is fitted to the quantity (σ^2+v^2) derived from the observed σ (velocity dispersion) and v (rotation velocity) profiles. For a more detailed description of the models and of the steps leading to the best-fitting parameters, we refer to Paper I.

For each galaxy, the results are summarized in the following.

NGC 439. Both the rotation velocity and the velocity dispersion profiles of NGC 439 are reasonably well fitted by an edge-on, rotating, oblate model, with flattening equal to the (averaged) observed one (E2; see solid line in Fig. 3). The luminous mass inferred from the model is 1.2×10^{12} $M_\odot$, and the corresponding M/L is 19 $M_\odot/L_{\odot B}$. A dark halo is not required to fit the available data. However, the data extend until only one half-light radius, and it is therefore not appropriate to draw any strong inference from them about the amount and distribution of dark matter. This galaxy has an ellipticity that changes substantially with the radius; our modelling (at constant ellipticity) might thus lose some details of its dynamical structure.

NGC 2434. The kinematic profiles of NGC 2434 are well fitted by both an oblate and a prolate model. The best-fitting oblate model (solid line in Fig. 7) has a flattening of E3 and a viewing angle of about 60°; it is surrounded by a spherical

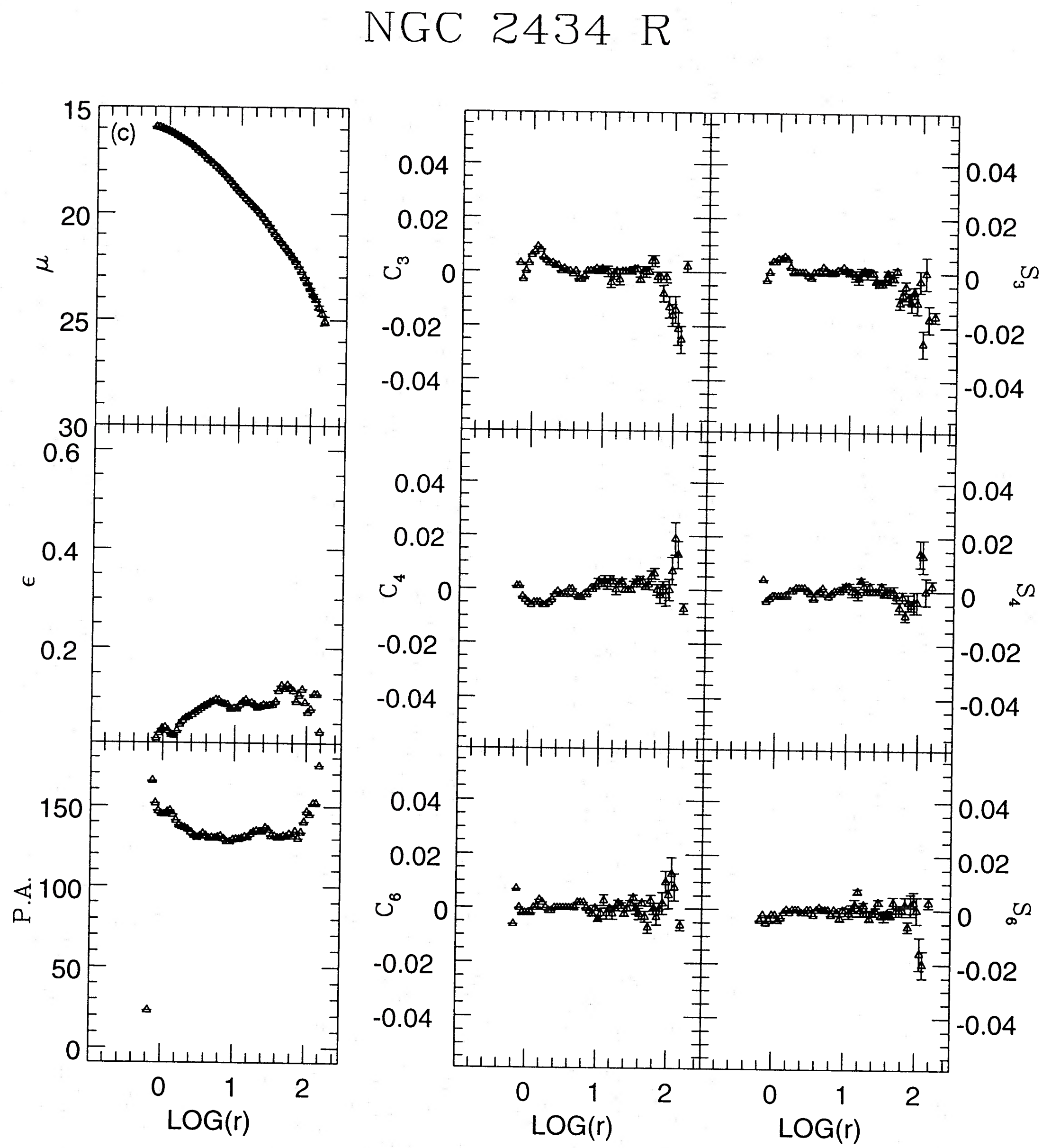

Figure 5 – *continued*

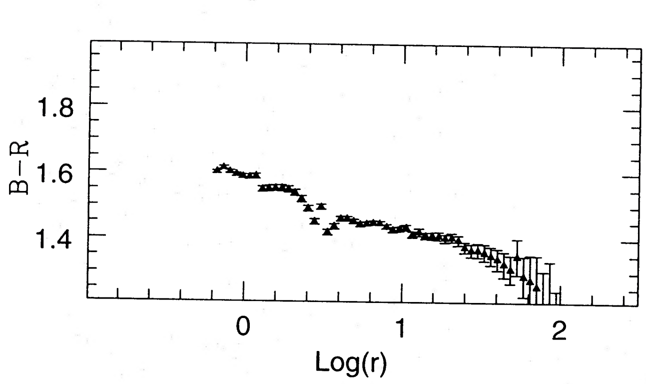

Figure 6. As Fig. 2, for NGC 2434.

dark halo with dark to luminous matter ratio ≈ 2 and dark to luminous scalelength ratio ≈ 2.5. The luminous mass inferred from the model is 5.7×10^{10} $M_\odot$, and the corresponding M/L is 4.4 $M_\odot/L_{\odot B}$.

The best-fitting prolate model (dashed line in Fig. 7) has an E4 flattening and is seen at an angle of about 45°. (For simplicity we have superimposed the fit, made to the total $\sigma^2 + v^2$ profile, to the velocity dispersion measurements. The contribution of rotation is very small, and would not change the visual representation significantly.) A spherical dark halo is required, three times as massive and twice as diffuse as the luminous matter. The luminous mass inferred from the model is 4.7×10^{10} $M_\odot$, and the corresponding M/L is 4 $M_\odot/L_{\odot B}$.

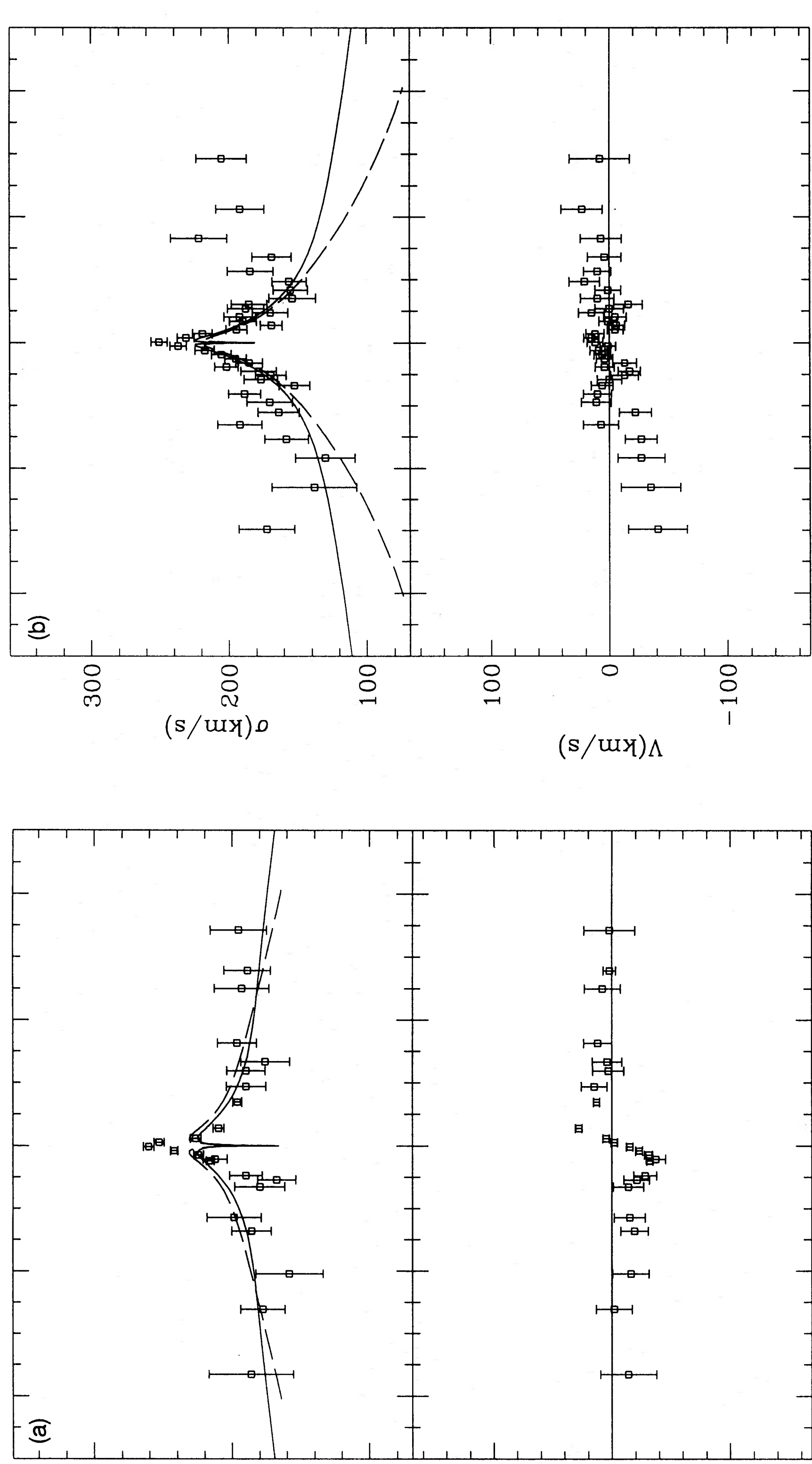

Figure 7. (a) and (b) As Fig. 3, for NGC 2434. (c) PA = 90°. Solid lines are the best-fitting oblate dynamical model to the three axes; dashed lines are the best-fitting prolate model (see text).

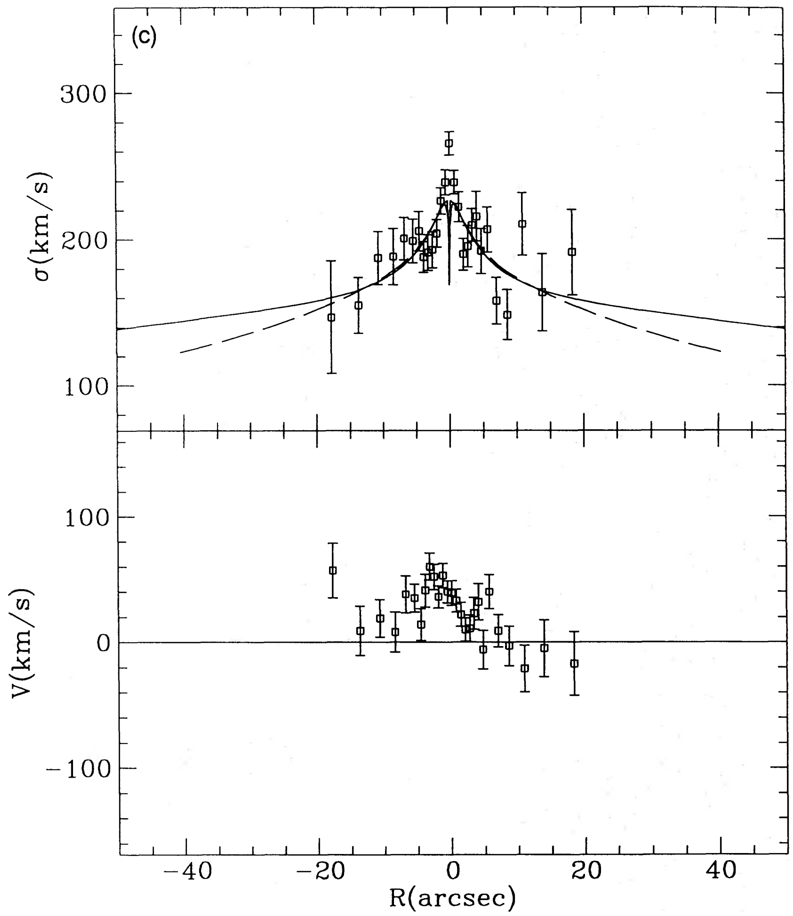

Figure 7 – *continued*

Independent of the particular model, NGC 2434 thus seems to be a pressure-supported stellar system $[(V/\sigma_{\rm intrinsic}) \leq 0.1]$, seen at an intermediate viewing angle and surrounded by a massive dark halo.

For both shapes, a rather large range of models is able to fit the data, as might be expected, given the small observed flattening of this galaxy. Acceptable models give luminous masses up to 6×10^{10} $M_\odot$.

NGC 3706. The rotation velocity and velocity dispersion profiles of NGC 3706 are very well fitted by an oblate model with fast rotation $[(V/\sigma_{\rm intrinsic}) \geq 1]$. From the model (solid line in Fig. 12), the galaxy is a very flattened rotator (E6), seen close to face-on (at about 25°); it is surrounded by a dark halo at least as massive as the luminous galaxy, with a scale-length twice as large as the luminous scale and with the same flattening as the luminous component. The luminous mass inferred from the model is 4.5×10^{11} $M_\odot$, and the corresponding M/L is 6.6 $M_\odot/L_{\odot B}$.

NGC 6407. The data for NGC 6407 present a sizeable scatter which makes it difficult to formulate very firm conclusions. The best-fitting model is an E5 object, seen at an angle of 35° (solid line in Fig. 16). Dark matter is not required to fit the data, which, however, sample only the region inside $\approx 1.3 R_e$. The luminous mass inferred from the model is 1.8×10^{12} $M_\odot$, and the corresponding M/L is 29 $M_\odot/L_{\odot B}$. In addition, this galaxy has an ellipticity that changes substantially with the radius, so that, as in this case of NGC 439, our modelling, performed at constant ellipticity, might not account for all the features present in the galaxy.

NGC 7192. As the projection of NGC 7192 on the sky is round, a rather wide range of models is able to fit the data (which are insufficient to remove the degeneracy in the allowed triaxial shapes). Both prolate and oblate models have been fitted to the data.

The best-fitting oblate model (solid line in Fig. 20) is almost round, and it is seen edge-on. It is surrounded by a flattened (E6) dark halo, twice as massive and three times as extended as the luminous galaxy. The luminous mass inferred from the model is 4×10^{11} $M_\odot$, and the corresponding M/L is 15 $M_\odot/L_{\odot B}$.

The best prolate model (dashed line in Fig. 20; again, the best fit to $\sigma^2 + v^2$ is superimposed on the velocity dispersion measurements) gives a more satisfactory fit along the minor axis, but a less satisfactory one along the major axis. Also in this case, the galaxy is rather round and the major axis is roughly perpendicular to the line of sight. A flattened (E3), twice as massive and doubly extended dark halo

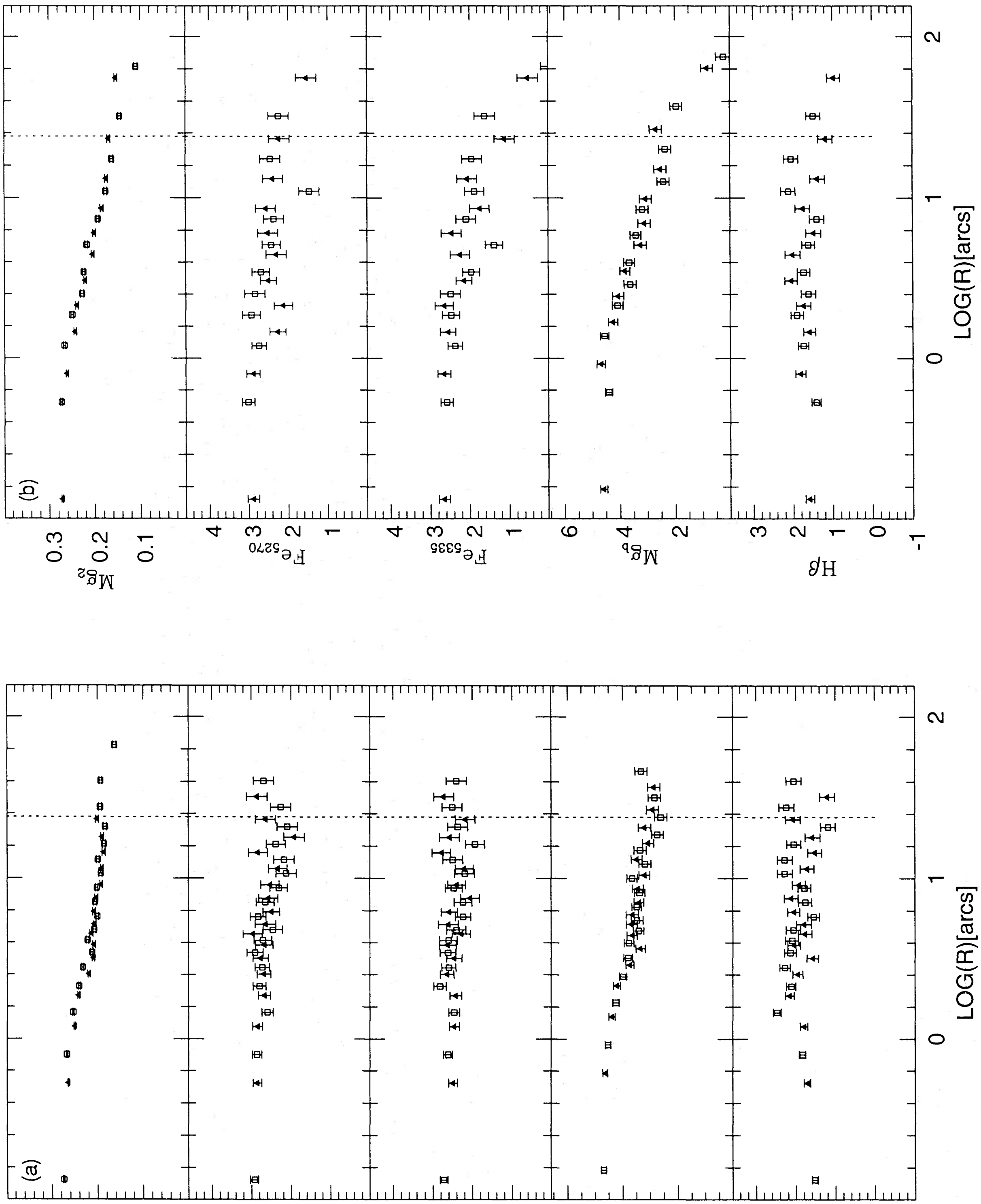

Figure 8. (a) Hβ (lower), Mg_b (second from bottom), Fe_{5335} (third from bottom), Fe_{5270} (second from top; all the last four indices in Å) and Mg_2 (upper; in mag), as functions of $\log_{10}$(radius) (in arcsec) for the major axis of NGC 2434. (b) As (a), for the minor axis of NGC 2434. (c) As (a), for PA = 90°.

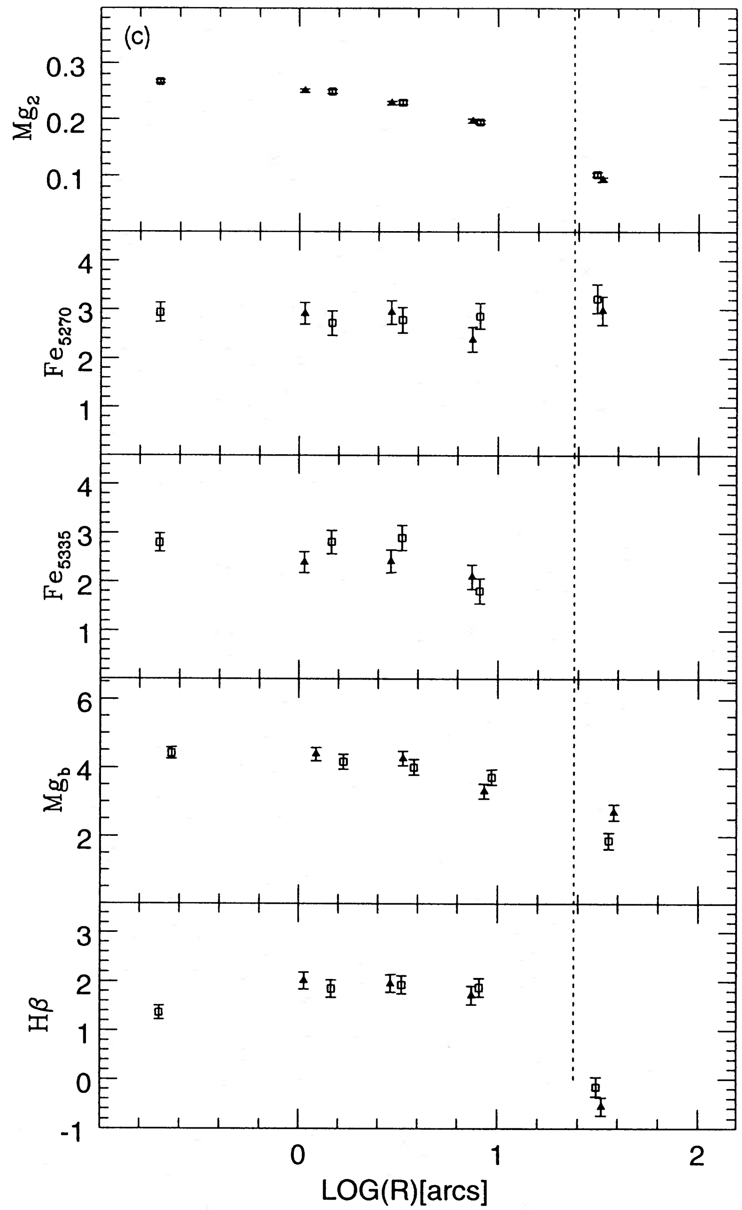

Figure 8 – *continued*

surrounds the luminous galaxy. The luminous mass inferred from the model is 4.8×10^{11} $M_\odot$, and the corresponding M/L is 18 $M_\odot/L_{\odot B}$.

5 DISCUSSION

To date, how and when galaxies formed has been a crucial, open question. With the current knowledge and instrumental tools, attempts can be made to put strong constraints on and reduce the many alternatives to a few plausible scenarios. For example, depending on the type of dark matter and on the primordial fluctuation spectrum, cosmological simulations make such different predictions about the statistical distribution of the shapes of dark haloes, that delineating the shape of dark haloes for a large, statistically significant sample of galaxies would justify by itself the efforts spent in detailed studies of galactic dynamical fields. The discovery of the relation between central velocity dispersion and line strength (Terlevich et al. 1981) has, however, shown that dynamics and stellar populations are very closely related, although not in a simple way, as, for example, (i) the relation between σ and Mg_2 index among nuclei seems different from the relation within galaxies (DSP); (ii) the behaviour of different metallicity indicators as a function of σ is not always the same, i.e. it seems as if the abundance ratio between Mg and Fe increases as a function of galaxy mass, or that most bright galaxies have suffered from Mg-enriching, occasional star formation bursts in their nuclei (WFG; DSP; CDB).

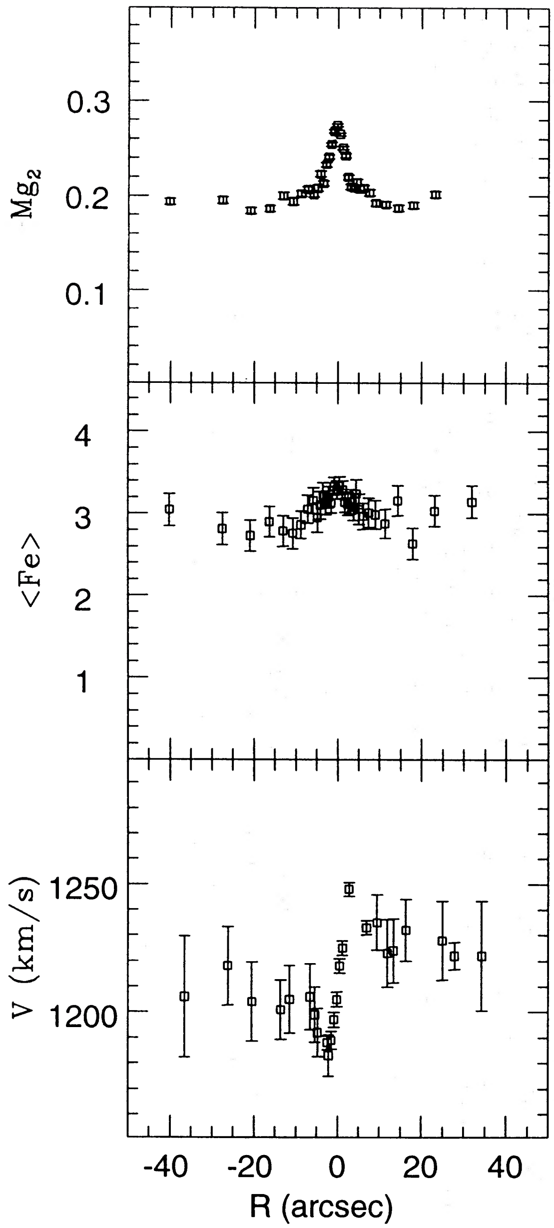

Figure 9. Mg_2 (upper), ⟨Fe⟩ (central) and rotation velocity (lower), as functions of radius (in arcsec) for NGC 2434.

Thus it appears that, in order to reconstruct how galaxies formed from diffuse material in space, it is necessary to study not just their shapes and kinematics, but also their stellar populations, in order to understand, for example, (i) what is the connection between the dynamical structure and the distribution of metallicity and abundance ratios within elliptical galaxies; (ii) whether the observed peculiarities in the inner regions of both kinematic and metallicity profiles are an artefact of projection of highly triaxial systems, or are signatures of additional star formation events; (iii) what are the intrinsic shapes of elliptical galaxies, and what is the connection between intrinsic shapes and the stellar population properties; (iv) whether elliptical galaxies have dark matter haloes, what are the intrinsic shapes of the haloes, what is the connection between the structure of the halo and the structure and population of the luminous galaxy.

To answer these questions, it is necessary to combine (*individually* for each galaxy of a statistically significant sample) the information derived from detailed dynamical modelling with that derived from accurate stellar population modelling. The latter is beyond the purpose of this paper, and will be published separately. In the following we limit our discussion to a presentation of some possible constraints to the above framework, from the observational and theoretical results presented in the previous sections.

5.1 The Mg_2-$(B-R)$ relationship

Since the work of Burstein et al. (1988, hereafter B88), it is known that a rather tight Mg_2-$(B-V)_0$ relationship exists linking the *central* line strength to the *global* galactic colour. This strongly suggests that the nuclear stellar population is closely related to the stellar population of the whole galactic bulk (see also BBF2). Although the more anisotropic galaxies seem to be slightly redder for their values of Mg_2 than isotropic galaxies, this latter result might actually be driven by the inclusion in the sample of galaxies with bluer stellar discs (BBF2 and references therein). It appears, therefore, that colours are able to trace rather well the main features of the rather homogeneous galactic stellar populations. Indeed, when the *local* relationship between colours and line strengths is also explored, it strengthens the evidence that both these observables are mostly measuring small variations in the galactic metallicities, and in a consistent way (see, e.g., DSP). In Fig. 23 the *local* relationship between Mg_2 and $(B-R)$ derived from our data is shown. Only NGC 3706 (triangles in Fig. 23) on this diagram shows a slope different from that of the relationship between nuclear Mg_2 and $(B-R)$ integrated inside 67 arcsec (B87; D87; DSP). It is indeed possible that the light from this galaxy is contaminated by a disc component which makes the galaxy bluer (this hypothesis is supported by the very fast rotation and by the discy isophotes). For the remaining galaxies, an offset of only about 0.05 mag is observed, i.e. the slope within galaxies is equal to that of the $Mg_{2\,\mathrm{nuclear}}$-$(B-R)_{67\,\mathrm{arcsec}}$ relationship. The offset might partially arise from the uncertainties in our photometric calibration; however, an analogous shift was found also by DSP. Thus it seems plausible that it might partially arise from using, without any scaling, integrated and local colours (the former systematically lowered by the presence of small but significant colour gradients). Assuming an average colour gradient in $(B-R)$ of about -0.08 per dex in radius (Franx, Illingworth & Heckman 1989; Peletier et al. 1990), and using a power-law description for the light profiles of ellipticals, one indeed gets a shift of ≈ 0.05–0.07 mag in the $Mg_{2\,\mathrm{nuclear}}$-$(B-R)_{67\,\mathrm{arcsec}}$ relationship, for colours measured in an aperture comparable to the slit used to obtain the Mg_2 values (D87). The above results, taken together, lead one to speculate that stellar populations in *normal* ellipticals are not only rather homogeneous in both metallicity and age *within* galaxies, but also they are not strongly dependent on the details of their orbital structure and their intrinsic shapes (once bulge and disc components are appropriately decoupled).

5.2 The Mg_2–σ relationship

The $Mg_{2nuclear}$–$\sigma_{nuclear}$ relationship is very tight for bright elliptical galaxies (see, e.g., BBF2 and references therein). A large scatter is observed in smaller galaxies. This scatter might hint either at distinct physical processes occurring in massive and small galaxies or at a quantitative difference in, for example, the amount of stellar/gaseous mergers suffered from by the two kinds of systems (BBF1; BBF2). None the less, no significant zero-point difference is observed between dwarf and very bright ellipticals. Thus, although the formation histories of these two families of objects might be quite different, their stellar populations seem to show a close connection with their kinematic temperature (as measured through the velocity dispersion σ). Again, this result hints at a distant connection between the galactic stellar populations and the details of the dynamical structure, as, for example, boxy and discy galaxies, rotating and non-rotating galaxies, field and cluster galaxies basically follow the same $Mg_{2nuclear}$–$\sigma_{nuclear}$ relationship.

Relatively recently, there have been questions about whether the local metallicity within ellipticals is a function only of the local depth of the gravitational potential well (which could be traced also by σ; FI), i.e. whether, for example, the Mg_2–σ relationship holds not only for galactic nuclei but also as a *local* property (FI; see also DSP). In Fig. 24 we plot the *local* Mg_2–σ relationship for the five galaxies of the sample. No significant difference is observed when

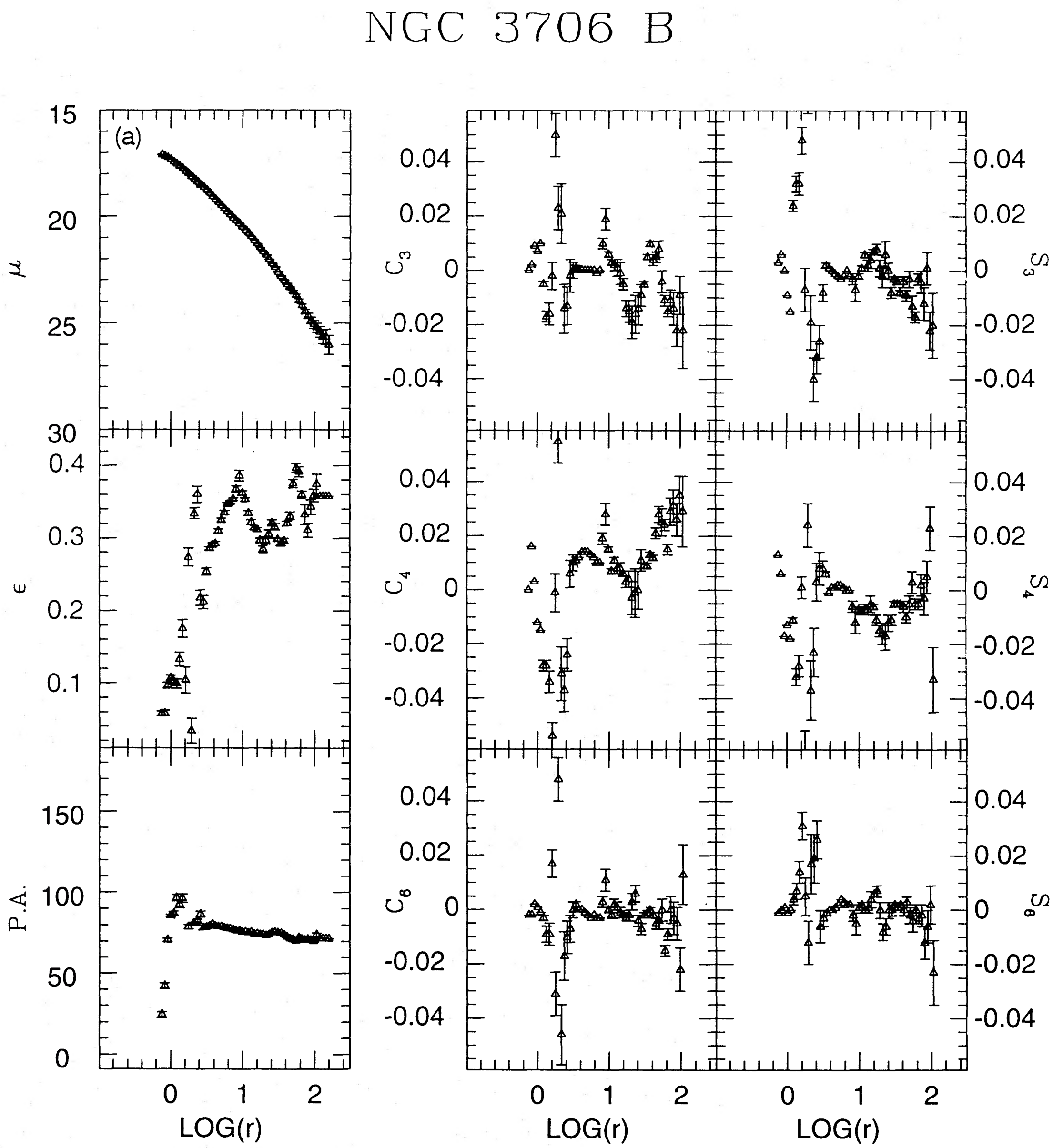

Figure 10. (a) *B* photometry for NGC 3706 (from C93). Left panel: surface brightness (upper), ellipticity (central), major axis position angle (lower). Right panel: C_i (left) and S_i (right) coefficients ($i = 3, 4, 6$ from top to bottom). Abscissa is $\log_{10}$(radius), in arcsec. (b) As (a), for the *R* band of NGC 3706.

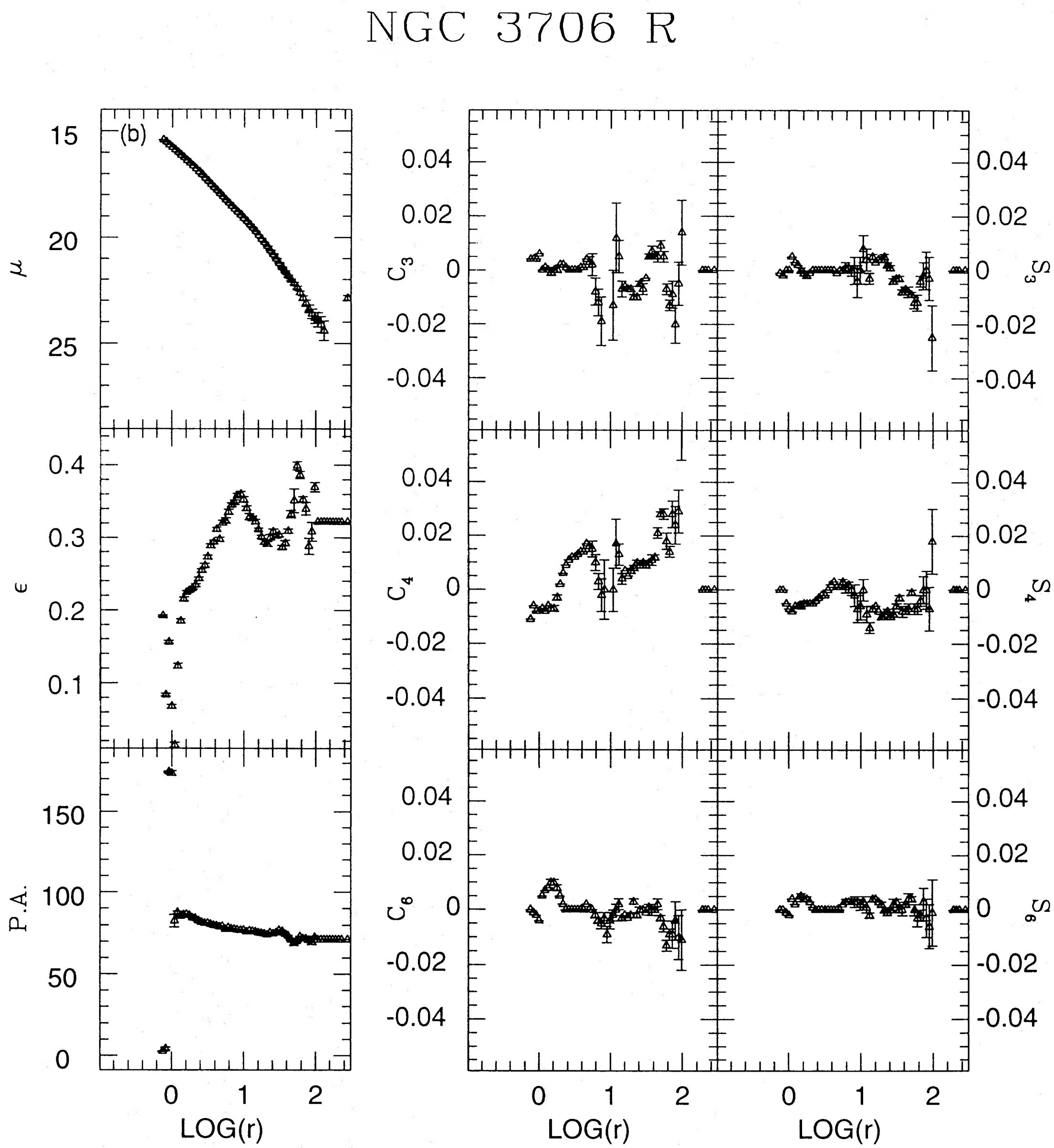

Figure 10 – *continued*

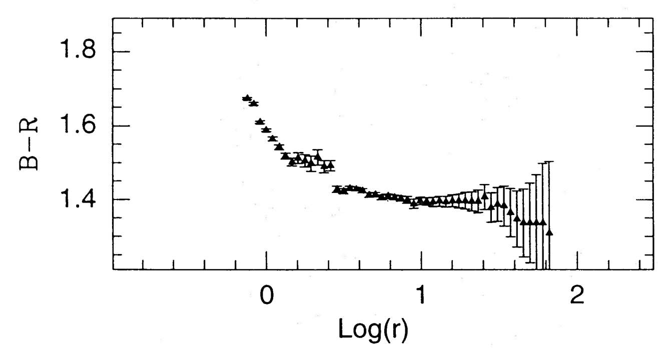

Figure 11. $(B-R)$ versus $\log_{10}$(radius) for NGC 3706 (from C93).

considering the various position angles available. It appears that the points do not lie on a line parallel to that followed by the nuclei, but rather scatter around a steeper line. This has also been noticed by DSP. The very rapid rise in velocity dispersion observed for some of the galaxies of the sample within the innermost few arcsec – to be compared to the central velocity dispersions used to derive the nuclear relationship, which are averaged down inside the area of the used aperture (D87) – increases the discrepancy. Furthermore, the local relationship shows an average spread in Mg_2 of ≈ 0.06 mag at a given value of σ, with a typical scatter from galaxy to galaxy of about 0.04 mag. The latter is twice as large as the typical scatter within a single galaxy (with the exception of NGC 7192). Part of the large global spread might be due to possible systematic differences between the

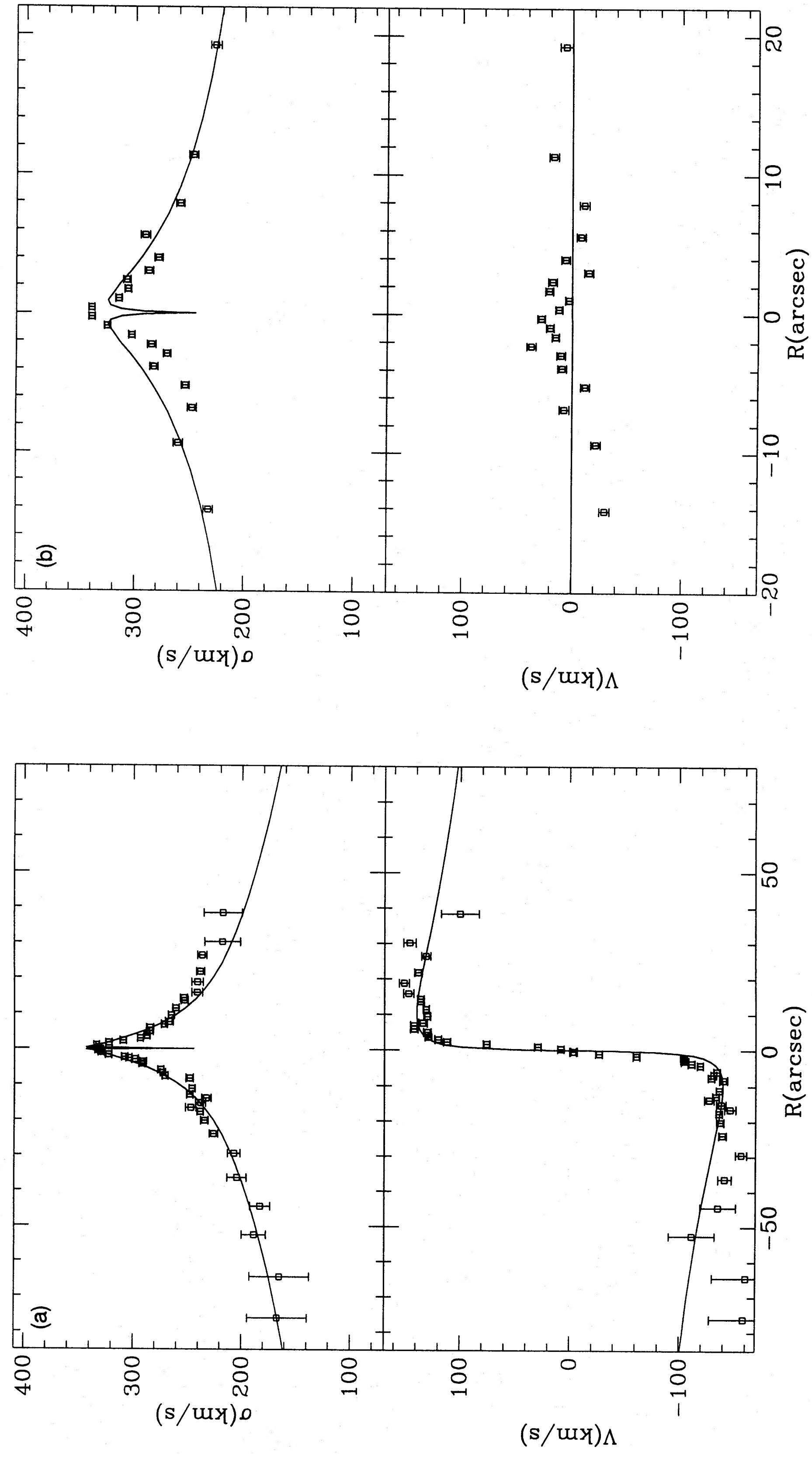

Figure 12. (a) and (b) As Fig. 3, for NGC 3706. Solid lines are the best-fitting dynamical model to the two axes (see text).

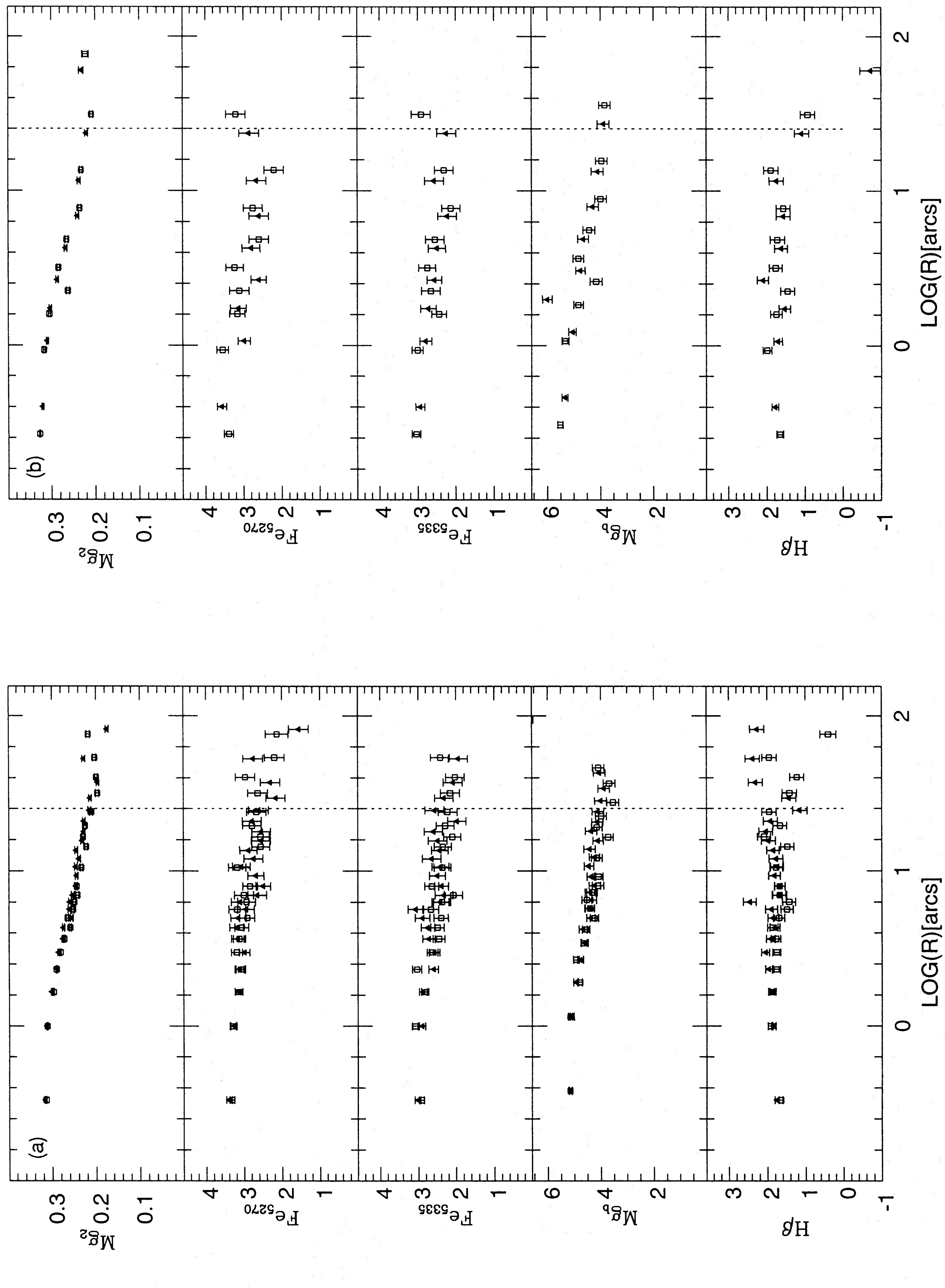

Figure 13. (a) and (b) As Figs 8(a) and (b), for NGC 3706.

NTT and the 2.2-m measurements of velocity dispersion. It seems likely, however, that a residual intrinsic spread remains, since the maximum offset between the NTT and the 2.2-m measurements is estimated to be smaller than ≈ 30 km s^{-1}, since the galaxies observed at the NTT and at the 2.2-m telescope mix in the Mg_2–σ plane, and since a large intrinsic spread is also observed by DSP for a sample of galaxies observed in identical conditions. Thus our results, combined with those of DSP, seem to lead to the conclusion that velocity dispersion and Mg_2 within galaxies are poorly related to one another. This result still needs to be properly understood. In any case, the velocity dispersion seems to be a poor tracer of, for example, the escape velocity from the galactic potential well, a parameter which would appear to be more physically relevant for the problem at hand (see, e.g., FI; DSP).

5.3 The Mg_2–v_{escape} relationship

Fig. 25 shows the *local* correlation between Mg_2 index and escape velocity *within* the five galaxies of the sample. The escape velocity has been derived from the best-fitting dynamical models presented in the previous section. The correlation between Mg_2 and escape velocity is good; the scatter for the sample is, however, larger than that within a single galaxy (a similar result was found by DSP). As all position angles and all models (when more than one model was able to fit the data) give compatible results within each single galaxy, the scatter is plausibly real. A systematic shift of about 25 per cent in velocity is observed with respect to the DSP sample, while the slopes appear to be identical. The shift might be due to the inclusion of massive dark haloes in most of our models. The lack of a significant difference in

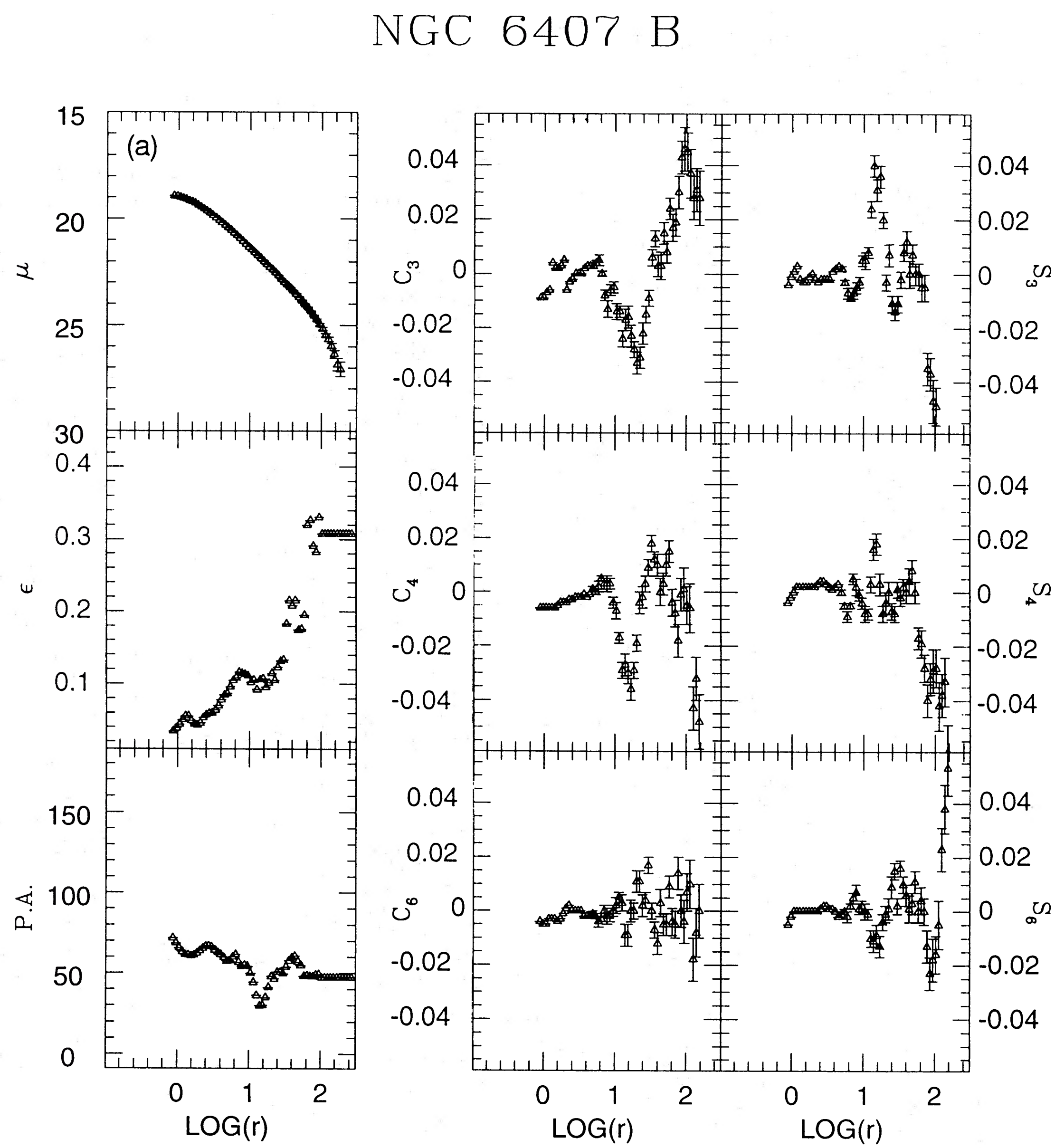

Figure 14. (a)–(c) As Fig. 5, for NGC 6407.

slope for objects such as NC 2434, flattened by velocity anisotropy, and NGC 3706, flattened by rotation, indicates either that no significant flattening of gradients due to radial orbits is present, or that different effects are synchronously acting to smooth down intrinsic differences. Indeed, the above result supports the idea that, to some extent, the galactic metallicity is influenced by the local potential depth; the scatter in the data suggests, however, that some other factor is also contributing in determining the metallicity distribution within elliptical galaxies. As discussed by BBF2, the scatter is well understood in a hierarchical scheme of galaxy formation, as it would be difficult to understand a tight *local* relationship between escape velocity and metallicity in objects that have suffered many merging events. Some other factor must therefore be coupled to any purely dynamical indicator, in order to understand the observed local metallicity distribution in ellipticals.

5.4 The Mg_2–$M^2\rho$ correlation

In the attempt to understand the physical origin of the nuclear Mg_2–σ correlation, BBF2 have noticed that the local stellar density (i) is an indicator of the amount of dissipation occurring during the formation epoch; (ii) reflects the stellar

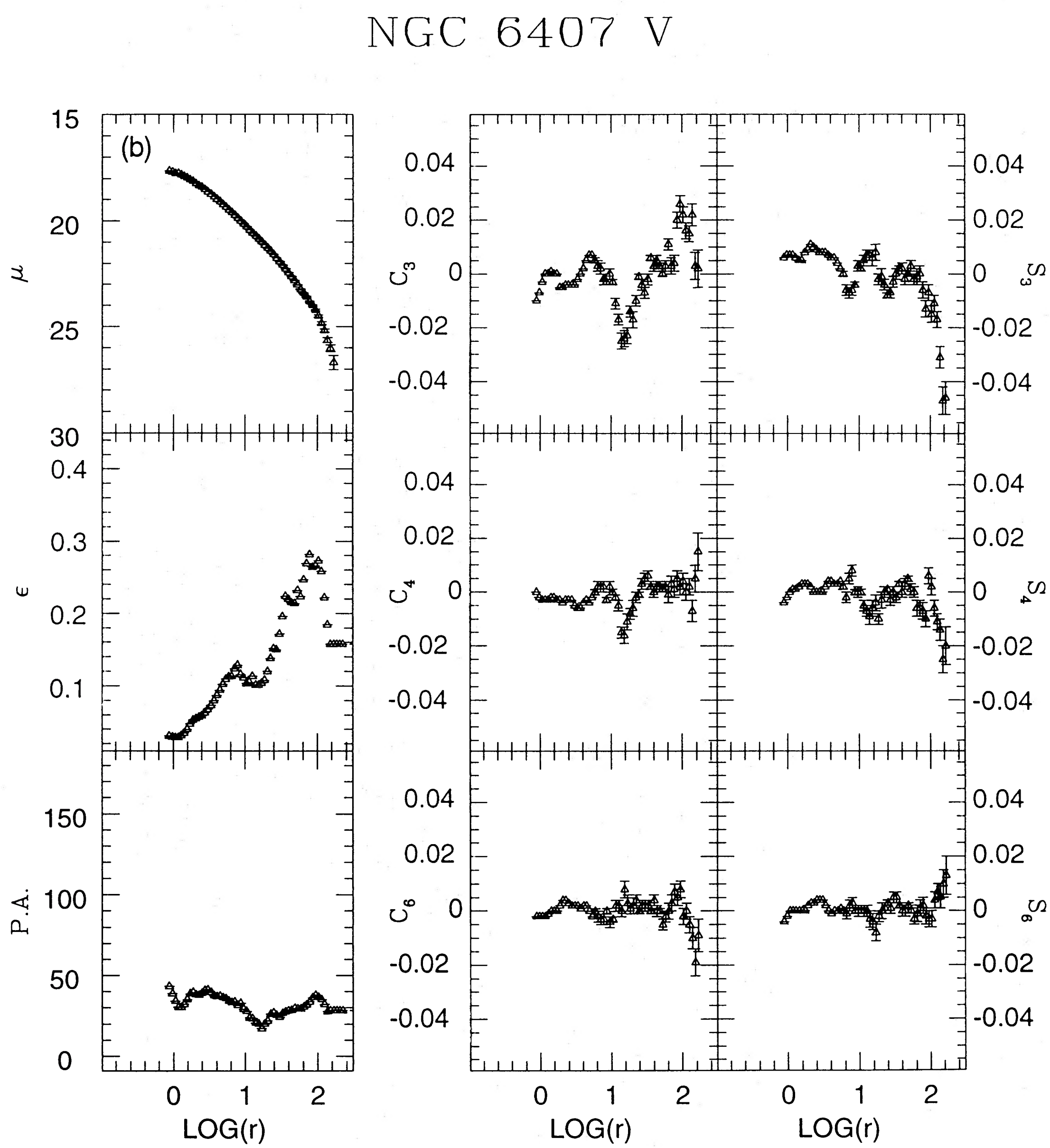

Figure 1 4 – *continued*

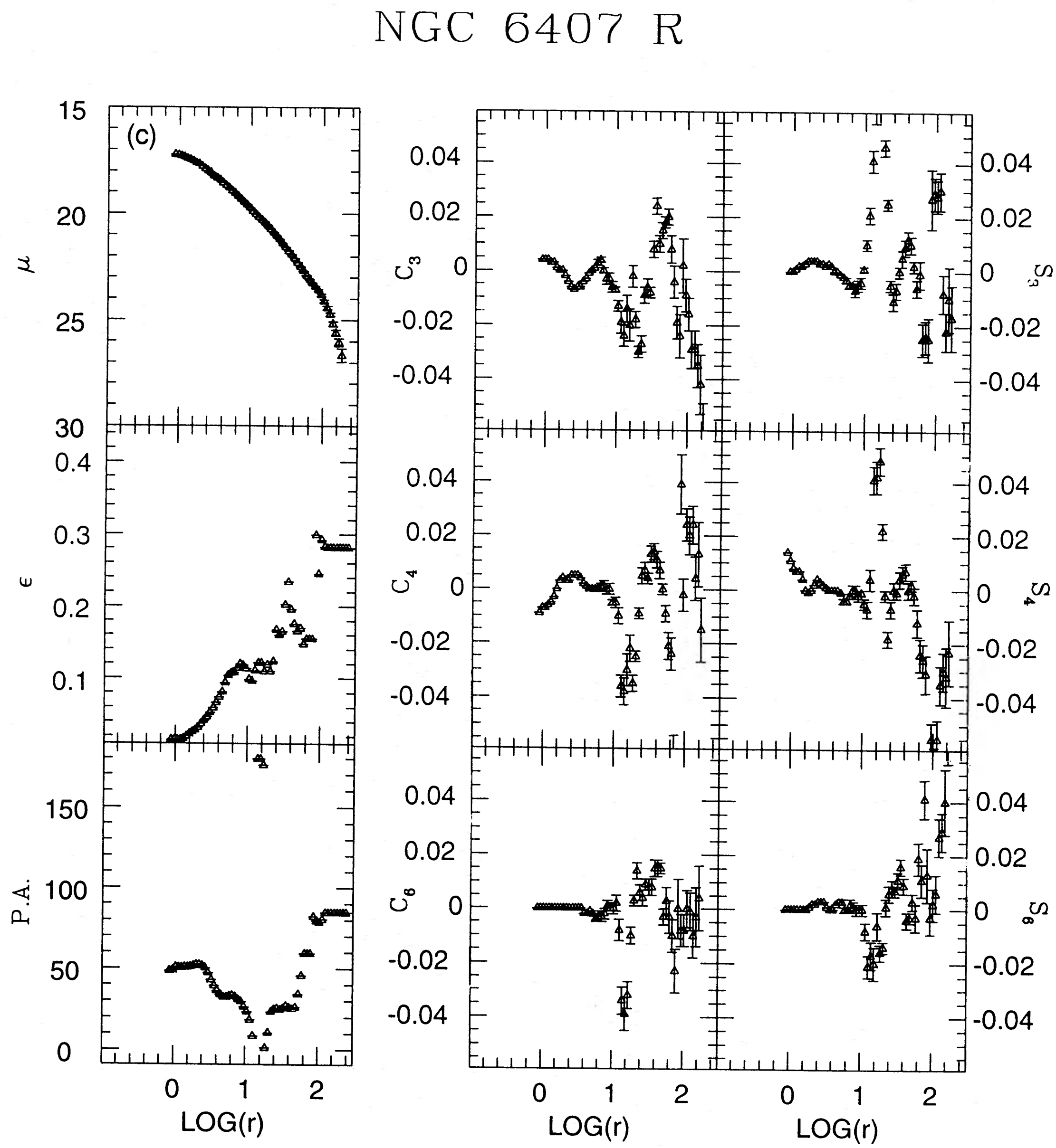

Figure 14 – *continued*

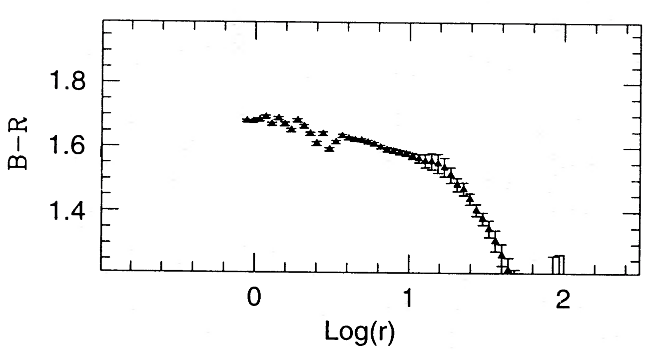

Figure 15. As Fig. 2, for NGC 6407.

density of the merging subunits, and (iii) reflects the efficiency of density-dependent processes such as the cooling rate or the star formation rate. Thus they have represented the stellar population P of an elliptical galaxy as a function of the *total* mass and of the *local* density, i.e. $P=f(M^{\alpha}\rho^{\beta})$. Assuming $M \propto \sigma_0^2 R_e$ and $\langle\rho\rangle \propto M/R_e^3$ (with R_e being the half-light radius), and considering the fit to the observed Mg_2–σ relationship for galactic nuclei, BBF2 have derived $Mg_2 = 0.033\log(M^2\langle\rho\rangle) + \text{constant}$. Although this relationship is, by construction, a different way of expressing the Mg_2–σ_0 relationship that holds for galactic nuclei, it provides a way to investigate the dependence of the metallicity on the stellar density ρ. Should the present stellar

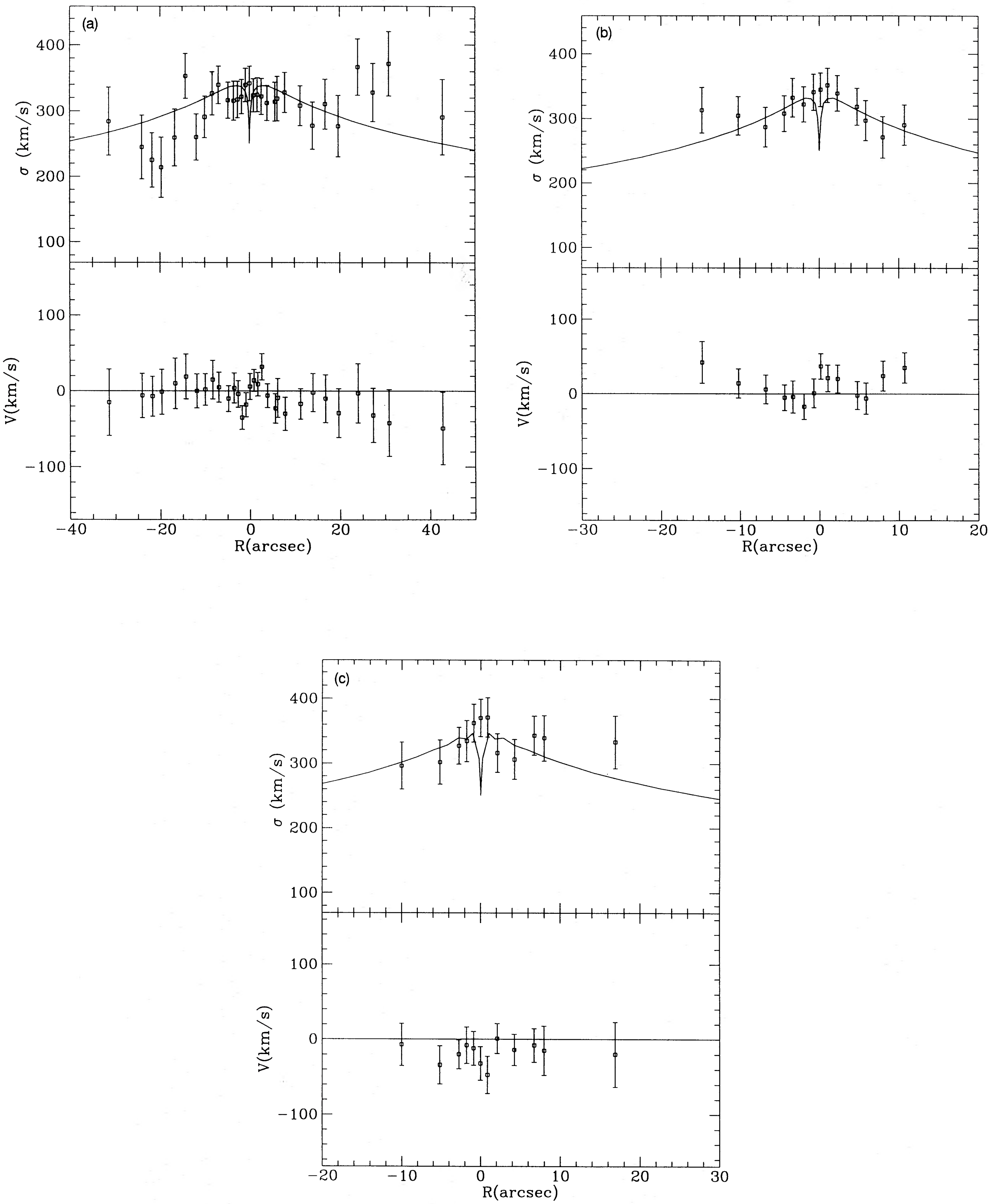

Figure 16. (a) and (b) As Fig. 3, for NGC 6407. (c) PA= 108°. Solid lines are the best-fitting dynamical model to the three axes (see text).

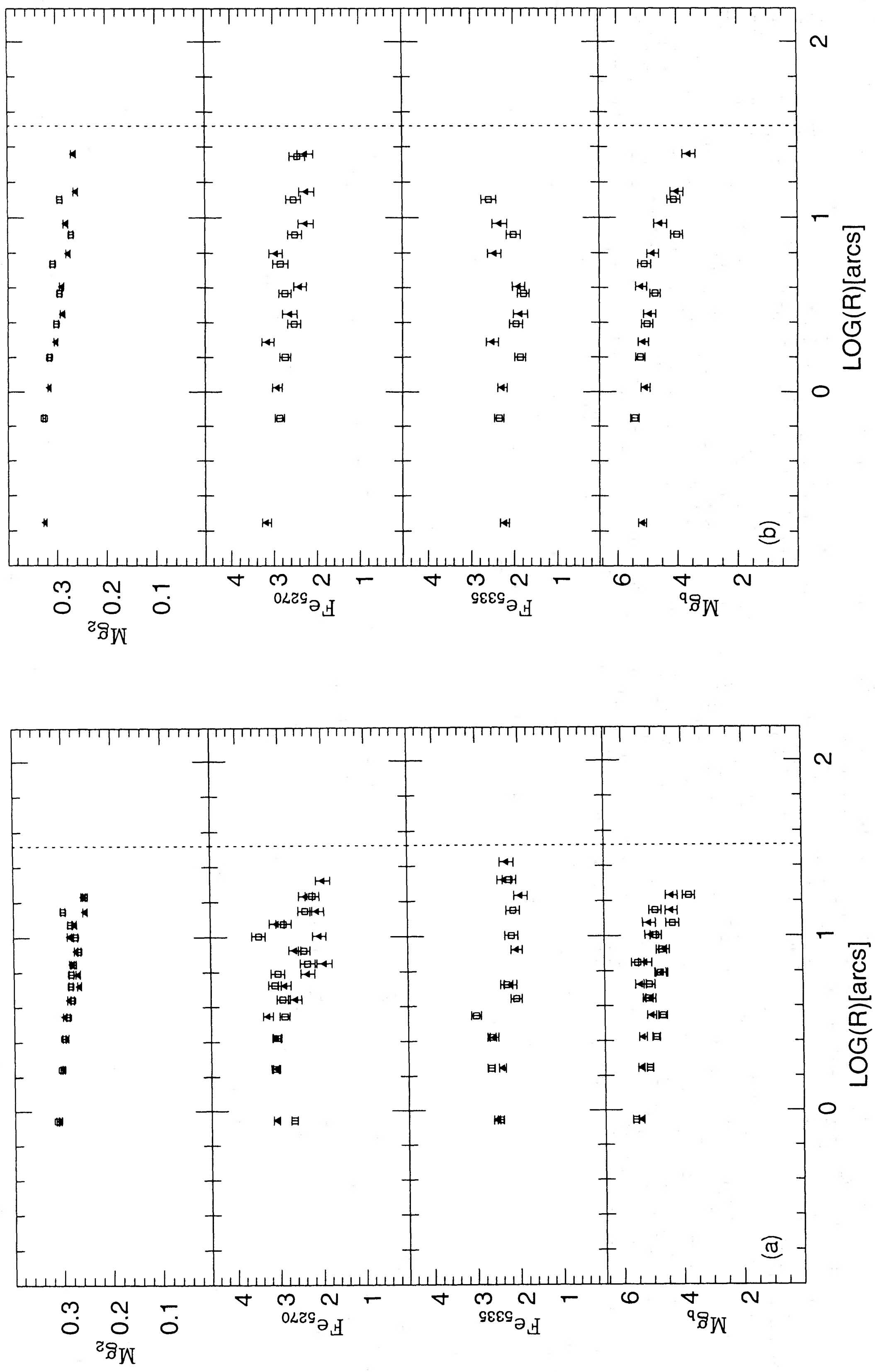

Figure 17. (a) and (b) As Fig. 4, for NGC 6407. (c) PA = 108°.

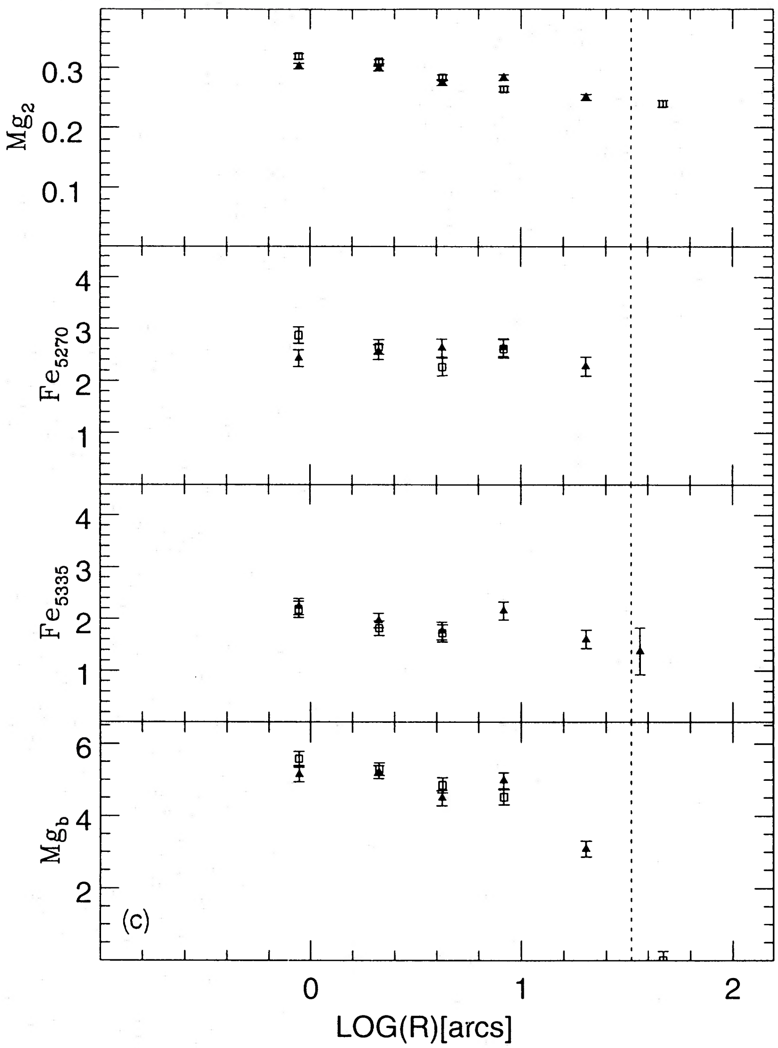

Figure 17 – *continued*

density remember the original mass density, and retain information on the local processes leading to the observed chemical enrichment, one would expect a tight connection between Mg_2 and ρ *within* galaxies as well (once the proper scale for the global galactic mass is again taken into account). We have used the data presented in the previous sections to test the validity of the Mg_2–$M^2\rho$ relationship on a *local* scale, extending to the outermost galactic regions (Fig. 26). In order to do so, we have represented the density ρ through the R-band light profile in mag; this converts the quantity $M^2\rho$ into the quantity $\mu' = \mu_R = 5 \log M$. The masses M used are those derived from the dynamical modelling previously described, although a test has been done by using the mass scale $\sigma_0^2 R_e/G$. The correlation between Mg_2 and μ' *within* the galaxies of the sample is rather good; the slope of the local relationship is consistent with that shown by galactic nuclei. A shift towards higher masses is observed, which could be due to the addition of the matter present in the dark haloes when computing the total M (an addition that reduces the scatter in the relationship). Thus it seems that the proposed combination of a *global* parameter (the galactic mass M, which accounts for the effects of depth of the galactic potential well, such as the retention of supernovae-produced elements and the delay of any galactic wind) and a *local* parameter (the stellar density ρ, as described by the surface brightness, which accounts for the effects of local density driven processes such as the star formation rate) is able to embrace the essential mechanisms leading, even in dynamically different objects such as NGC 2434 and NGC 3706, to the observed metal distribution within galaxies. Still, a significant spread is present. Errors in the photometric calibration alone cannot account for it, while the possibility remains that it is entirely due to uncertainties in the determination of the mass (since, for example, the dark haloes here considered are the 'minimum' allowed by the data). Both the correlation itself and its spread need, however, to be understood in the context of recent studies, which show that giant ellipticals could be much older, could have suffered less dissipation, and could have formed more efficiently and on much shorter time-scales than smaller galaxies (WFG; CDB; Gonzales 1993; Matteucci 1993). This might imply that part of the scatter is 'intrinsic', i.e. caused by a residual dependence on the galactic size (e.g. through differences in the efficiency and time-scale of star formation in larger objects), and that a more accurate determination of the two parameters α and β might be required. More detailed data and modelling, involving deeper theoretical investigations, are called for.

5.5 Pecular kinematics and stellar populations in the cores

Two of the galaxies, NGC 2434 and NGC 7192, show a core that is kinematically decoupled from the bulk of the galaxy. The first examples of core decoupling were reported by Franx & Illingworth (1988), Jedrezejewski & Schechter (1988) and Bender (1988). There, the evidence for an anomaly in the inner regions was only kinematical, and it was thus unclear whether it arose from, for example, projection effects of highly triaxial shapes (see, e.g., Statler 1991). More recently, Bender & Surma (1992) and DSP have studied the Mg_2 radial profiles of some ellipticals with peculiar core

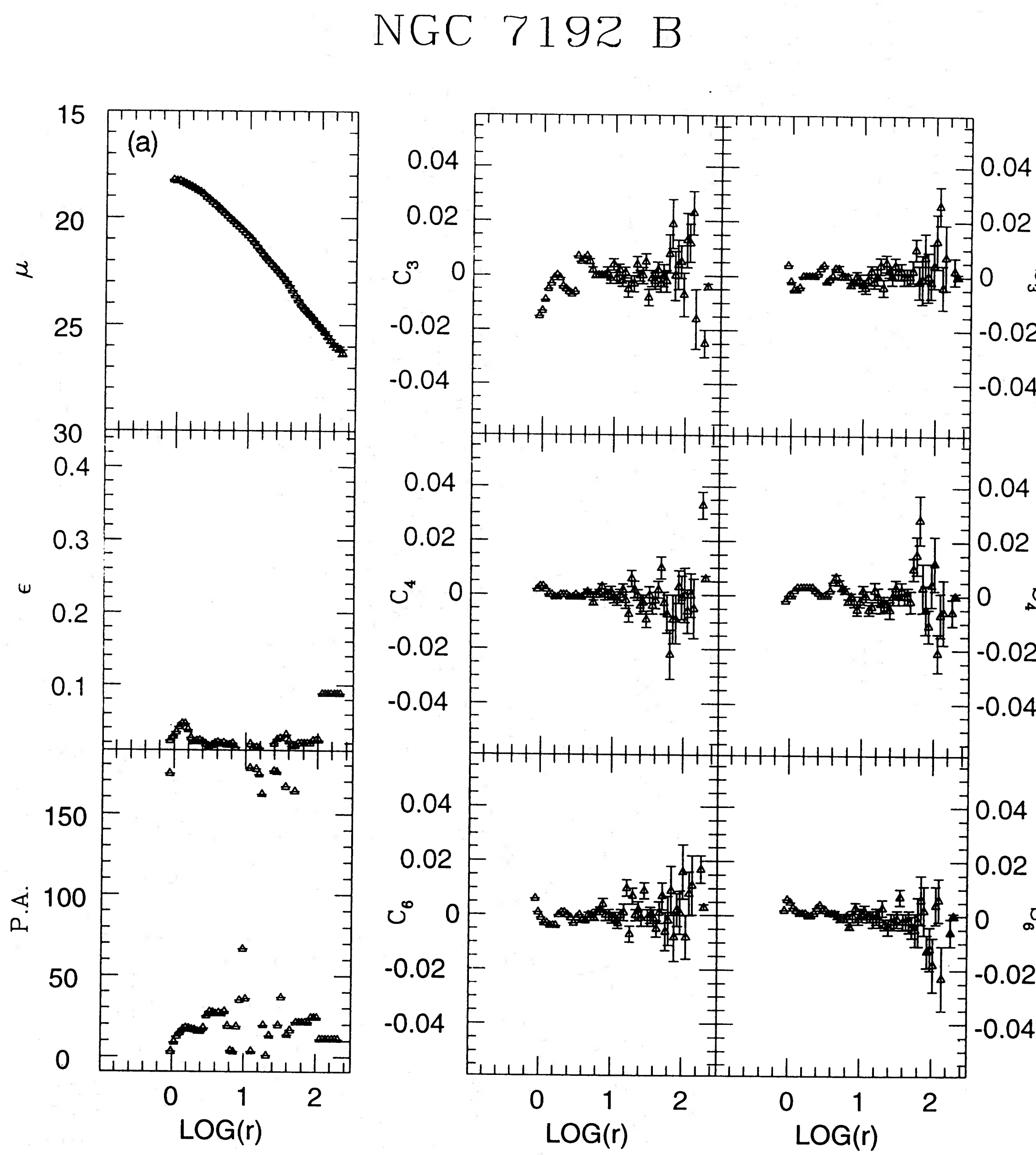

Figure 18. (a)–(c) As Fig. 5, for NGC 7192.

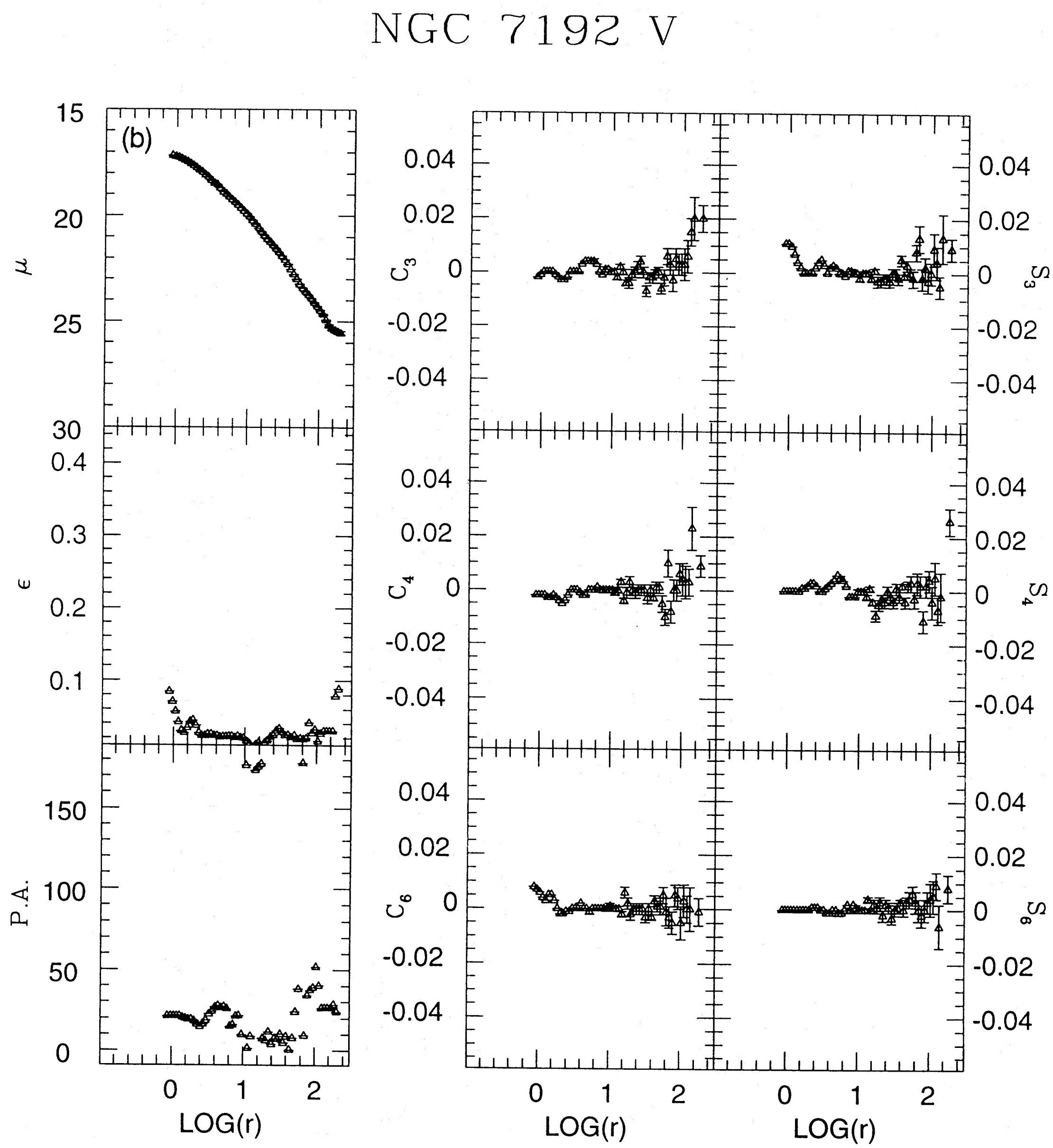

Figure 18 – *continued*

kinematics, and have noticed that such profiles show a sharp change of slope at the radius of the core, i.e. an enhancement in metallicity in the kinematically decoupled inner regions with respect to the main body. Those authors have suggested that such an enhancement might result from star formation episodes following the formation of the bulk of the galaxy, due to possibly already enriched, infalling gas, which might have generated the inner counter-rotating stellar disc also observed in the rotation curve (see also BBF2). The two galaxies NGC 2434 and NGC 7192 present the same anomalous features, i.e. their Mg_2 profiles show a sudden rise in the radial slope at the radii of the kinematically decoupled cores. The same qualitative behaviour is observed also in their ⟨Fe⟩ profiles, although, there, the rise is less sharp and the relative enhancement of this index appears much more moderate. This latter result strengthens the suggestion that a later star formation event has produced the counter-rotating stellar disc in the core, and suggests that such an event has occurred on relatively short time-scales. An enhanced [Mg/Fe] is in fact what one might expect to observe if the star formation episode had occurred on time-scales shorter than those typical of (iron-producing) Type Ia supernovae. Although the statistics are not yet large, it seems that such inner stellar discs are a rather common phenomenon in the

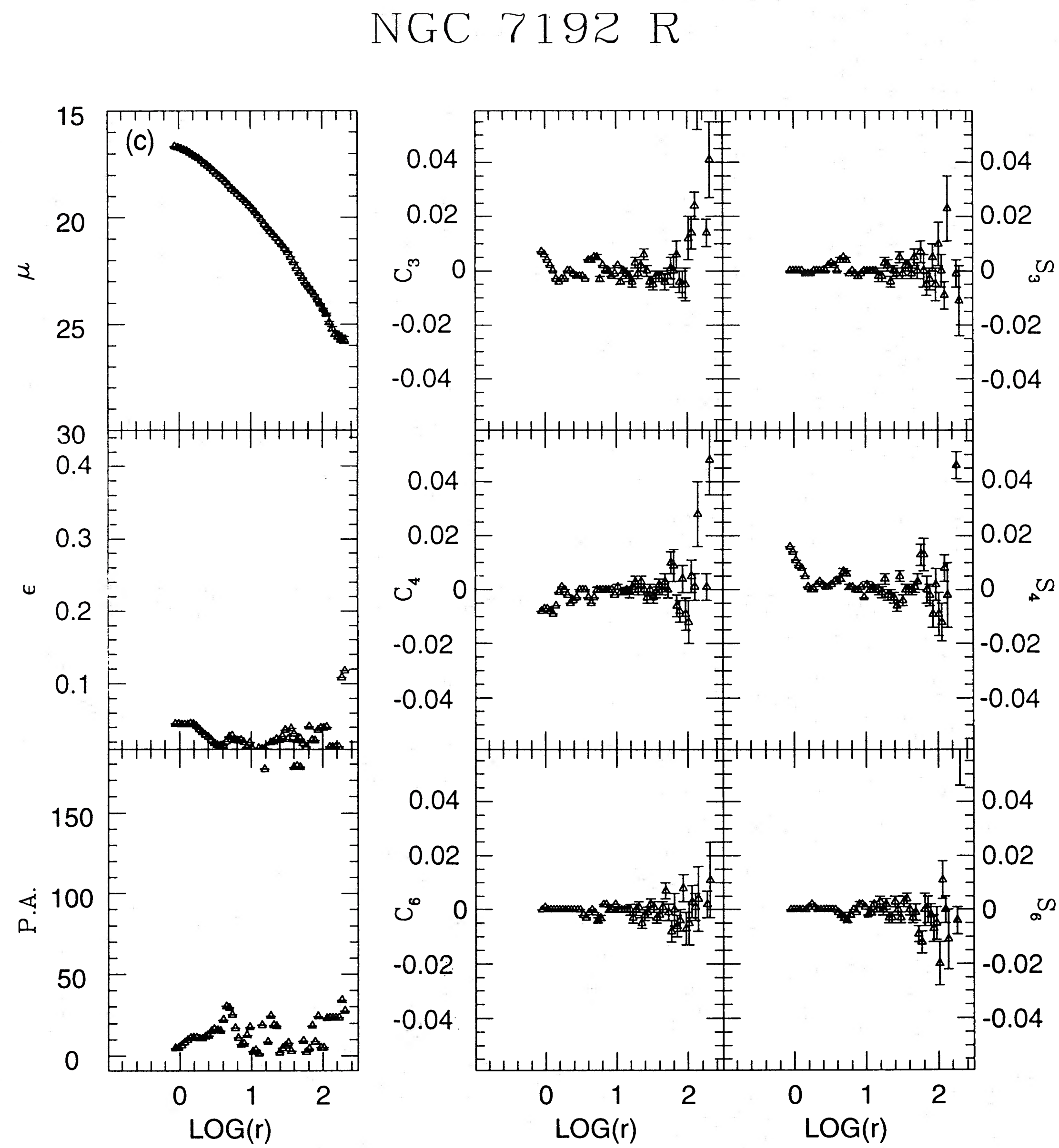

Figure 18 – *continued*

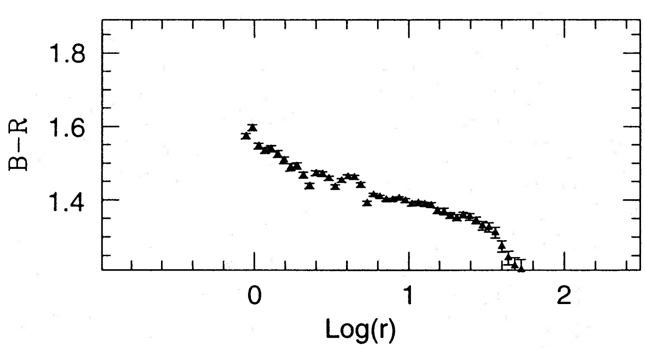

Figure 19. As Fig. 2, for NGC 7192.

cores of elliptical galaxies, as demonstrated by the normal occurrence of discy isophotes in the core of large boxy ellipticals (Nieto et al. 1991).

5.6 The Mg_2–⟨Fe⟩ relationship

Fig. 27 shows the local correlation between the Mg_2 and the ⟨Fe⟩ indices for the five galaxies of the sample. The solid line indicates the correlation observed for the ellipticals' nuclei (Burstein et al. 1984). The effect already pointed out by WFG, DSP and CDB of a statistically steeper dependence of ⟨Fe⟩ on Mg_2 within galaxies, with respect to galactic nuclei, is also observed here. Despite the many hints for a general

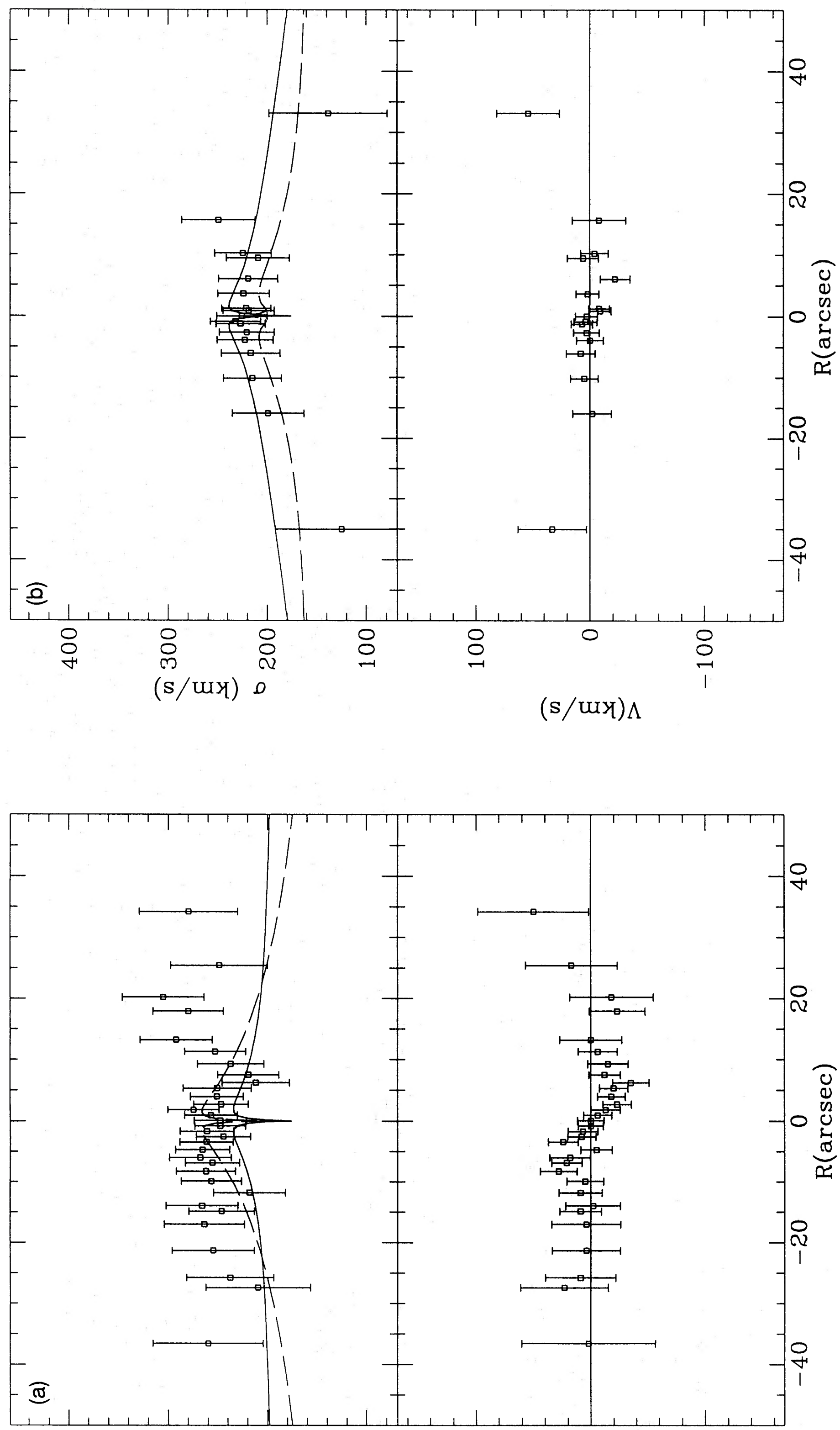

Figure 20. (a) and (b) As Fig. 3, for NGC 7192. (c) PA = 65°. Solid lines are the best-fitting oblate dynamical model to the three axes; dashed lines are the best-fitting prolate model (see text).

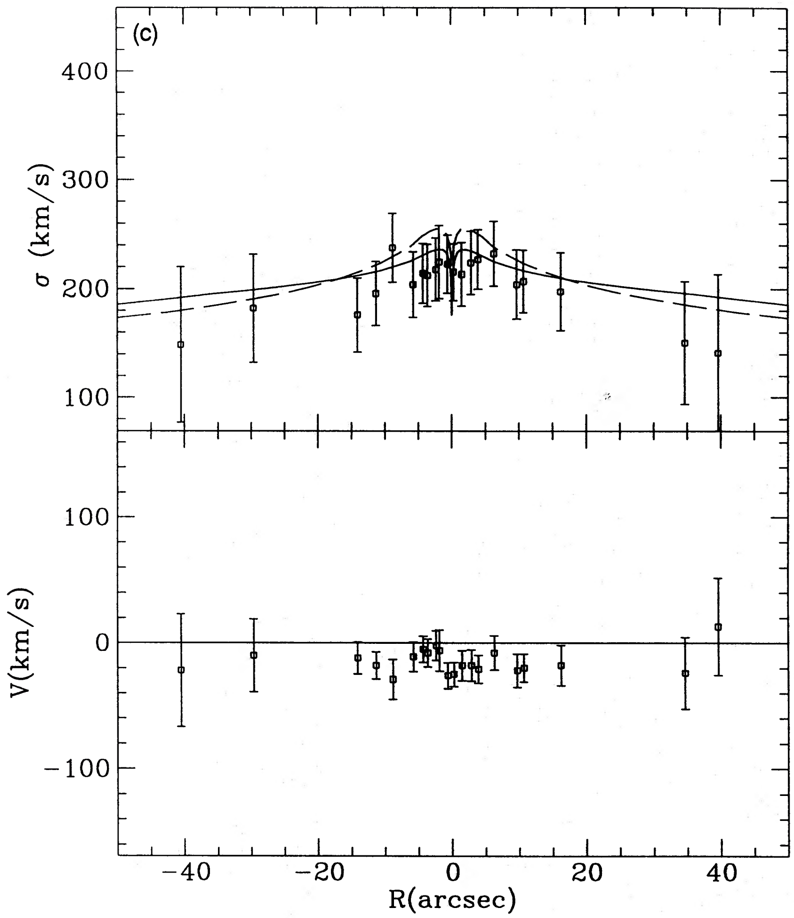

Figure 20 – *continued*

behaviour that is not dependent on the details of the orbital structure, it is interesting to note that NGC 3706, which is a rotation-supported galaxy, seems to follow the slope of the nuclei. We still need to understand the influence on this diagram of galaxies that have suffered from central Mg_2 enhancement, and whether any systematic effect (e.g. a difference in the star formation time-scales between rotation-supported and anisotropic galaxies, driven, for instance, by differences in the stellar/gaseous ratio of the merging subunits) is present. Further and more accurate investigations are required.

5.7 Dark matter content and shapes of the haloes

For most of the galaxies in the sample, the dynamical modelling has given strong evidence for the presence of a massive, extended dark halo around the luminous galaxy. The values of the luminous M/L_B are in the range 4–29. (The very high M/L value derived, for example, for NGC 6407 might reflect the inadequacy of constant-ellipticity models in representing galaxies with rapidly varying ellipticity.) The best-fitting haloes show a variety of intrinsic shapes, and, most interestingly, flattened haloes seem to be required in many cases (the only exception in the sample studied here being NGC 2434, which has been well fitted with a spherical halo). In the other cases, even haloes more flattened than the luminous galaxy itself are preferred, in order properly to fit the observed kinematic profiles (see also the fit to NGC 5018 presented in Paper I). Even if less than conclusive (as a third integral of motion might be required to represent the galactic dynamical fields properly), this result is intriguing, because in standard CDM cosmological models such very flattened dark haloes are naturally produced by dissipationless collapse of dark matter with very cold initial conditions (so that radial orbit instability can occur during the collapse; Dubinski & Carlberg 1991. See also Bertin & Stiavelli 1993 and references therein).

6 CONCLUSIONS

In this paper we have studied, through optical multiband CCD photometry and multiposition CCD long-slit spectroscopy, five early-type galaxies, namely NGC 439, NGC 2434, NGC 3706, NGC 6407 and NGC 7192. In two of the galaxies, NGC 2434 and NGC 7192, the innermost nuclear regions counter-rotate with respect to the main galactic bulk and show, corresponding with the kinematically decoupled core, an enhancement in the Mg_2 index. Such behaviour had been detected before in a few other galaxies (Bender & Surma 1992; DSP); it can be explained if the core has

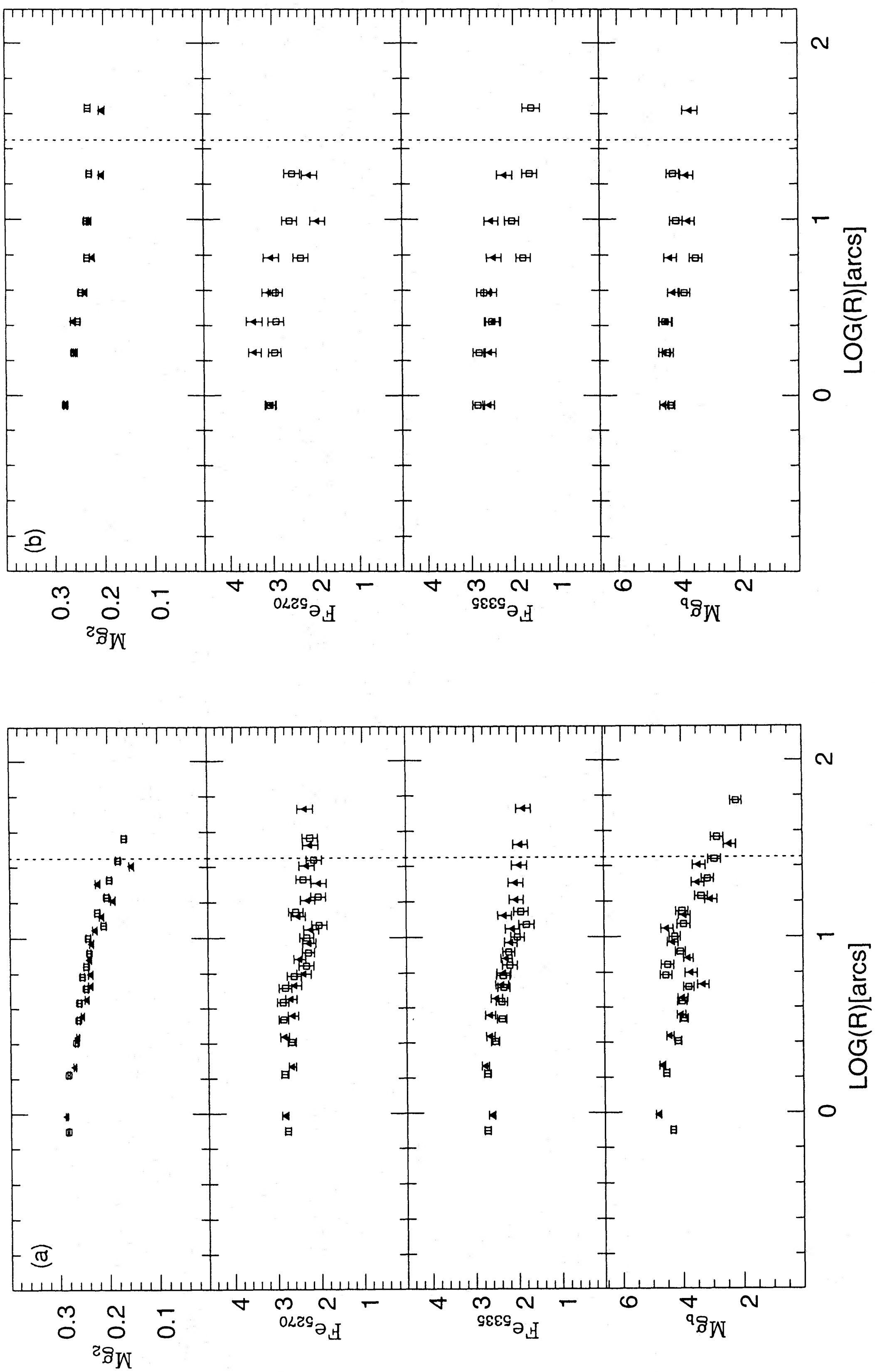

Figure 21. (a) and (b) As Fig. 4, for NGC 7192. (c) PA = 65°.

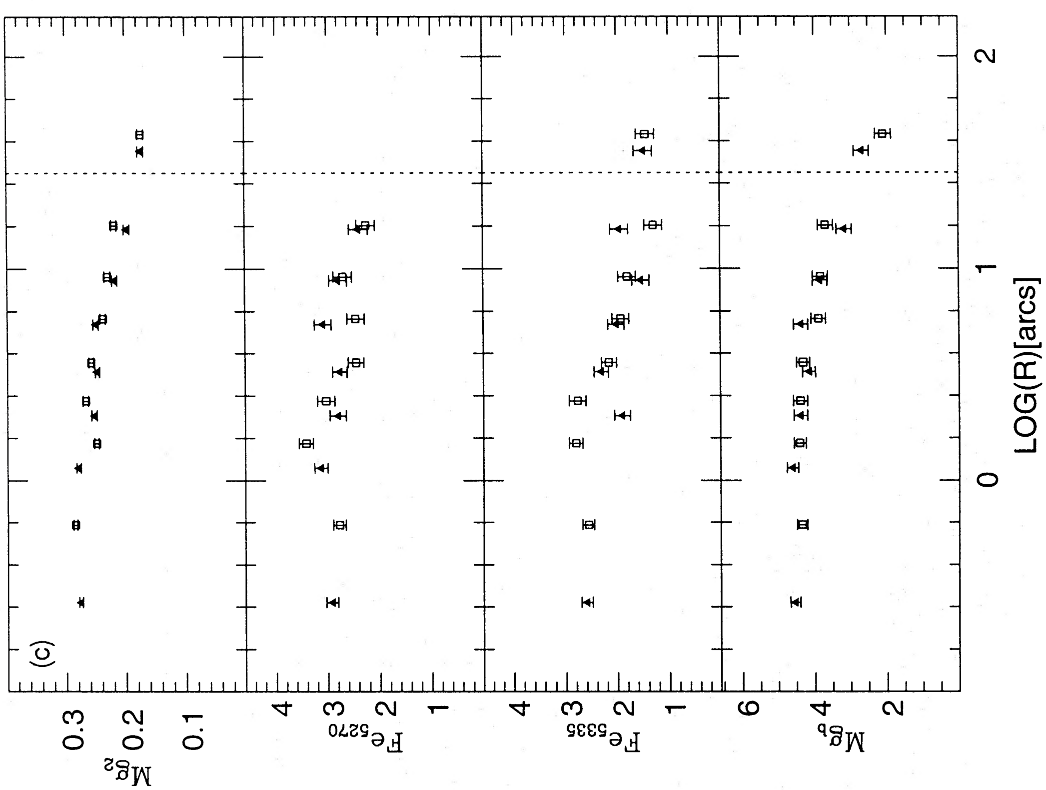

Figure 21 – *continued*

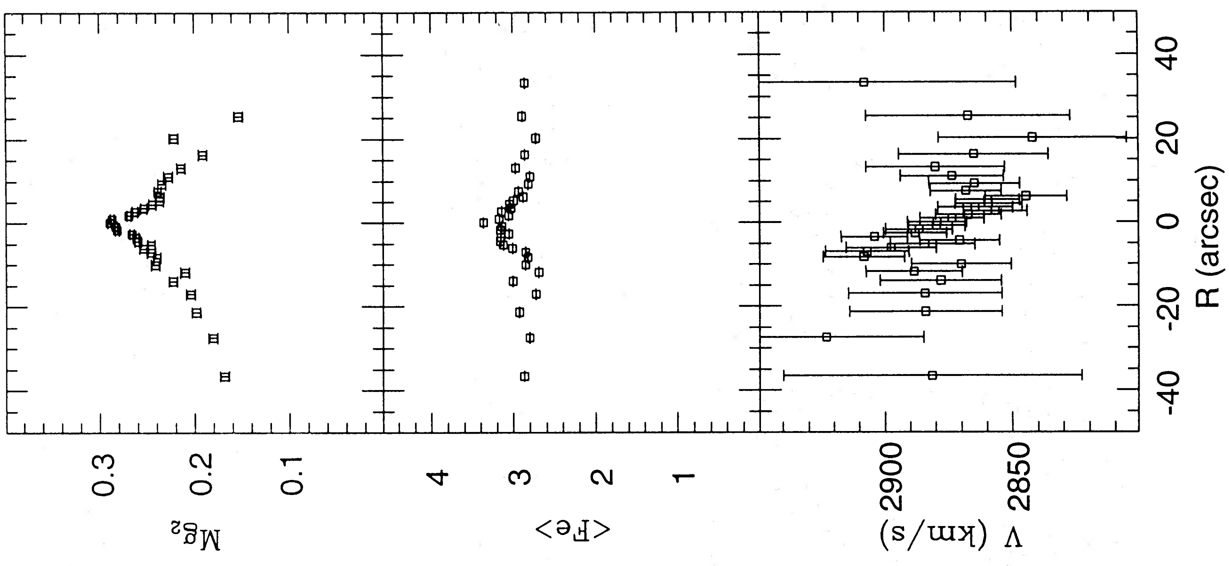

Figure 22. As Fig. 9, for NGC 7192.

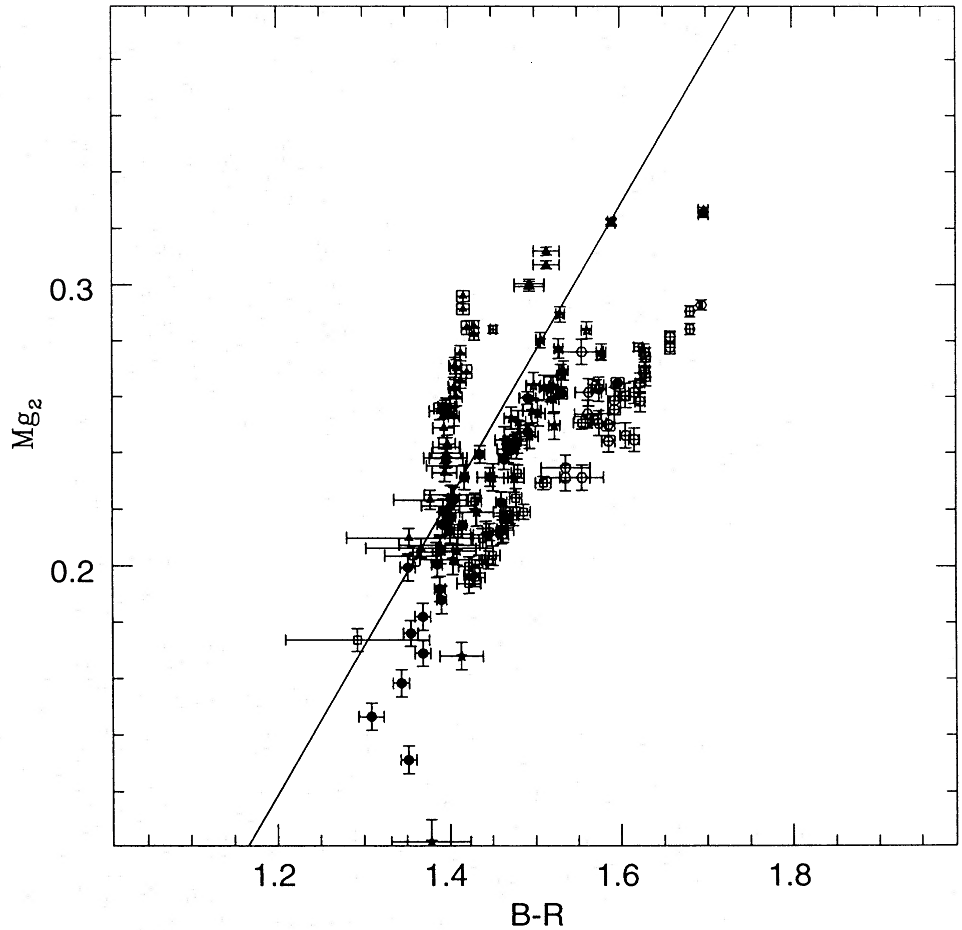

Figure 23. Mg_2 versus $(B-R)$ within the galaxies of the sample. The solid line is the fit to the nuclei (from DSP). Stars: NGC 439; open squares: NGC 2434; filled triangles: NGC 3706; open hexagons: NGC 6407, and filled circles: NGC 7192.

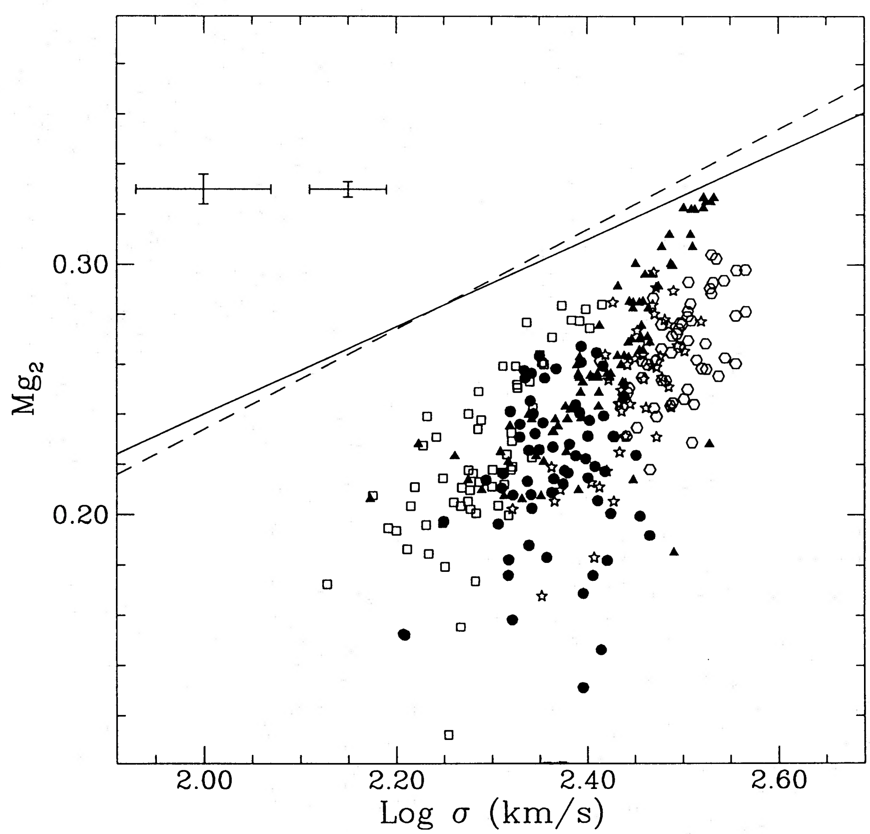

Figure 24. Mg_2 versus $\log_{10}\sigma$ within the galaxies of the sample. Symbols as in Fig. 23. The two lines are the fits to the nuclei given by BBF2. The two error bars are those typical for the inner (small bar) and outer (large bar) regions.

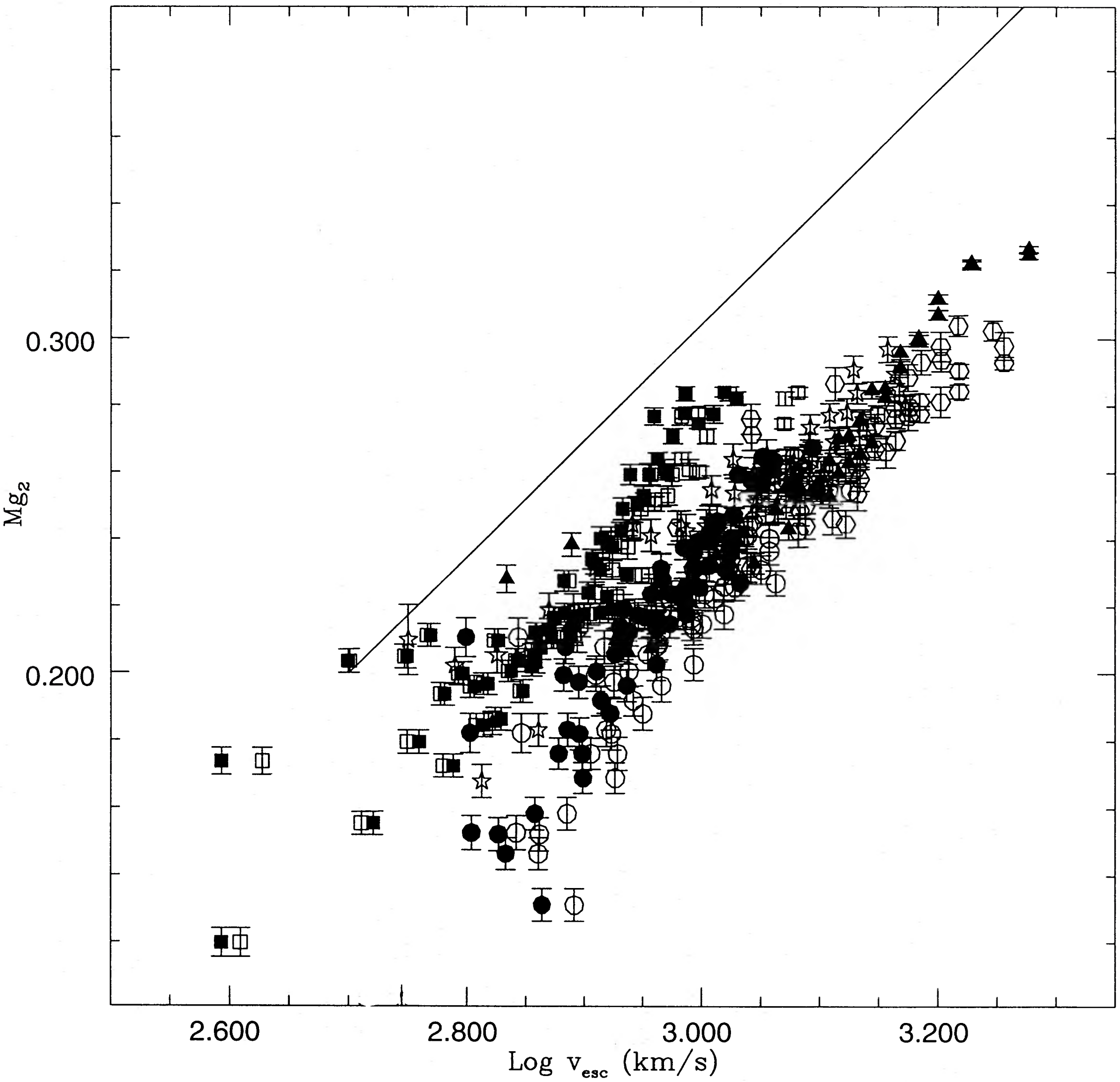

Figure 25. Mg_2 versus the escape velocity (derived from the dynamical modelling) within the galaxies of the sample. Symbols as in Fig. 23 (open and filled squares and circles discriminate oblate and prolate models for NGC 2434 and NGC 7192, respectively). The solid line is the fit to the DSP sample.

suffered from an additional star formation episode due to infalling gas which has enhanced the magnesium content of the central region and generated a stellar disc observed to be counter-rotating in the velocity profile. For both galaxies, we have also measured the ⟨Fe⟩ profile, which is also found to show an enhancement relative to the galactic bulk. Such an enhancement is, however, much less pronounced than that detected in Mg_2. This and the red central colour, ensuring the absence of any younger stellar component, suggest that the additional star formation event has occurred at earlier phases and has been very rapid, i.e. on time-scales shorter than that occurring during the formation of the bulk of the galaxy, and also shorter than that typical of (iron-producing) Type I supernovae. If this phenomenon were a common feature in giant ellipticals, it might be at least partly responsible for the shallow slope in the ⟨Fe⟩–Mg_2 plane shown by galactic nuclei, as compared with that traced *within* galaxies, where the outer regions (not affected by any Mg_2 enhancement) dominate the measurement.

Axisymmetric dynamical models have been constructed for each galaxy, and in some objects they support the presence of a significantly massive and extended dark halo (in some cases at least as flattened as the luminous galaxy it surrounds). The availability of observations at several position angles for flattened galaxies has turned out to be a necessary ingredient to constrain the shapes of the haloes. In round galaxies, the degeneracy (in projection) increases enormously the freedom in modelling. The escape velocity from the gravitational potential well has been derived from the best-fitting dynamical model of each galaxy.

A *local* dependence of the metallicity (as traced by Mg_2) on the escape velocity has been found (supporting the results of FI and DSP); however, the spread in the *local* relationship hints at other physical parameters, in addition to the local

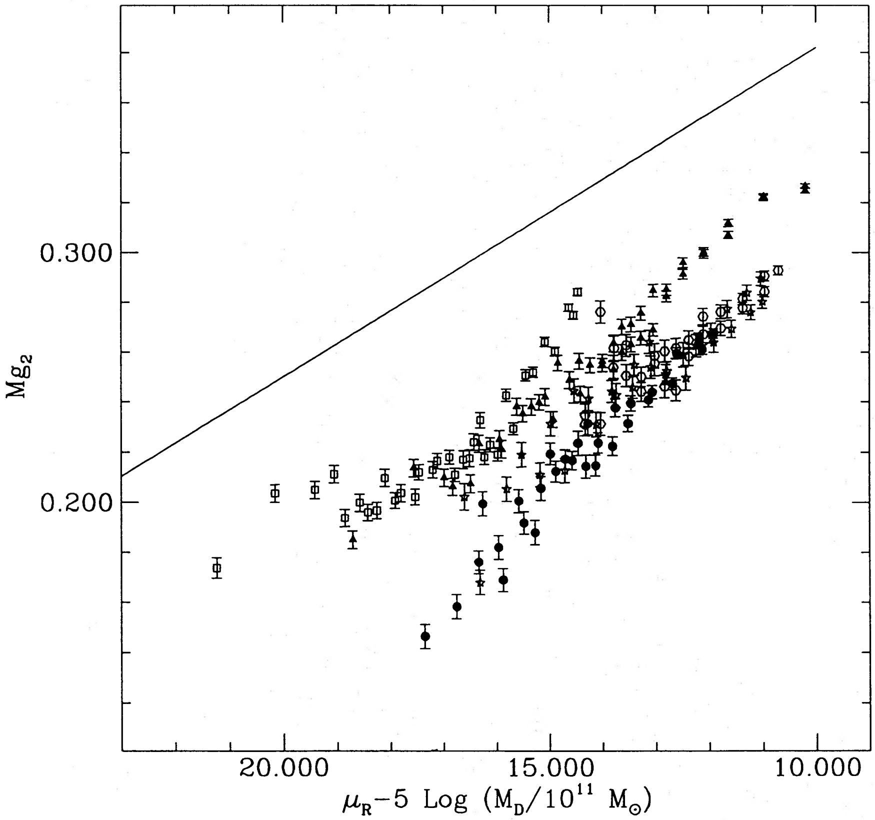

Figure 26. Mg_2 versus $\mu_R - 5\ \log_{10} M$ (i.e. versus $M^2\rho$; mass derived from the dynamical modelling) within the galaxies of the sample. Symbols as in Fig. 23. The solid line is the fit to the nuclei given by BBF2.

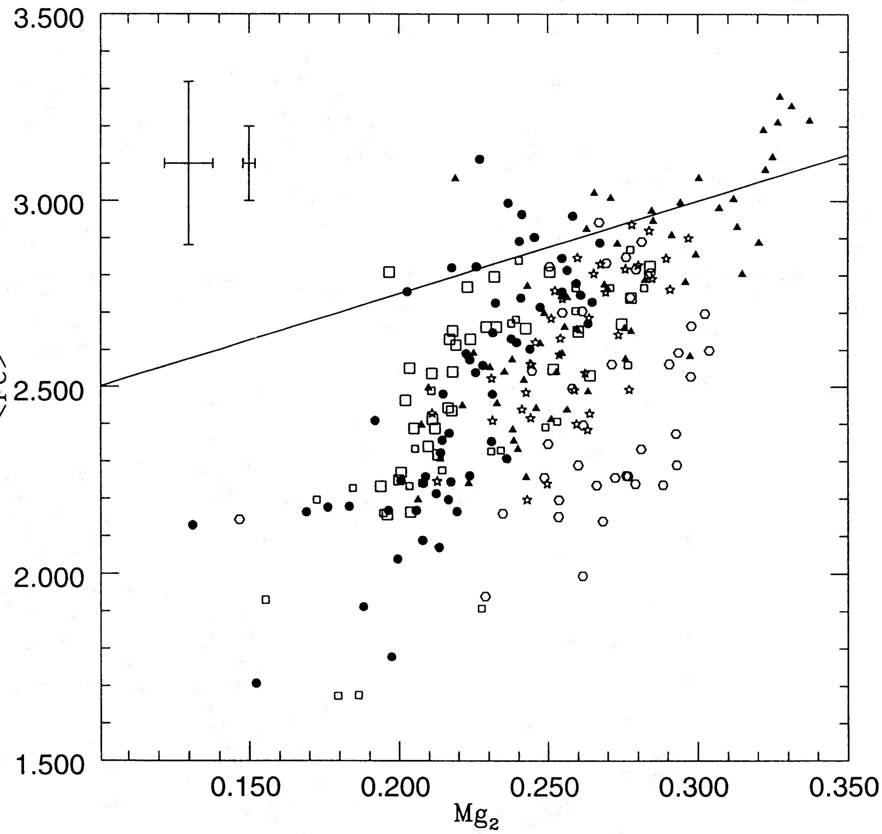

Figure 27. ⟨Fe⟩ versus Mg_2 within the galaxies of the sample. Symbols as in Fig. 23. The solid line is the fit to the nuclei given by Burstein et al. (1984). The two error bars are those typical for the inner (small bar) and outer (large bar) regions.

potential affecting the metallicity distribution within galaxies. The *local* dependence of the Mg_2 index on the *local* stellar density, as described by the *R* surface brightness, has been investigated. The mass derived from the dynamical modelling has been used to scale the density; the addition of the dark component has turned out to be crucial in reducing the spread in the Mg_2–$M^2\rho$ relationship, which seems to follow the *average* relationship derived by BBF2 for galactic nuclei. It is remarkable that objects with kinematically decoupled cores and flattened by anisotropic pressure (such as NGC 2434), and rotation-supported objects such as NGC 3706, lie almost parallel and very close in the Mg_2–$M^2\rho$ plane. It seems as if *local* phenomena, regulated by basic physical processes, such as the amount of dissipation that occurred or the star formation rate, are able to reproduce (once scaled to the size of the galaxy itself) the observed metallicity distribution. However, the relatively large scatter in the relationship might suggest a residual dependence on, for example, the details of the orbital structure or the galactic size.

ACKNOWLEDGMENTS

We are indebted to R. van der Marel for kindly providing the Fourier fitting program. We also thank R. F. Peletier, M. Stiavelli and P. T. de Zeeuw for interesting comments on a preliminary version of this paper. CMC wishes to thank F. Matteucci and M. Stiavelli for enlightening conversations. This research has made use of the NASA/IPAC extragalactic database (NED), which is operated by the Jet Propulsion Laboratory, Caltech, under contract with the National Aeronautics and Space Administration.

REFERENCES

Bender R., 1988, A&A, 202, L5
Bender R., Surma P., 1992, A&A, 258, 250
Bender R., Burstein D., Faber S. M., 1992, ApJ, 399, 462 (BBF1)
Bender R., Burstein D., Faber S. M., 1993, ApJ, 411, 153 (BBF2)
Bertin G., Stiavelli M., 1993, Rep. Prog. Phys., 56, 493
Binney J. J., Davies R. L., Illingworth G. D., 1990, ApJ, 361, 78
Bregman J. N., Hogg D. E., Roberts M. S., 1992, ApJ, 387, 484
Burstein D., Heiles C., 1984, ApJS, 54, 33
Burstein D., Faber S. M., Gaskell C. M., Krumm N., 1984, ApJ, 287, 586
Burstein D., Bertola F., Buson L. M., Faber S. M., Lauer T. R., 1988, ApJ, 328, 440
Carollo C. M., 1993, PhD thesis, Ludwig-Maximilians Universität (C93)
Carollo C. M., Danziger I. J., 1994, MNRAS, in press (Paper I)
Carollo C. M., Danziger I. J., Buson L. M., 1993, MNRAS, 265, 553 (CDB)
Carollo C. M., van der Marel R., de Zeeuw P. T., Danziger I. J., 1994, MNRAS, submitted (CMZD)
Davies R. L., Burstein D., Dressler A., Faber S. M., Lynden-Bell D., Terlevich R., Wegner G., 1987, ApJS, 64, 581 (D87)
Davies R. L., Sadler E. M., Peletier R. F., 1993, MNRAS, 262, 650
de Vaucouleurs A., Longo G., 1988, Catalogue of Visual and Infrared Photometry of Galaxies from 0.5 μm to 10 μm (1961–1985). Univ. Texas, Austin
de Vaucouleurs G., de Vaucouleurs A., Corwin H. G. Jr, Buta R. J., Paturel G., Fouqué P., 1991, Third Reference Catalogue of Bright Galaxies. Springer-Verlag, New York (RC3)
Dubinski J., Carlberg R. G., 1991, ApJ, 378, 496
Franx M., Illingworth G. D., 1988, ApJ,. 327, L55
Franx M., Illingworth G. D., 1990, ApJ, 359, L41 (FI)
Franx M., Illingworth G. D., Heckman T., 1989, AJ, 98, 538
Gonzales J. J., 1993, PhD thesis, Univ. California, Santa Cruz
Gourgoulhon E., Chamaraux P., Fouqué P., 1992, A&A, 255, 69
Huchra J. P., Geller M. J., 1982, ApJ, 257, 423
Jaffe W., 1983, MNRAS, 202, 995
Jedrezejewski R. J., Schechter P. L., 1988, ApJ, 330, L87
Lauberts A., Valentjin E. A., 1989, The surface photometry catalogue of the ESO–Uppsala Galaxies. ESO, Garching
Longo G., de Vaucouleurs A., 1983, A General Catalogue of Photoelectric Magnitudes and Colors in the U, B, V, System 91936-1982. Univ. Texas, Austin
Maia M. A. G., Da Costa L. N., Latham D. W., 1989, ApJS, 69, 809
Malin D. F., Carter D., 1983, ApJ, 274, 534
Matteucci F., 1994, A&A, in press
Nieto J.-L., Bender R., Arnaud J., Surma P., 1991, A&A, 244, L25
Peletier R. F., Davies R. L., Illingworth G. D., Davis L. E., Cawson M. C. M., 1990, AJ, 100, 1091
Phillips M. M., Jenkins C. R., Dopita M. A., Sadler E. M., Binette L., 1986, AJ, 91, 1062
Roberts M. S., Hogg D. E., Bregman J. N., Forman W. R., Jones C., 1991, ApJS, 75, 751
Sadler E. M., Jenkins C. R., Kotanyi C. G., 1989, MNRAS, 240, 591
Sargent W. L. W., Schechter P. L., Bocksenberg A., Shortridge K., 1977, ApJ, 212, 326
Statler T. S., 1991, ApJ, 382, L11
Terlevich R., Davies R. L., Faber S. M., Burstein D., 1981, MNRAS, 196, 381
Vader J. P., Chaboyer B., 1992, Publ. Astron. Soc. Pac., 104, 57
van der Marel R., Franx M., 1993, ApJ, 407, 525
Whitford B. C., 1971, ApJ, 169, 215
Wilkinson A., Browne I. W. A., Kotanyi C., Christiansen W. A., Williams R., Sparks W. B., 1987, MNRAS, 224, 895
Worthey G., Faber S. M., Gonzalez J. J., 1992, ApJ, 398, 69

APPENDIX A: PHOTOMETRIC DATA

NGC 439

rad	R	e_R	ell	e_ell	c4	e_c4	B-R	e_B-R
0.8800	17.4900	0.0035	0.0599	0.0005	-0.0110	0.0005	1.5760	0.0052
0.9680	17.5100	0.0036	0.0619	0.0005	-0.0100	0.0005	1.5840	0.0052
1.0650	17.5500	0.0037	0.0656	0.0005	-0.0090	0.0005	1.5780	0.0054
1.1700	17.5900	0.0039	0.0699	0.0005	-0.0080	0.0005	1.5750	0.0056
1.2850	17.6300	0.0040	0.0755	0.0005	-0.0070	0.0005	1.5770	0.0058
1.4170	17.6900	0.0043	0.0830	0.0005	-0.0050	0.0005	1.5600	0.0060
1.5580	17.7300	0.0043	0.0915	0.0005	-0.0010	0.0005	1.5670	0.0059
1.7160	17.8000	0.0043	0.0995	0.0005	0.0000	0.0005	1.5550	0.0058
1.8830	17.8800	0.0041	0.1087	0.0005	0.0000	0.0005	1.5450	0.0056
2.0770	17.9600	0.0038	0.1199	0.0005	-0.0020	0.0005	1.5360	0.0054
2.2790	18.0500	0.0036	0.1367	0.0005	-0.0020	0.0005	1.5280	0.0051
2.5080	18.1100	0.0033	0.1553	0.0005	-0.0020	0.0005	1.5490	0.0048
2.7630	18.2100	0.0032	0.1712	0.0005	-0.0010	0.0005	1.5380	0.0049
3.0360	18.3200	0.0031	0.1877	0.0005	0.0000	0.0005	1.5220	0.0052
3.3440	18.4000	0.0031	0.2056	0.0005	-0.0010	0.0005	1.5420	0.0053
3.6780	18.5300	0.0032	0.2225	0.0005	-0.0030	0.0005	1.5120	0.0053
4.0390	18.6300	0.0030	0.2337	0.0005	-0.0040	0.0005	1.5190	0.0052
4.4440	18.7400	0.0031	0.2472	0.0005	-0.0050	0.0005	1.5230	0.0060
4.8930	18.8600	0.0035	0.2629	0.0005	-0.0060	0.0005	1.5220	0.0067
5.3860	19.0000	0.0038	0.2774	0.0005	-0.0050	0.0005	1.5050	0.0068
5.9220	19.1500	0.0047	0.2936	0.0005	-0.0060	0.0005	1.4700	0.0079
6.5120	19.2400	0.0045	0.3010	0.0005	-0.0100	0.0010	1.5080	0.0097
7.1630	19.3300	0.0043	0.3090	0.0005	-0.0070	0.0020	1.5390	0.0093
7.8760	19.4900	0.0046	0.3240	0.0005	-0.0060	0.0005	1.5020	0.0084
8.6680	19.6100	0.0044	0.3356	0.0005	-0.0080	0.0005	1.5020	0.0088
9.5300	19.7400	0.0046	0.3453	0.0005	-0.0090	0.0010	1.5020	0.0107
10.4900	19.8700	0.0052	0.3460	0.0005	-0.0090	0.0005	1.4900	0.0098
11.5400	20.0100	0.0059	0.3491	0.0005	-0.0080	0.0010	1.4860	0.0114
12.6900	20.1500	0.0056	0.3340	0.0005	-0.0100	0.0010	1.4790	0.0120
13.9600	20.3100	0.0049	0.3260	0.0005	-0.0070	0.0010	1.4830	0.0103
15.3600	20.4700	0.0047	0.3227	0.0005	-0.0040	0.0010	1.4780	0.0115
16.8900	20.6300	0.0051	0.3243	0.0005	-0.0060	0.0010	1.4690	0.0120
18.5800	20.7900	0.0049	0.3220	0.0005	-0.0010	0.0020	1.4710	0.0127
20.4400	20.9600	0.0049	0.3373	0.0005	0.0000	0.0010	1.4630	0.0110
22.4800	21.1000	0.0060	0.3630	0.0005	0.0070	0.0010	1.4610	0.0148
24.7300	21.2600	0.0080	0.3958	0.0005	0.0020	0.0020	1.4640	0.0194
27.2000	21.4100	0.0074	0.3928	0.0005	0.0030	0.0010	1.4460	0.0167
29.9200	21.5600	0.0066	0.3825	0.0005	0.0000	0.0010	1.4430	0.0146
32.9100	21.7300	0.0074	0.3824	0.0005	-0.0030	0.0020	1.4330	0.0179
36.2000	21.9000	0.0071	0.3756	0.0005	0.0020	0.0010	1.4340	0.0200
39.8300	22.0700	0.0066	0.3683	0.0005	0.0070	0.0010	1.4080	0.0189
43.8200	22.2400	0.0082	0.3912	0.0005	0.0100	0.0010	1.4110	0.0241
48.1900	22.4200	0.0106	0.4050	0.0005	0.0110	0.0020	1.4030	0.0283
53.0100	22.6100	0.0096	0.3995	0.0005	0.0100	0.0020	1.4060	0.0279
58.3100	22.7800	0.0084	0.3987	0.0005	0.0090	0.0010	1.4180	0.0246
64.1400	22.9600	0.0126	0.4253	0.0005	0.0110	0.0020	1.4050	0.0363
70.5600	23.1500	0.0119	0.4086	0.0005	0.0110	0.0020	1.4090	0.0378
77.6200	23.3400	0.0113	0.3865	0.0005	0.0100	0.0020	1.4020	0.0366
85.3800	23.5500	0.0137	0.3966	0.0005	0.0090	0.0020	1.3750	0.0441
93.9100	23.7500	0.0160	0.3964	0.0005	0.0130	0.0020	1.4130	0.0543
103.3000	23.9700	0.0136	0.3637	0.0005	0.0050	0.0030	1.3940	0.0590
113.6000	24.1800	0.0213	0.4068	0.0005	0.0100	0.0040	1.4270	0.0763
125.0000	24.3600	0.0243	0.4068	0.0005	0.0200	0.0060	1.3860	0.0919
137.5000	24.5500	0.0256	0.3425	0.0005	0.0120	0.0070	1.4270	0.1056
151.2000	24.7100	0.0269	0.3425	0.0005	0.0240	0.0290	1.4080	0.1143
166.4000	24.8600	0.0353	0.3425	0.0005	0.0050	0.0020	1.5010	0.1520

NGC 2434

rad	R	e_R	ell	e_ell	c4	e_c4	B-R	e_B-R
0.6640	15.9300	0.0012	0.0090	0.0005	0.0010	0.0005	1.6010	0.0046
0.7304	15.9600	0.0013	0.0099	0.0005	0.0010	0.0005	1.6140	0.0048
0.8034	16.0100	0.0014	0.0188	0.0005	-0.0030	0.0005	1.6020	0.0052
0.8831	16.0600	0.0017	0.0294	0.0005	-0.0040	0.0005	1.5930	0.0056
0.9694	16.1200	0.0021	0.0380	0.0005	-0.0050	0.0005	1.5880	0.0062
1.0690	16.1800	0.0025	0.0400	0.0005	-0.0060	0.0005	1.5870	0.0070
1.1750	16.2500	0.0028	0.0339	0.0005	-0.0050	0.0005	1.5890	0.0078
1.2950	16.3500	0.0032	0.0269	0.0005	-0.0050	0.0005	1.5500	0.0085
1.4210	16.4200	0.0033	0.0247	0.0005	-0.0050	0.0005	1.5520	0.0088
1.5670	16.5000	0.0035	0.0341	0.0005	-0.0060	0.0005	1.5530	0.0091
1.7200	16.5900	0.0035	0.0469	0.0005	-0.0060	0.0005	1.5530	0.0094
1.8920	16.6900	0.0036	0.0550	0.0005	-0.0050	0.0005	1.5490	0.0094
2.0850	16.7900	0.0036	0.0600	0.0005	-0.0040	0.0005	1.5390	0.0097
2.2910	16.9000	0.0035	0.0624	0.0005	-0.0020	0.0005	1.5200	0.0095
2.5230	17.0300	0.0034	0.0664	0.0005	-0.0010	0.0005	1.4910	0.0088
2.7760	17.1800	0.0032	0.0711	0.0005	-0.0020	0.0005	1.4510	0.0085
3.0480	17.2600	0.0027	0.0750	0.0005	-0.0020	0.0005	1.4970	0.0081
3.3530	17.4400	0.0026	0.0790	0.0005	-0.0020	0.0005	1.4190	0.0079
3.6920	17.5400	0.0024	0.0831	0.0005	0.0000	0.0005	1.4380	0.0078
4.0640	17.6500	0.0020	0.0858	0.0005	0.0000	0.0005	1.4610	0.0075
4.4690	17.7800	0.0019	0.0909	0.0005	-0.0020	0.0005	1.4600	0.0070
4.9140	17.9100	0.0017	0.0931	0.0005	-0.0030	0.0005	1.4530	0.0067
5.4050	18.0500	0.0019	0.0965	0.0005	-0.0030	0.0010	1.4440	0.0068
5.9430	18.1800	0.0020	0.0960	0.0005	-0.0020	0.0005	1.4460	0.0063
6.5400	18.3400	0.0017	0.0903	0.0005	-0.0020	0.0005	1.4480	0.0065
7.1910	18.5000	0.0016	0.0879	0.0005	0.0000	0.0005	1.4470	0.0061
7.9150	18.6600	0.0018	0.0867	0.0005	0.0000	0.0005	1.4370	0.0068

NGC 2434

rad	R	e_R	ell	e_ell	c4	e_c4	B-R	e_B-R
8.7050	18.8200	0.0025	0.0786	0.0005	0.0010	0.0010	1.4280	0.0079
9.5750	18.9800	0.0022	0.0791	0.0005	0.0030	0.0010	1.4300	0.0077
10.5300	19.1400	0.0024	0.0791	0.0005	0.0020	0.0010	1.4350	0.0085
11.5900	19.2900	0.0024	0.0874	0.0005	0.0030	0.0020	1.4140	0.0088
12.7400	19.4300	0.0029	0.0924	0.0005	0.0020	0.0020	1.4210	0.0111
14.0200	19.5700	0.0027	0.0966	0.0005	0.0030	0.0020	1.4110	0.0096
15.4200	19.7100	0.0032	0.0895	0.0005	0.0030	0.0010	1.4100	0.0111
16.9700	19.8500	0.0033	0.0912	0.0005	0.0000	0.0020	1.4100	0.0117
18.6600	20.0100	0.0033	0.0868	0.0005	0.0020	0.0010	1.4020	0.0124
20.5200	20.1800	0.0031	0.0808	0.0005	0.0030	0.0010	1.4050	0.0136
22.5800	20.3600	0.0032	0.0835	0.0005	0.0000	0.0010	1.3960	0.0150
24.8300	20.5500	0.0037	0.0873	0.0005	0.0000	0.0010	1.3750	0.0159
27.3200	20.7500	0.0044	0.0848	0.0005	0.0000	0.0010	1.3660	0.0193
30.0500	20.9600	0.0049	0.0860	0.0005	0.0020	0.0010	1.3670	0.0217
33.0600	21.1500	0.0055	0.0873	0.0005	0.0030	0.0010	1.3590	0.0254
36.3600	21.3400	0.0063	0.0937	0.0005	0.0030	0.0020	1.3500	0.0279
40.0000	21.5000	0.0068	0.1155	0.0005	0.0030	0.0010	1.3400	0.0325
44.0000	21.6800	0.0082	0.1259	0.0005	0.0010	0.0010	1.3240	0.0380
48.4000	21.8600	0.0098	0.1189	0.0005	0.0020	0.0020	1.3090	0.0423
53.2400	22.0500	0.0118	0.1265	0.0005	0.0050	0.0020	1.3480	0.0538
58.5600	22.2600	0.0127	0.1213	0.0005	0.0060	0.0020	1.2880	0.0608
64.4200	22.5000	0.0151	0.1156	0.0005	0.0000	0.0020	1.2760	0.0765
70.8600	22.7400	0.0190	0.0940	0.0005	-0.0020	0.0030	1.2570	0.0943
77.9500	23.0100	0.0231	0.1063	0.0005	0.0010	0.0020	1.1920	0.1124
85.7400	23.2700	0.0292	0.1183	0.0005	-0.0020	0.0040	1.1900	0.1438
94.3100	23.5400	0.0355	0.0915	0.0005	0.0000	0.0040	1.0780	0.1664
103.8000	23.8100	0.0461	0.0726	0.0005	0.0070	0.0050	1.0050	0.2046
114.1000	24.0500	0.0584	0.0781	0.0005	0.0190	0.0060	0.9258	0.2417
125.5000	24.4000	0.0850	0.1087	0.0005	0.0130	0.0050	0.8293	0.2794
138.1000	24.6800	0.1229	0.1087	0.0005	0.4490	0.2330	0.7232	0.3208
151.9000	25.0400	0.1960	0.0337	0.0005	-0.0070	0.0020	0.6065	0.3664

NGC 6407

rad	R	e_R	ell	e_ell	c4	e_c4	B-R	e_B-R
0.8800	17.2400	0.0012	0.0150	0.0005	-0.0090	0.0005	1.6810	0.0040
0.9680	17.2700	0.0013	0.0153	0.0005	-0.0070	0.0005	1.6800	0.0042
1.0650	17.3100	0.0014	0.0151	0.0005	-0.0070	0.0005	1.6840	0.0042
1.1700	17.3400	0.0015	0.0154	0.0005	-0.0060	0.0005	1.6940	0.0044
1.2850	17.4200	0.0016	0.0169	0.0005	-0.0050	0.0005	1.6700	0.0047
1.4170	17.4600	0.0017	0.0202	0.0005	-0.0030	0.0005	1.6890	0.0051
1.5580	17.5400	0.0018	0.0231	0.0005	0.0000	0.0005	1.6710	0.0054
1.7160	17.6300	0.0019	0.0261	0.0005	0.0030	0.0005	1.6520	0.0058
1.8830	17.6800	0.0018	0.0290	0.0005	0.0040	0.0005	1.6820	0.0056
2.0770	17.7800	0.0019	0.0323	0.0005	0.0030	0.0005	1.6640	0.0058
2.2790	17.9000	0.0020	0.0374	0.0005	0.0030	0.0005	1.6410	0.0058
2.5080	18.0200	0.0022	0.0419	0.0005	0.0050	0.0005	1.6100	0.0062
2.7630	18.0900	0.0021	0.0468	0.0005	0.0050	0.0005	1.6420	0.0062
3.0360	18.2500	0.0021	0.0527	0.0005	0.0050	0.0005	1.5920	0.0059
3.3440	18.3400	0.0018	0.0589	0.0005	0.0040	0.0005	1.6150	0.0054
3.6780	18.4300	0.0018	0.0665	0.0005	0.0020	0.0005	1.6340	0.0053
4.0390	18.5500	0.0019	0.0738	0.0005	0.0010	0.0005	1.6270	0.0053
4.4440	18.6700	0.0020	0.0808	0.0005	0.0000	0.0005	1.6230	0.0054
4.8930	18.8000	0.0023	0.0935	0.0005	0.0000	0.0005	1.6210	0.0057
5.3860	18.9200	0.0026	0.1035	0.0005	0.0000	0.0010	1.6150	0.0061
5.9220	19.0500	0.0024	0.1071	0.0005	0.0000	0.0010	1.6090	0.0060
6.5120	19.1800	0.0024	0.1075	0.0005	0.0010	0.0010	1.6000	0.0060
7.1630	19.3200	0.0029	0.1140	0.0005	0.0010	0.0020	1.5920	0.0076
7.8760	19.4600	0.0028	0.1196	0.0005	0.0000	0.0020	1.5880	0.0078
8.6680	19.6000	0.0027	0.1180	0.0005	0.0000	0.0020	1.5840	0.0073
9.5300	19.7400	0.0027	0.1133	0.0005	-0.0050	0.0010	1.5800	0.0076
10.4900	19.8800	0.0038	0.0982	0.0005	-0.0050	0.0020	1.5720	0.0094
11.5400	20.0200	0.0063	0.0961	0.0005	-0.0100	0.0030	1.5650	0.0135
12.6900	20.1600	0.0103	0.1103	0.0005	-0.0360	0.0040	1.5570	0.0200
13.9600	20.3000	0.0137	0.1214	0.0005	-0.0380	0.0050	1.5550	0.0254
15.3600	20.4300	0.0172	0.1214	0.0005	-0.0300	0.0060	1.5490	0.0292
16.8900	20.5800	0.0165	0.1091	0.0005	-0.0220	0.0050	1.5380	0.0289
18.5800	20.7400	0.0137	0.1186	0.0005	-0.0350	0.0030	1.5140	0.0242
20.4400	20.9000	0.0097	0.1092	0.0005	-0.0250	0.0020	1.4840	0.0205
22.4800	21.0500	0.0081	0.1230	0.0005	-0.0090	0.0020	1.4710	0.0194
24.7300	21.2200	0.0073	0.1673	0.0005	0.0050	0.0030	1.4390	0.0176
27.2000	21.4000	0.0069	0.1599	0.0005	0.0070	0.0030	1.4050	0.0179
29.9200	21.5900	0.0061	0.1647	0.0005	0.0040	0.0020	1.3790	0.0193
32.9100	21.7500	0.0077	0.2024	0.0005	0.0130	0.0030	1.3470	0.0256
36.2000	21.9200	0.0113	0.2339	0.0005	0.0140	0.0030	1.3090	0.0328
39.8300	22.1000	0.0107	0.1956	0.0005	0.0110	0.0030	1.2650	0.0336
43.8200	22.3000	0.0112	0.1752	0.0005	0.0070	0.0030	1.2200	0.0367
48.1900	22.4900	0.0126	0.1655	0.0005	0.0000	0.0020	1.1790	0.0409
53.0100	22.7100	0.0168	0.1698	0.0005	-0.0090	0.0030	1.1420	0.0478
58.3100	22.9200	0.0199	0.1475	0.0005	-0.0210	0.0050	1.0970	0.0518
64.1400	23.0800	0.0243	0.1550	0.0005	-0.0240	0.0060	1.0830	0.0624
70.5600	23.2700	0.0336	0.1550	0.0005	-0.0600	0.0060	1.0840	0.0751
77.6200	23.4400	0.0422	0.1550	0.0005	-0.0690	0.0080	1.1110	0.0838
85.3800	23.5800	0.0531	0.2989	0.0005	0.0390	0.0110	1.1620	0.1007
93.9100	23.8200	0.0584	0.2451	0.0005	-0.0020	0.0060	1.1500	0.1174
103.3000	24.1100	0.0678	0.2919	0.0005	0.0240	0.0060	1.0590	0.1350
113.6000	24.4300	0.0818	0.2826	0.0005	0.0200	0.0070	1.0380	0.1671
125.0000	24.7400	0.0879	0.2811	0.0005	0.0240	0.0070	0.9124	0.1823
137.5000	25.1800	0.1182	0.2811	0.0005	0.0040	0.0080	0.7846	0.2473
151.2000	25.5900	0.1400	0.2811	0.0005	0.0130	0.0120	0.6599	0.3361
166.4000	26.0600	0.1857	0.2811	0.0005	-0.0150	0.0120	0.5228	0.4338
183.0000	26.6600	0.3107	0.2811	0.0005	-0.0380	0.0150	0.3719	0.5413

NGC 7192

rad	R	e_R	ell	e_ell	c4	e_c4	B-R	e_B-R
0.8800	16.6700	0.0032	0.0451	0.0005	-0.0080	0.0005	1.5740	0.0073
0.9680	16.7000	0.0032	0.0446	0.0005	-0.0070	0.0005	1.5970	0.0076
1.0650	16.7500	0.0033	0.0441	0.0005	-0.0070	0.0005	1.5470	0.0078
1.1700	16.8200	0.0035	0.0439	0.0005	-0.0080	0.0005	1.5340	0.0082
1.2850	16.8800	0.0036	0.0442	0.0005	-0.0090	0.0005	1.5400	0.0085
1.4170	16.9600	0.0038	0.0455	0.0005	-0.0060	0.0005	1.5250	0.0091
1.5580	17.0500	0.0039	0.0449	0.0005	-0.0010	0.0005	1.5080	0.0094
1.7160	17.1400	0.0038	0.0422	0.0005	0.0010	0.0005	1.4890	0.0094
1.8830	17.2200	0.0036	0.0373	0.0005	0.0000	0.0005	1.4920	0.0089
2.0770	17.3300	0.0033	0.0332	0.0005	-0.0020	0.0005	1.4680	0.0080
2.2790	17.4600	0.0030	0.0300	0.0005	-0.0050	0.0005	1.4380	0.0073
2.5080	17.5600	0.0029	0.0272	0.0005	-0.0040	0.0005	1.4730	0.0070
2.7630	17.6700	0.0028	0.0234	0.0005	-0.0030	0.0005	1.4710	0.0067
3.0360	17.8000	0.0027	0.0188	0.0005	0.0000	0.0005	1.4590	0.0063
3.3440	17.9500	0.0026	0.0162	0.0005	0.0000	0.0005	1.4350	0.0058
3.6780	18.0500	0.0025	0.0154	0.0005	0.0000	0.0005	1.4530	0.0054
4.0390	18.1800	0.0026	0.0155	0.0005	-0.0030	0.0005	1.4640	0.0054
4.4440	18.3100	0.0031	0.0207	0.0005	-0.0050	0.0005	1.4620	0.0061
4.8930	18.4700	0.0033	0.0271	0.0005	-0.0030	0.0005	1.4410	0.0063
5.3860	18.6500	0.0031	0.0286	0.0005	0.0000	0.0010	1.3910	0.0060
5.9220	18.7500	0.0023	0.0229	0.0005	0.0000	0.0010	1.4150	0.0044
6.5120	18.8800	0.0019	0.0222	0.0005	0.0000	0.0005	1.4090	0.0039
7.1630	19.0100	0.0020	0.0228	0.0005	0.0000	0.0005	1.4010	0.0040
7.8760	19.1400	0.0021	0.0199	0.0005	0.0000	0.0010	1.4000	0.0046
8.6680	19.2800	0.0021	0.0127	0.0005	0.0000	0.0005	1.4050	0.0049
9.5300	19.4200	0.0020	0.0196	0.0005	-0.0020	0.0005	1.3990	0.0050
10.4900	19.5700	0.0023	0.0101	0.0005	0.0010	0.0010	1.3890	0.0047
11.5400	19.7400	0.0025	0.0084	0.0005	-0.0010	0.0010	1.3910	0.0057
12.6900	19.9100	0.0026	0.0118	0.0005	-0.0010	0.0010	1.3890	0.0061
13.9600	20.1000	0.0027	0.0109	0.0005	0.0000	0.0010	1.3860	0.0065
15.3600	20.2900	0.0035	0.0111	0.0005	-0.0010	0.0020	1.3710	0.0078
16.8900	20.4600	0.0034	0.0085	0.0005	0.0010	0.0020	1.3690	0.0091
18.5800	20.6300	0.0034	0.0192	0.0005	0.0030	0.0020	1.3580	0.0081
20.4400	20.7900	0.0036	0.0204	0.0005	0.0000	0.0020	1.3520	0.0087
22.4800	20.9300	0.0037	0.0237	0.0005	0.0030	0.0020	1.3600	0.0084
24.7300	21.0900	0.0034	0.0227	0.0005	0.0000	0.0020	1.3550	0.0091
27.2000	21.2600	0.0034	0.0279	0.0005	-0.0030	0.0020	1.3450	0.0093
29.9200	21.4300	0.0040	0.0367	0.0005	0.0000	0.0020	1.3310	0.0117
32.9100	21.6200	0.0045	0.0238	0.0005	-0.0030	0.0020	1.3260	0.0121
36.2000	21.8500	0.0047	0.0390	0.0005	-0.0010	0.0020	1.3120	0.0144
39.8300	22.1100	0.0055	0.0316	0.0005	0.0020	0.0020	1.2740	0.0154
43.8200	22.3700	0.0067	0.0226	0.0005	0.0000	0.0020	1.2430	0.0186
48.1900	22.6100	0.0081	0.0244	0.0005	0.0030	0.0030	1.2210	0.0225
53.0100	22.8400	0.0104	0.0189	0.0005	0.0000	0.0030	1.2100	0.0283
58.3100	23.0600	0.0127	0.0133	0.0005	0.0100	0.0040	1.1650	0.0331
64.1400	23.2400	0.0144	0.0413	0.0005	0.0090	0.0060	1.1270	0.0385
70.5600	23.4300	0.0156	0.0226	0.0005	-0.0060	0.0040	1.1080	0.0413
77.6200	23.6200	0.0173	0.0220	0.0005	-0.0080	0.0040	1.0470	0.0462
85.3800	23.8300	0.0226	0.0370	0.0005	0.0040	0.0050	1.0100	0.0541
93.9100	24.0500	0.0290	0.0398	0.0005	-0.0090	0.0060	0.9697	0.0661
103.3000	24.2900	0.0426	0.0398	0.0005	-0.0120	0.0080	0.8799	0.0870
113.6000	24.5300	0.0469	0.0407	0.0005	0.0050	0.0060	0.8148	0.0983
125.0000	24.9200	0.0676	0.0134	0.0005	0.0010	0.0050	0.6235	0.1343
137.5000	25.2100	0.0923	0.0134	0.0005	0.0280	0.0120	0.5302	0.1698
151.2000	25.4500	0.1238	0.0134	0.0005	0.0300	0.0240	0.4747	0.2179
166.4000	25.5500	0.1421	0.0134	0.0005	0.0710	0.0400	0.4131	0.2749
183.0000	25.6800	0.1647	0.1085	0.0005	0.0010	0.0050	0.3454	0.3376
201.3000	25.7400	0.1813	0.1180	0.0005	0.0480	0.0130	0.2710	0.4065

APPENDIC B: KINEMATIC DATA

NGC 439 major

radius	V	e_V	Sigma	e_Sigma
-45.3	-110.0	32.4	209.0	48.0
-40.8	-64.0	55.8	237.2	47.4
-31.5	-41.0	29.8	242.2	42.2
-24.1	-14.0	30.5	282.1	38.9
-21.6	-12.0	23.3	284.5	33.9
-18.9	-23.0	29.0	289.9	37.2
-14.9	-4.0	19.8	263.1	32.9
-12.5	-18.0	14.8	270.1	27.9
-11.9	-26.0	16.2	259.9	29.8
-9.7	-17.0	20.0	281.6	31.6
-7.9	-23.0	15.8	274.5	28.4
-6.2	-20.0	19.3	307.7	29.5
-4.8	-6.0	17.0	297.2	28.3
-4.0	0.0	18.7	283.9	30.4
-3.2	4.0	18.0	314.0	28.1
-2.3	-1.0	19.5	332.7	28.4
-1.4	-14.0	14.8	295.7	26.5
-0.5	-3.0	17.2	310.9	27.7
0.4	-1.0	14.7	296.9	26.3
1.2	-15.0	16.0	307.1	27.0
3.0	6.0	15.1	288.7	27.1
3.9	8.0	18.2	301.2	29.0
4.3	-10.0	16.3	288.6	28.2
6.8	9.0	15.1	273.0	28.1

NGC 439 major

radius	V	e_V	Sigma	e_Sigma
7.8	5.0	18.2	266.1	31.2
9.6	11.0	20.1	297.7	30.6
11.1	17.0	16.1	296.8	27.4
14.8	15.0	24.8	317.2	33.0
18.5	19.0	21.4	312.7	30.8
23.9	27.0	28.6	295.8	36.7
31.3	53.0	38.2	338.6	39.3
36.2	31.0	33.2	276.3	41.1
42.7	21.0	45.8	213.6	56.3

NGC 439 minor

-70.8	4.0	53.9	192.7	79.8
-53.1	7.0	52.7	272.1	66.9
-33.3	-3.0	54.1	247.3	69.7
-15.0	-7.0	33.0	282.1	40.4
-9.1	-1.0	28.4	287.8	37.1
-5.7	16.0	24.9	316.9	33.1
-4.5	1.0	19.4	312.1	29.4
-3.5	-10.0	20.7	306.2	30.6
-2.3	1.0	17.2	273.3	29.9
-1.8	3.0	15.2	289.1	27.2
-1.4	7.0	19.4	304.5	29.7
-0.5	-9.0	21.6	296.5	31.8
-0.1	-4.0	17.2	282.9	29.3
0.4	0.0	19.3	268.7	32.1
1.2	12.0	17.3	298.1	28.5
1.6	3.0	16.4	290.0	28.2
2.1	-10.0	20.7	278.4	32.5
3.4	6.0	20.4	290.1	31.3
4.6	10.0	17.1	292.4	28.6
5.5	16.0	19.7	295.3	30.5
8.9	-1.0	27.9	305.4	35.6
15.4	-7.0	47.9	281.5	48.3
17.7	-8.0	39.8	303.8	42.6
33.3	-6.0	66.6	305.3	56.7

NGC 2434 major

-61.8	-11.0	45.3	189.8	47.7
-36.5	-22.0	23.6	186.3	30.7
-26.1	-10.0	15.3	177.6	16.2
-20.4	-24.0	15.5	158.3	24.6
-13.6	-27.0	11.6	185.8	14.5
-11.4	-23.0	13.2	198.6	19.7
-6.5	-22.0	12.8	179.8	18.3
-5.4	-29.0	10.8	167.4	14.0
-4.8	-36.0	9.5	189.8	11.9
-2.4	-40.0	2.7	215.9	3.0
-2.1	-45.0	8.2	212.3	8.8
-1.5	-39.0	3.5	224.4	3.5
-0.8	-31.0	2.9	242.0	2.7
-0.1	-23.0	2.9	260.5	3.7
0.5	-10.0	2.8	252.9	3.7
1.2	-3.0	2.8	226.6	4.0
2.8	20.0	2.7	209.7	3.9
6.9	5.0	2.8	196.2	3.3
9.4	7.0	10.8	189.8	14.3
11.9	-5.0	13.1	189.8	13.9
13.3	-4.0	12.5	175.9	17.8
16.3	4.0	12.1	196.4	14.2
25.0	0.0	15.4	193.0	19.8
27.9	-6.0	5.3	188.8	16.9
34.2	-6.0	21.5	195.3	20.5
56.6	0.0	40.1	187.8	37.5

NGC 2434 minor

-29.8	-36.0	24.8	172.6	20.3
-23.1	-30.0	25.2	138.2	30.7
-18.4	-22.0	19.9	130.3	21.7
-15.3	-22.0	13.4	158.3	15.8
-13.0	12.0	14.9	192.0	16.0
-11.1	-17.0	13.6	163.8	14.9
-9.4	16.0	12.6	170.3	16.6
-8.1	15.0	11.8	188.4	11.6
-6.8	11.0	9.4	152.3	11.1
-5.8	5.0	10.5	176.6	12.1
-5.1	-8.0	11.8	169.4	11.1
-4.5	-12.0	9.6	178.3	12.7
-3.8	9.0	8.1	201.5	8.5
-3.2	-8.0	10.1	185.1	9.7
-2.5	9.0	7.0	194.9	7.8
-1.8	11.0	7.1	205.2	7.2
-1.2	14.0	7.4	217.2	7.0
-0.5	6.0	6.7	236.5	5.9
0.1	17.0	6.7	250.3	5.8
0.8	20.0	6.5	230.9	6.0
1.5	17.0	7.6	218.9	7.0
2.1	0.0	6.7	194.1	7.7
2.8	-1.0	7.3	169.0	7.9

NGC 2434 minor

radius	V	e_V	Sigma	e_Sigma
3.4	6.0	7.7	189.5	9.8
4.1	0.0	9.7	191.8	11.5
4.8	20.0	11.0	169.6	12.8
5.4	5.0	12.0	187.5	13.2
6.1	-11.0	12.1	185.0	12.9
7.1	15.0	14.2	153.8	16.8
8.4	6.0	11.0	155.1	12.4
9.7	26.0	12.8	156.0	12.3
11.3	15.0	11.6	184.2	16.6
13.6	9.0	14.1	168.6	14.1
16.6	12.0	17.4	221.5	20.5
21.2	28.0	17.4	191.5	17.5
29.3	13.0	25.4	205.1	18.2

NGC 2434 PA 90°

-17.8	32.0	21.7	146.8	38.5
-13.6	-16.0	19.5	155.0	19.0
-10.7	-6.0	14.8	187.4	18.2
-8.4	-17.0	15.8	188.2	19.4
-6.8	13.0	14.7	200.6	14.6
-5.5	10.0	11.1	199.0	15.1
-4.5	-11.0	12.4	205.7	13.5
-3.8	16.0	13.1	187.9	10.5
-3.2	35.0	10.8	191.1	12.2
-2.5	27.0	10.1	192.9	12.4
-1.8	11.0	8.9	204.2	9.5
-1.2	28.0	9.6	226.4	9.0
-0.5	15.0	8.8	239.1	8.5
0.1	14.0	9.7	265.4	7.9
0.8	8.0	9.2	238.9	8.0
1.5	-3.0	9.5	222.2	10.2
2.1	-15.0	9.1	189.8	10.9
2.8	-14.0	10.7	195.3	14.1
3.4	-2.0	12.5	209.9	11.1
4.1	7.0	14.4	215.8	16.9
4.8	-31.0	15.4	192.1	15.4
5.7	15.0	13.6	206.9	15.5
7.0	-16.0	12.9	158.0	15.9
8.7	-28.0	15.6	148.5	17.1
10.9	-46.0	18.5	210.5	21.6
13.9	-30.0	22.7	163.7	26.4
18.4	-42.0	25.4	191.3	29.4

NGC 3706 major

-76.2	-161.0	30.5	167.3	27.6
-64.5	-163.0	30.2	165.3	27.6
-52.6	-114.0	20.8	188.8	11.2
-44.4	-138.0	16.2	183.0	9.3
-36.4	-144.0	6.2	204.5	8.8
-29.5	-159.0	5.1	207.2	5.9
-23.9	-142.0	3.5	226.0	3.9
-20.1	-140.0	3.3	234.5	3.5
-17.6	-139.0	2.9	238.3	3.0
-16.5	-149.0	5.1	247.1	4.8
-15.2	-141.0	4.4	238.1	4.7
-13.9	-130.0	4.2	232.7	4.3
-12.9	-136.0	3.0	248.1	3.0
-11.1	-139.0	2.8	246.0	2.8
-8.2	-143.0	3.7	248.1	3.5
-7.5	-132.0	2.9	270.8	2.7
-6.7	-134.0	2.7	272.9	2.5
-5.9	-137.0	2.9	274.8	2.8
-4.2	-122.0	2.8	292.4	2.6
-3.6	-114.0	3.1	291.1	3.0
-3.0	-108.0	3.4	298.5	3.1
-2.6	-107.0	3.0	304.2	2.8
-2.3	-107.0	3.1	307.9	3.0
-1.6	-64.0	3.2	322.6	2.9
-1.0	-30.0	3.2	329.5	2.8
-0.3	-6.0	3.1	330.2	2.8
-0.3	-7.0	3.0	332.5	2.7
0.3	5.0	3.0	331.6	2.6
1.0	26.0	3.0	333.6	2.7
1.6	73.0	3.2	322.3	2.8
2.3	109.0	3.2	309.3	2.9
3.0	117.0	3.1	293.7	2.6
3.6	126.0	3.2	287.5	2.9
4.9	127.0	3.4	284.9	3.4
5.9	139.0	3.5	284.6	3.3
6.9	139.0	3.2	271.5	2.9
7.6	131.0	3.8	266.9	3.7
9.4	127.0	3.0	265.2	3.0
11.4	128.0	2.9	261.1	3.0
13.6	133.0	3.1	253.1	3.3
14.2	133.0	3.1	253.7	3.2
15.8	144.0	4.5	241.4	5.0
18.8	148.0	4.6	241.1	5.3
21.8	135.0	3.6	238.3	3.8
26.4	128.0	4.1	236.7	4.4
30.1	143.0	5.7	218.0	16.5
38.4	97.0	17.2	217.3	17.6

NGC 3706 minor

radius	V	e_V	Sigma	e_Sigma
-29.7	-57.0	8.6	219.6	8.7
-14.2	-50.0	4.7	232.4	4.2
-9.4	-42.0	4.3	259.9	4.3
-6.8	-13.0	4.5	247.5	4.3
-5.2	-32.0	4.3	253.7	3.6
-3.9	-11.0	4.0	282.5	3.7
-2.9	-10.0	4.0	270.5	3.4
-2.2	17.0	4.2	284.6	4.1
-1.6	-5.0	3.4	303.0	3.0
-0.9	0.0	3.5	325.2	3.1
-0.3	8.0	3.4	339.6	3.0
0.4	-8.0	3.4	339.7	2.9
1.1	-17.0	3.3	314.9	3.0
1.7	1.0	3.7	306.5	3.1
2.4	-2.0	4.0	307.5	3.5
3.0	-35.0	4.2	287.3	4.1
4.0	-14.0	3.9	278.4	3.8
5.6	-28.0	4.1	290.7	4.2
7.9	-31.0	4.4	258.8	3.8
11.4	-3.0	4.4	246.8	4.2
19.2	-14.0	5.5	226.6	4.9

NGC 6407 major

-31.4	5.0	43.8	284.1	51.8
-24.0	14.0	29.4	244.9	48.7
-21.8	13.0	26.3	225.1	41.7
-19.7	19.0	29.6	213.8	46.0
-16.7	30.0	33.5	259.3	43.2
-14.3	39.0	29.6	352.9	34.0
-11.9	20.0	22.5	260.1	35.3
-10.0	22.0	20.8	290.8	31.8
-8.3	35.0	25.4	326.7	32.9
-6.9	25.0	19.8	339.6	28.4
-4.8	10.0	17.1	316.2	27.4
-3.5	24.0	19.9	315.4	29.5
-2.6	16.0	17.5	317.2	27.7
-1.8	-15.0	15.7	321.6	26.0
-0.9	2.0	15.9	339.3	25.4
0.0	26.0	17.3	341.7	26.4
0.9	34.0	14.6	323.6	25.1
1.8	29.0	15.7	324.5	25.9
2.6	52.0	17.3	321.8	27.3
3.9	14.0	15.7	311.9	26.6
5.7	-3.0	19.3	314.0	29.3
6.2	11.0	25.8	318.7	33.6
7.8	-10.0	21.8	328.0	30.4
11.3	3.0	20.1	308.0	30.1
14.0	18.0	25.2	277.5	36.1
16.8	10.0	31.7	310.3	37.7
19.7	-9.0	32.0	276.8	46.7
24.0	17.0	39.1	366.6	42.7
27.4	-12.0	35.6	327.9	44.1
30.9	-22.0	44.0	371.6	48.6
42.8	-29.0	47.8	290.6	57.3

NGC 6407 minor

-14.8	32.0	28.1	312.8	35.3
-10.2	4.0	19.4	304.3	29.8
-6.8	-4.0	19.1	286.8	30.6
-4.4	-15.0	17.0	307.9	27.7
-3.3	-14.0	21.3	332.3	29.8
-1.9	-27.0	17.0	322.0	27.1
-0.7	-9.0	19.2	340.9	27.9
0.2	27.0	16.9	344.7	26.0
1.1	11.0	17.8	351.5	26.4
2.3	10.0	18.7	339.2	27.6
4.8	-12.0	18.5	318.5	28.3
5.9	-16.0	20.6	297.0	31.2
8.0	14.0	20.0	271.0	32.3
10.7	25.0	20.4	290.0	31.4

NGC 6407 PA 108°

-10.0	13.0	28.0	296.0	36.3
-5.2	-14.0	25.3	301.8	34.2
-2.7	0.0	19.0	327.0	28.4
-1.8	12.0	24.2	334.3	31.6
-0.9	8.0	22.4	362.0	29.2
0.0	-12.0	22.2	370.0	28.8
0.9	-27.0	24.7	370.7	30.4
2.1	21.0	19.9	316.0	29.7
4.3	6.0	20.8	306.1	30.7
6.7	12.0	22.4	343.0	30.1
8.0	5.0	32.6	339.0	35.1
16.9	0.0	43.0	332.9	40.6

NGC 7192 major

radius	V	e_V	Sigma	e_Sigma
-36.5	2.0	58.4	259.8	55.4
-27.4	23.0	38.3	209.6	52.7
-25.8	9.0	30.9	237.7	43.8
-21.3	4.0	29.9	254.7	41.3
-17.0	4.0	30.1	263.7	40.5
-14.8	9.0	18.3	246.4	33.1
-13.9	-2.0	23.8	266.0	36.1
-11.8	9.0	18.9	218.2	36.2
-9.9	5.0	16.1	256.6	30.2
-8.2	28.0	16.0	262.1	29.8
-6.9	21.0	13.2	255.5	27.4
-6.0	18.0	17.7	267.6	31.0
-4.7	-5.0	13.8	265.3	27.4
-3.4	24.0	13.0	261.4	26.9
-2.6	8.0	12.4	244.3	27.3
-1.7	7.0	13.1	261.0	27.0
-0.8	0.0	11.0	247.6	25.6
0.1	0.0	11.6	247.6	26.3
1.0	-6.0	12.5	257.1	26.6
1.8	-13.0	12.8	274.6	25.9
2.7	-23.0	12.5	246.8	27.4
4.0	-18.0	12.2	250.9	26.7
5.4	-20.0	12.5	250.7	34.4
6.2	-35.0	16.0	211.7	34.0
7.5	-12.0	13.9	219.4	31.0
9.3	-15.0	17.8	237.0	33.4
11.3	-6.0	17.1	252.7	30.8
13.2	0.0	27.2	292.0	36.2
17.9	-23.0	24.4	279.9	35.2
20.2	-18.0	36.7	305.1	41.1
25.4	17.0	40.0	248.7	48.8
34.2	50.0	48.3	279.5	49.5

NGC 7192 minor

-35.0	23.0	29.9	124.7	66.7
-15.9	-12.0	16.9	198.8	36.3
-10.1	-5.0	12.1	214.5	29.3
-6.1	-2.0	12.5	216.3	29.6
-3.9	-10.0	11.7	222.1	28.3
-2.6	-7.0	11.2	220.3	27.7
-1.2	-3.0	9.4	226.6	25.0
-0.9	-6.0	10.1	231.7	25.5
0.0	-7.0	9.7	225.3	25.4
0.9	-19.0	9.6	218.3	25.8
1.2	-18.0	9.0	220.9	24.8
3.6	-8.0	10.0	223.6	26.0
6.1	-32.0	12.9	218.8	29.8
9.5	-4.0	13.6	209.0	31.6
10.2	-14.0	12.1	224.0	28.4
15.7	-18.0	23.4	248.8	37.2
33.1	44.0	27.6	138.3	59.5

NGC 7192 PA 65°

-40.5	3.0	44.9	148.6	71.7
-29.6	15.0	28.9	182.0	49.6
-14.1	13.0	12.6	175.9	33.9
-11.3	7.0	10.7	195.7	29.3
-8.8	-4.0	15.9	237.4	31.5
-5.8	14.0	11.8	204.0	29.9
-4.3	20.0	10.5	214.1	27.3
-3.6	17.0	11.2	212.4	28.4
-2.4	23.0	11.8	217.7	28.7
-1.9	19.0	16.5	224.4	33.4
-0.6	-1.0	10.2	222.6	26.4
0.3	0.0	9.6	215.2	26.1
1.5	7.0	11.9	213.3	29.1
2.9	7.0	12.4	223.8	28.9
3.9	4.0	11.1	226.9	27.2
6.3	17.0	13.6	232.2	29.6
9.7	3.0	13.3	203.9	31.7
10.7	5.0	11.1	206.8	28.6
16.2	7.0	16.1	197.4	35.6
34.7	1.0	28.5	150.3	56.5
39.6	38.0	38.7	141.3	71.9

APPENDIX C: LINE STRENGTHS

n439 major mg2

-65.2	0.224	0.005
-42.6	0.227	0.005
-30.1	0.233	0.005
-22.3	0.235	0.005
-17.1	0.263	0.005
-13.2	0.266	0.004
-10.1	0.268	0.004
-8.0	0.286	0.005
-6.2	0.273	0.004
-4.9	0.281	0.005
-4.0	0.285	0.004
-3.2	0.290	0.004
-2.3	0.299	0.004
-1.4	0.306	0.003
-0.5	0.312	0.003
0.4	0.302	0.003
1.2	0.298	0.003
2.1	0.291	0.003
3.0	0.286	0.004
3.9	0.285	0.004
4.8	0.272	0.005
6.1	0.274	0.004
7.8	0.276	0.004
9.9	0.277	0.004
12.6	0.265	0.005
15.7	0.253	0.005
20.0	0.266	0.005
26.5	0.253	0.005
36.6	0.241	0.005
55.8	0.190	0.005
86.8	0.124	0.008

n439 minor mg2

-77.7	0.232	0.011
-35.9	0.205	0.005
-15.0	0.247	0.005
-8.2	0.265	0.005
-4.8	0.287	0.004
-2.6	0.296	0.004
-1.4	0.300	0.004
-0.5	0.319	0.004
0.4	0.307	0.004
1.2	0.313	0.004
2.1	0.282	0.005
3.3	0.276	0.004
5.5	0.282	0.005
9.2	0.266	0.005
17.6	0.240	0.005
46.6	0.227	0.005

n2434 major mg2

-66.8	0.164	0.004
-40.2	0.194	0.004
-27.6	0.195	0.004
-20.9	0.184	0.003
-16.3	0.186	0.003
-13.0	0.200	0.003
-10.7	0.194	0.003
-8.7	0.202	0.003
-7.1	0.207	0.003
-5.8	0.201	0.003
-4.8	0.208	0.003
-4.1	0.223	0.003
-3.5	0.213	0.003
-2.8	0.233	0.002
-2.1	0.241	0.002
-1.5	0.254	0.002
-0.8	0.268	0.002
-0.1	0.274	0.001
0.5	0.265	0.002
1.2	0.250	0.002
1.9	0.242	0.002
2.5	0.219	0.002
3.2	0.209	0.003
3.9	0.208	0.003
4.5	0.214	0.003
5.2	0.207	0.004
6.2	0.208	0.003
7.5	0.203	0.003
9.1	0.192	0.003
11.4	0.191	0.003
14.4	0.187	0.003
18.0	0.190	0.004
23.2	0.201	0.003

n2434 minor mg2

-65.2	0.110	0.004
-32.1	0.145	0.003
-17.4	0.162	0.003
-11.0	0.176	0.003
-7.4	0.193	0.003
-5.1	0.218	0.003
-3.5	0.224	0.003
-2.5	0.228	0.003
-1.9	0.249	0.003
-1.2	0.267	0.003
-0.5	0.274	0.002
0.1	0.272	0.002
0.8	0.261	0.002
1.5	0.243	0.003
2.1	0.239	0.003
3.1	0.221	0.003
4.4	0.205	0.003
6.0	0.201	0.003
8.6	0.185	0.003
13.1	0.175	0.003
23.1	0.169	0.003
55.4	0.154	0.003

n2434 pa90 mg2

-31.1	0.102	0.004
-8.1	0.195	0.004
-3.3	0.230	0.004
-1.5	0.249	0.003
-0.2	0.268	0.003
1.1	0.251	0.003
2.9	0.229	0.003
7.4	0.198	0.003
33.0	0.094	0.004

APPENDIX C – *continued*

n3706 major mg2

-76.0	0.218	0.004
-53.7	0.204	0.004
-40.0	0.200	0.003
-31.7	0.198	0.004
-23.9	0.211	0.004
-19.5	0.225	0.003
-16.5	0.230	0.003
-14.3	0.223	0.003
-10.5	0.233	0.003
-8.0	0.245	0.003
-7.0	0.243	0.003
-6.3	0.250	0.003
-5.6	0.253	0.003
-5.0	0.266	0.003
-4.3	0.259	0.002
-3.7	0.272	0.002
-3.0	0.281	0.002
-2.3	0.290	0.002
-1.7	0.297	0.001
-1.0	0.312	0.001
-0.3	0.315	0.001
0.3	0.317	0.001
1.0	0.312	0.001
1.7	0.302	0.001
2.3	0.289	0.002
3.0	0.286	0.002
3.7	0.275	0.002
4.3	0.275	0.002
5.0	0.256	0.003
5.6	0.261	0.003
6.3	0.260	0.003
7.0	0.254	0.003
8.0	0.246	0.003
9.3	0.245	0.003
10.6	0.246	0.003
11.9	0.239	0.003
13.6	0.246	0.003
15.6	0.232	0.003
17.9	0.228	0.003
20.9	0.228	0.003
24.5	0.215	0.004
29.4	0.213	0.003
37.0	0.196	0.003
52.7	0.228	0.004
81.9	0.175	0.004

n3706 minor mg2

-76.5	0.222	0.008
-31.1	0.209	0.004
-13.6	0.233	0.003
-7.7	0.236	0.003
-4.8	0.266	0.003
-3.2	0.284	0.003
-2.3	0.263	0.003
-1.6	0.305	0.003
-0.9	0.317	0.002
-0.3	0.327	0.002
0.4	0.321	0.002
1.1	0.310	0.002
1.7	0.303	0.003
2.7	0.287	0.003
4.2	0.268	0.003
6.8	0.241	0.003
11.6	0.237	0.004
23.4	0.221	0.004
60.0	0.232	0.005

n7192 major mg2

-36.6	0.168	0.005
-27.4	0.180	0.005
-21.3	0.198	0.005
-17.0	0.204	0.005
-13.9	0.223	0.005
-11.8	0.210	0.005
-10.0	0.241	0.004
-8.2	0.239	0.004
-7.0	0.246	0.005
-6.1	0.253	0.004
-5.2	0.246	0.004
-4.3	0.260	0.004
-3.4	0.262	0.003
-2.6	0.266	0.003
-1.7	0.282	0.002
-0.8	0.283	0.002
0.1	0.289	0.002
1.0	0.287	0.002
1.8	0.269	0.002
2.7	0.263	0.003
3.6	0.254	0.003
4.5	0.244	0.004
5.4	0.237	0.004
6.2	0.236	0.005
7.6	0.239	0.004
9.3	0.234	0.004
11.1	0.228	0.005
13.2	0.214	0.004
16.3	0.191	0.005
20.2	0.221	0.005
25.4	0.153	0.005

n7192 minor mg2

-42.7	0.233	0.006
-18.1	0.230	0.005
-9.8	0.236	0.005
-6.1	0.235	0.005
-3.9	0.248	0.004
-2.6	0.254	0.005
-1.8	0.262	0.004
-0.9	0.280	0.003
0.0	0.277	0.003
0.9	0.278	0.003
1.8	0.259	0.004
2.6	0.263	0.005
3.9	0.240	0.004
6.1	0.225	0.005
9.8	0.230	0.005
17.8	0.205	0.005
41.5	0.204	0.006

n7192 pa65 mg2

-42.9	0.175	0.005
-16.0	0.219	0.005
-9.2	0.231	0.005
-5.8	0.238	0.005
-3.6	0.258	0.004
-2.4	0.268	0.004
-1.5	0.249	0.004
-0.6	0.285	0.003
0.3	0.277	0.003
1.1	0.280	0.004
2.0	0.253	0.004
3.3	0.248	0.004
5.5	0.250	0.004
8.8	0.218	0.005
15.3	0.198	0.005
35.6	0.174	0.005

APPENDIX C – *continued*

n6407 major mg2

-17.1	0.253	0.005
-14.0	0.298	0.005
-11.9	0.283	0.005
-10.1	0.273	0.004
-8.3	0.266	0.004
-7.0	0.277	0.005
-6.2	0.282	0.004
-5.3	0.283	0.004
-4.4	0.280	0.004
-3.5	0.289	0.003
-2.6	0.298	0.003
-1.8	0.303	0.002
-0.9	0.312	0.002
0.0	0.315	0.002
0.9	0.306	0.002
1.8	0.300	0.002
2.6	0.292	0.003
3.5	0.296	0.003
4.4	0.287	0.004
5.3	0.267	0.004
6.2	0.268	0.005
7.0	0.280	0.005
8.4	0.272	0.004
10.1	0.285	0.004
11.9	0.276	0.005
14.0	0.253	0.004
17.1	0.257	0.005

n6407 minor mg2

-12.6	0.293	0.005
-8.0	0.271	0.004
-5.5	0.309	0.005
-3.7	0.294	0.004
-2.5	0.301	0.004
-1.6	0.315	0.004
-0.7	0.326	0.003
0.2	0.324	0.003
1.1	0.316	0.003
1.9	0.301	0.004
2.8	0.288	0.005
4.0	0.290	0.004
6.2	0.277	0.004
9.2	0.282	0.005
14.0	0.261	0.005
22.9	0.266	0.005

n6407 pa108 mg2

-46.8	0.240	0.006
-8.3	0.265	0.005
-4.2	0.284	0.005
-2.1	0.310	0.004
-0.9	0.320	0.004
0.0	0.320	0.004
0.9	0.303	0.005
2.1	0.299	0.004
4.2	0.276	0.005
8.3	0.284	0.005
20.2	0.251	0.005

n439 major fe52

-65.2	2.00	0.20
-42.6	2.05	0.18
-30.1	2.66	0.18
-22.3	2.41	0.18
-17.1	2.34	0.17
-13.2	2.47	0.16
-10.1	2.77	0.16
-8.0	2.57	0.17
-6.2	2.78	0.14
-4.9	2.16	0.18
-4.0	2.49	0.16
-3.2	2.81	0.14
-2.3	2.60	0.13
-1.4	2.96	0.11
-0.5	2.82	0.10
0.4	2.56	0.10
1.2	2.69	0.11
2.1	3.02	0.12
3.0	3.04	0.14
3.9	2.27	0.16
4.8	2.22	0.17
6.1	2.87	0.14
7.8	2.58	0.16
9.9	2.75	0.15
12.6	2.50	0.18
15.7	2.67	0.18
20.0	2.84	0.18
26.5	2.44	0.18

n439 minor fe52

-8.2	2.29	0.17
-4.8	2.87	0.16
-2.6	2.81	0.14
-1.4	2.86	0.15
-0.5	3.23	0.14
0.4	2.94	0.14
1.2	2.88	0.15
2.1	3.09	0.18
3.3	2.82	0.16
5.5	2.70	0.18
9.2	2.77	0.18
17.6	2.27	0.18
46.6	2.47	0.19

APPENDIX C – *continued*

n2434 major fe52

-40.2	2.69	0.26
-27.6	2.26	0.26
-20.9	2.10	0.26
-16.3	2.38	0.24
-13.0	2.18	0.26
-10.7	2.13	0.26
-8.7	2.31	0.22
-7.1	2.65	0.23
-5.8	2.83	0.20
-4.8	2.46	0.25
-4.1	2.71	0.23
-3.5	2.91	0.21
-2.8	2.72	0.18
-2.1	2.80	0.16
-1.5	2.60	0.14
-0.8	2.86	0.12
-0.1	2.93	0.10
0.5	2.85	0.11
1.2	2.84	0.13
1.9	2.67	0.15
2.5	2.68	0.17
3.2	2.77	0.20
3.9	2.68	0.22
4.5	2.97	0.24
5.2	2.65	0.26
6.2	2.50	0.21
7.5	2.57	0.24
9.1	2.53	0.23
11.4	2.34	0.23
14.4	2.84	0.24
18.0	1.92	0.26
23.2	2.64	0.25
32.0	2.86	0.26

n2434 minor fe52

-32.1	2.24	0.26
-17.4	2.45	0.25
-11.0	1.47	0.25
-7.4	2.37	0.25
-5.1	2.43	0.23
-3.5	2.70	0.22
-2.5	2.85	0.26
-1.9	2.93	0.22
-1.2	2.74	0.19
-0.5	3.01	0.16
0.1	2.88	0.15
0.8	2.88	0.16
1.5	2.26	0.20
2.1	2.13	0.24
3.1	2.51	0.21
4.4	2.30	0.26
6.0	2.52	0.26
8.6	2.57	0.25
13.1	2.39	0.26
23.1	2.23	0.26
55.4	1.55	0.26

n2434 pa90 fe52

-31.1	3.22	0.29
-8.1	2.86	0.26
-3.3	2.78	0.26
-1.5	2.72	0.25
-0.2	2.94	0.19
1.1	2.91	0.22
2.9	2.94	0.24
7.4	2.38	0.26
33.0	2.98	0.29

n3706 major fe52

-76.0	2.13	0.30
-53.7	2.19	0.26
-40.0	2.96	0.25
-31.7	2.63	0.26
-23.9	2.67	0.26
-19.5	2.79	0.24
-16.5	2.56	0.23
-14.3	2.55	0.23
-10.5	3.18	0.23
-8.0	2.84	0.19
-7.0	3.00	0.25
-6.3	2.93	0.23
-5.6	3.18	0.22
-5.0	2.92	0.20
-4.3	3.06	0.18
-3.7	3.12	0.16
-3.0	3.19	0.14
-2.3	3.09	0.12
-1.7	3.14	0.10
-1.0	3.30	0.08
-0.3	3.32	0.07
0.3	3.40	0.07
1.0	3.27	0.09
1.7	3.14	0.11
2.3	3.11	0.13
3.0	2.99	0.15
3.7	3.17	0.16
4.3	3.20	0.18
5.0	3.15	0.20
5.6	2.95	0.22
6.3	3.11	0.23
7.0	2.65	0.25
8.0	2.49	0.19
9.3	2.68	0.21
10.6	3.07	0.23
11.9	2.75	0.25
13.6	2.88	0.23
15.6	2.55	0.25
17.9	2.55	0.24
20.9	2.79	0.25
24.5	2.61	0.26
29.4	2.16	0.25
37.0	2.31	0.26
52.7	2.76	0.26
81.9	1.55	0.26

n3706 minor fe52

-31.1	3.21	0.26
-13.6	2.20	0.26
-7.7	2.76	0.25
-4.8	2.60	0.26
-3.2	3.23	0.23
-2.3	3.11	0.25
-1.6	3.17	0.20
-0.9	3.55	0.15
-0.3	3.39	0.12
0.4	3.57	0.12
1.1	2.98	0.16
1.7	3.14	0.21
2.7	2.61	0.20
4.2	2.80	0.24
6.8	2.60	0.25
11.6	2.66	0.26
23.4	2.86	0.26

APPENDIX C – *continued*

n6407 major fe52

-17.1	2.22	0.16
-14.0	2.39	0.16
-11.9	2.89	0.18
-10.1	3.47	0.16
-8.3	2.42	0.14
-7.0	2.34	0.17
-6.2	3.03	0.16
-5.3	3.11	0.15
-4.4	2.92	0.13
-3.5	2.88	0.12
-2.6	3.05	0.10
-1.8	3.11	0.08
-0.9	2.67	0.07
0.0	2.72	0.07
0.9	3.07	0.07
1.8	3.07	0.09
2.6	3.07	0.10
3.5	3.27	0.12
4.4	2.62	0.13
5.3	2.88	0.15
6.2	2.34	0.16
7.0	1.95	0.17
8.4	2.63	0.14
10.1	2.06	0.16
11.9	3.05	0.17
14.0	2.11	0.16
17.1	2.37	0.16
20.9	1.97	0.17

n6407 minor fe52

-22.2	2.44	0.18
-12.6	2.54	0.17
-8.0	2.50	0.16
-5.5	2.84	0.18
-3.7	2.73	0.14
-2.5	2.53	0.16
-1.6	2.73	0.13
-0.7	2.86	0.11
0.2	3.17	0.11
1.1	2.91	0.12
1.9	3.13	0.14
2.8	2.62	0.17
4.0	2.39	0.15
6.2	2.95	0.16
9.2	2.25	0.18
14.0	2.23	0.18
22.9	2.25	0.18

n6407 pa108 fe52

-8.3	2.61	0.17
-4.2	2.27	0.17
-2.1	2.65	0.14
-0.9	2.88	0.16
0.0	2.83	0.15
0.9	2.43	0.16
2.1	2.56	0.15
4.2	2.63	0.17
8.3	2.64	0.18
20.2	2.27	0.18

n7192 major fe52

-36.6	2.23	0.18
-27.4	2.13	0.18
-21.3	2.39	0.17
-17.0	2.05	0.17
-13.9	2.56	0.17
-11.8	2.02	0.18
-10.0	2.32	0.16
-8.2	2.27	0.14
-7.0	2.33	0.18
-6.1	2.61	0.16
-5.2	2.81	0.15
-4.3	2.87	0.13
-3.4	2.86	0.11
-2.6	2.67	0.10
-1.7	2.84	0.08
-0.8	2.77	0.07
0.1	3.11	0.07
1.0	2.83	0.07
1.8	2.66	0.08
2.7	2.83	0.10
3.6	2.64	0.12
4.5	2.68	0.13
5.4	2.59	0.15
6.2	2.38	0.17
7.6	2.48	0.13
9.3	2.26	0.15
11.1	2.21	0.17
13.2	2.51	0.16
16.3	2.29	0.17
20.2	2.03	0.18
25.4	2.30	0.18
33.3	2.22	0.18
53.3	2.34	0.18

n7192 minor fe52

-18.1	2.55	0.18
-9.8	2.61	0.17
-6.1	2.36	0.18
-3.9	2.94	0.16
-2.6	2.93	0.18
-1.8	2.96	0.15
-0.9	3.07	0.12
0.0	3.22	0.11
0.9	3.05	0.12
1.8	3.42	0.15
2.6	3.44	0.18
3.9	3.09	0.16
6.1	3.04	0.18
9.8	1.96	0.17
17.8	2.15	0.18

n7192 pa65 fe52

-16.0	2.26	0.18
-9.2	2.71	0.18
-5.8	2.46	0.17
-3.6	2.45	0.15
-2.4	3.03	0.16
-1.5	3.42	0.14
-0.6	2.78	0.12
0.3	2.92	0.11
1.1	3.13	0.13
2.0	2.80	0.15
3.3	2.77	0.14
5.5	3.09	0.16
8.8	2.80	0.17
15.3	2.40	0.18

n439 major fe53

-30.1	2.19	0.17
-22.3	2.08	0.17
-17.1	2.54	0.17
-13.2	2.36	0.16
-10.1	2.47	0.15
-8.0	2.29	0.16
-6.2	2.59	0.14
-4.9	2.83	0.17
-4.0	2.58	0.16
-3.2	2.85	0.14
-2.3	2.39	0.12
-1.4	2.88	0.11
-0.5	2.87	0.10
0.4	3.09	0.10
1.2	2.94	0.10
2.1	2.49	0.12
3.0	2.33	0.14
3.9	2.50	0.15
4.8	2.26	0.17
6.1	2.65	0.14
7.8	2.59	0.16
9.9	2.72	0.15
12.6	2.47	0.17
15.7	2.37	0.17
20.0	2.28	0.17
26.5	2.38	0.17

n439 minor fe53

-15.0	1.90	0.17
-8.2	2.10	0.17
-4.8	2.74	0.16
-2.6	2.47	0.13
-1.4	3.02	0.15
-0.5	2.57	0.13
0.4	2.64	0.13
1.2	2.65	0.14
2.1	2.60	0.17
3.3	2.44	0.16
5.5	2.10	0.17
9.2	2.35	0.17

APPENDIX C – *continued*

n2434 major f53

-40.2	2.41	0.25
-27.6	2.52	0.25
-20.9	2.37	0.25
-16.3	1.93	0.24
-13.0	2.50	0.25
-10.7	2.20	0.25
-8.7	2.47	0.21
-7.1	2.24	0.22
-5.8	2.24	0.19
-4.8	2.41	0.24
-4.1	2.61	0.22
-3.5	2.62	0.20
-2.8	2.59	0.18
-2.1	2.82	0.16
-1.5	2.46	0.13
-0.8	2.62	0.11
-0.1	2.72	0.10
0.5	2.49	0.11
1.2	2.46	0.12
1.9	2.42	0.15
2.5	2.64	0.17
3.2	2.46	0.19
3.9	2.62	0.21
4.5	2.29	0.23
5.2	2.61	0.25
6.2	2.58	0.20
7.5	2.06	0.23
9.1	2.40	0.22
11.4	2.21	0.23
14.4	2.78	0.24
18.0	2.58	0.25
23.2	2.18	0.25
32.0	2.73	0.25

n2434 minor fe53

-32.1	1.62	0.26
-17.4	1.95	0.25
-11.0	1.88	0.25
-7.4	2.10	0.25
-5.1	1.39	0.22
-3.5	1.96	0.21
-2.5	2.49	0.25
-1.9	2.47	0.22
-1.2	2.37	0.18
-0.5	2.59	0.15
0.1	2.65	0.14
0.8	2.65	0.16
1.5	2.55	0.19
2.1	2.65	0.23
3.1	2.15	0.20
4.4	2.25	0.25
6.0	2.46	0.25
8.6	1.75	0.25
13.1	2.07	0.25
23.1	1.12	0.26

n2434 pa90 fe53

-8.1	1.81	0.25
-3.3	2.90	0.25
-1.5	2.81	0.24
-0.2	2.80	0.19
1.1	2.40	0.21
2.9	2.42	0.23
7.4	2.10	0.25

n3706 major fe53

-53.7	2.42	0.25
-40.0	2.03	0.25
-31.7	2.16	0.25
-23.9	2.23	0.25
-19.5	2.29	0.23
-16.5	2.11	0.22
-14.3	2.36	0.23
-10.5	2.36	0.22
-8.0	2.65	0.18
-7.0	2.08	0.24
-6.3	2.38	0.22
-5.6	2.67	0.21
-5.0	2.40	0.19
-4.3	2.49	0.18
-3.7	2.45	0.16
-3.0	2.63	0.14
-2.3	3.04	0.12
-1.7	2.82	0.10
-1.0	3.08	0.08
-0.3	2.91	0.07
0.3	3.02	0.07
1.0	2.89	0.08
1.7	2.87	0.10
2.3	2.60	0.12
3.0	2.58	0.14
3.7	2.72	0.16
4.3	2.75	0.18
5.0	2.89	0.19
5.6	3.07	0.21
6.3	2.42	0.23
7.0	2.32	0.24
8.0	2.39	0.19
9.3	2.50	0.21
10.6	2.41	0.22
11.9	2.65	0.24
13.6	2.44	0.22
15.6	2.49	0.24
17.9	2.60	0.24
20.9	1.98	0.24
24.5	2.57	0.25
29.4	2.32	0.24
37.0	2.09	0.25
52.7	1.95	0.25

n3706 minor fe53

-31.1	2.91	0.25
-13.6	2.31	0.25
-7.7	2.13	0.24
-4.8	2.55	0.25
-3.2	2.76	0.22
-2.3	2.66	0.24
-1.6	2.44	0.19
-0.9	3.01	0.15
-0.3	3.04	0.11
0.4	2.94	0.12
1.1	2.79	0.16
1.7	2.72	0.21
2.7	2.56	0.20
4.2	2.50	0.23
6.8	2.23	0.25
11.6	2.57	0.25
23.4	2.25	0.25

APPENDIX C – *continued*

n6407 major fe53

-21.0	2.21	0.16
-14.0	2.14	0.16
-10.1	2.18	0.15
-5.3	2.30	0.14
-4.4	2.07	0.13
-3.5	3.01	0.11
-2.6	2.65	0.10
-1.8	2.67	0.08
-0.9	2.45	0.07
0.0	2.03	0.07
0.9	2.54	0.07
1.8	2.41	0.08
2.6	2.60	0.10
5.3	2.21	0.14
8.4	2.06	0.13
17.1	1.95	0.16
20.9	2.34	0.16
26.5	2.28	0.16

n6407 minor fe53

-12.6	2.59	0.17
-8.0	2.01	0.16
-3.7	1.78	0.14
-2.5	1.96	0.15
-1.6	1.85	0.13
-0.7	2.34	0.11
0.2	2.22	0.10
1.1	2.27	0.11
1.9	2.50	0.14
2.8	1.85	0.17
4.0	1.89	0.15
6.2	2.45	0.16
9.2	2.33	0.17

n6407 pa108 fe53

-4.2	1.72	0.17
-2.1	1.82	0.14
-0.9	2.18	0.16
0.0	2.50	0.15
0.9	2.24	0.16
2.1	1.97	0.14
4.2	1.77	0.17
8.3	2.15	0.17
20.2	1.61	0.17
36.3	1.37	0.45

n7192 major fe53

-13.9	1.93	0.17
-11.8	1.80	0.18
-10.0	2.02	0.15
-8.2	2.22	0.14
-7.0	2.19	0.17
-6.1	2.35	0.16
-5.2	2.33	0.14
-4.3	2.39	0.13
-3.4	2.38	0.11
-2.6	2.54	0.09
-1.7	2.72	0.08
-0.8	2.72	0.07
0.1	2.66	0.07
1.0	2.62	0.07
1.8	2.77	0.08
2.7	2.64	0.10
3.6	2.65	0.11
4.5	2.50	0.13
5.4	2.37	0.15
6.2	2.33	0.16
7.6	2.27	0.13
9.3	2.17	0.15
11.1	2.13	0.17
13.2	2.31	0.16
16.3	2.04	0.16
20.2	2.05	0.17
25.4	1.96	0.18
33.3	1.94	0.17
53.3	1.86	0.17

n7192 minor fe53

-42.7	1.59	0.20
-18.1	1.63	0.18
-9.8	2.04	0.17
-6.1	1.78	0.17
-3.9	2.70	0.16
-2.6	2.52	0.17
-1.8	2.82	0.14
-0.9	2.85	0.12
0.0	2.47	0.11
0.9	2.58	0.12
1.8	2.56	0.14
2.6	2.49	0.17
3.9	2.55	0.15
6.1	2.47	0.17
9.8	2.52	0.16
17.8	2.21	0.17

n7192 pa65 fe53

-42.9	1.45	0.18
-16.0	1.30	0.17
-9.2	1.81	0.17
-5.8	1.93	0.16
-3.6	2.16	0.15
-2.4	2.77	0.16
-1.5	2.80	0.13
-0.6	2.57	0.11
0.3	2.59	0.11
2.0	1.90	0.15
3.3	2.31	0.14
5.5	2.02	0.16
8.8	1.54	0.17
15.3	1.96	0.17
35.6	1.49	0.18